

2

AD-A238 592



Edward L. Ginzton Laboratory  
W. W. Hansen Laboratories of Physics  
Stanford University  
Stanford, California 94305

DTIC  
SELECTE  
JUL 18 1991  
S D

Final Report  
to  
Office of Naval Research  
of  
A Program of Research  
on

Physical Concepts and Modeling  
Procedures for Picosecond and  
Subpicosecond Distributed Circuits

G.L. No. 4840

Contract # N00014-85-K-0381

Principal Investigators

D. M. Bloom  
B. A. Auld

June 1991

CLASSIFICATION AUTHORITY  
EXEMPT FROM AUTOMATIC  
DOWNGRADING AND  
DECLASSIFICATION

91 7 13 068

91-05073



## Table of Contents

I. Introduction	3
II. Progress Under Contract	4
III. Conclusion	6
IV. Technology Transfer	6
V. Relevant Stanford Group Publications	7
VI. Dissertations Supported by this Contract	7
VII. References	8
VIII. Appendix: "Gallium Arsenide Integrated Circuits for Measurement and Generation of Electrical Waveforms to 300 GHz"	

## I. Introduction

The development of advanced high-speed digital devices and integrated circuits has been spurred by a number of applications, including fiber-optic digital data transmission at gigahertz rates, high-throughput computing, and wideband signal processing. Military interest in high-speed digital electronics stems from the need to rapidly acquire, digitize, and process very large amounts of data in EW systems. Associated with the needs for high-speed logic are commensurate demands for broadband analog signal processing, interface, and I/O electronics. Such circuits include correlators, broadband adaptive filters, picosecond-resolution sample-and-hold gates, and multigigahertz-rate D/A and A/D converters. For the digital and analog circuits mentioned, ultra-wide bandwidth instrumentation of superior speed is required for measuring the devices to be employed.

It is primarily this critical need for ultra-wide bandwidth instrumentation that has been addressed through the work done under this contract. Without such a capability for performing picosecond and subpicosecond measurements of electrical phenomena, it will be impossible to correctly engineer and characterize devices and circuits required for the applications listed above.

While we give only the highlights of the results achieved during work on this contract, details of the theory and design used in constructing the instrumentation, as well as the fabrication techniques employed, are fully discussed in an Appendix, consisting of the entire dissertation of R. A. Marsland on the integrated circuit sampler technology developed under this contract.

Accession For	
NTIS	CRUI <input checked="" type="checkbox"/>
DTIC	TAB <input type="checkbox"/>
Unannounced	<input type="checkbox"/>
Justification	
By <i>per AD-A 172828</i>	
Distribution	
Availability Codes	
Dist	Avail and/or Spec
<i>A-1</i>	

## II. Progress Under Contract

### Picosecond Pulse Generators and Sampling Circuits

We have developed monolithic circuits for both picosecond pulse generation and sampling of repetitive waveforms, with bandwidths extending to 290 GHz. The circuits used to strobe these samplers are nonlinear transmission lines (NLTLs),<sup>1</sup> high-impedance coplanar waveguide transmission lines periodically loaded with reverse-biased Schottky diodes, which steepen the falling portion of a sinusoidal excitation on the line to a brief (1.6 ps) 10%-90% falling edge. The samplers developed under this contract<sup>2</sup> are two-diode sampling bridges which are strobed by the derivative of the NLTL's falling edge, which is approximately an impulse function. We have also used these samplers in a monolithic Wheatstone bridge<sup>3</sup> for measuring vector parameters of waves (e.g. S-parameters) in high-speed devices. Incorporating this bridge into a coplanar waveguide probe, we were able to calibrate and make measurements to 78 GHz, limited only by availability of frequency extenders for the network analyzer we were using.

Previously, we had reported a diode sampling bridge monolithically integrated with a NLTL strobe-pulse and test-signal generators which had a sampling bandwidth of over 130 GHz. This sampler measured a 4 ps fall time from the attenuated output of the on-chip NLTL test-signal generator. The speed-limiting factors in this circuit were sampling diode series resistance and NLTL transition times themselves. The series resistance was high due to the relatively thick N<sup>-</sup> layer used for the varactor diodes of the on-chip NLTL. This problem was remedied in later generations by going to a two-chip solution in which the first part of the edge-sharpening from a microwave sinusoid to a sawtooth wave was accomplished on one chip with a hyperabrupt-doped NLTL, giving a 5 ps falling edge. The final edge steepening was performed on the second chip with an abrupt-doped sampling IC, where varactor breakdown was not as critical because of lower signal amplitudes. This allowed a thinner N<sup>-</sup> layer to be employed in the sampler, reducing the series resistance of the sampling diodes.

To increase the speed of the sampler, improvements were made to the NLTL, the sampling diode epitaxial structure, and overall IC layout. The portion of the NLTL which was integrated on the sampling chip was designed to have a periodic cutoff frequency of

500 GHz, as discussed in the Appendix, Ch. 3. With the other improvements, the completed sampler exhibited better than twice the first-generation sampler's bandwidth.

### Modeling

Our ability to model complex, high-frequency structures, such as those designed and built under this contract, has been enhanced by the acquisition of important CAD tools, running on a RISC-based UNIX workstation. We have entered into agreements with Meta-Software (makers of HSPICE, a sophisticated and powerful version of SPICE), with CONTEC Microelectronics (also makers of a version of SPICE with good transmission-line models), and with Sonnet Software (makers of em, an electromagnetic structure simulator for arbitrary geometries.)

Both versions of SPICE we have currently offer significantly improved transmission-line models over the standard delay-based model used in Microwave SPICE from eesof. These models incorporate both loss and dispersion, as well as arbitrary coupling between lines. Hence, they allow us to more accurately model NLTLs and samplers, a necessity for second- and third-order improvements in performance. In addition, HSPICE offers numerical optimization of parameters.

Em calculates the S-parameters for arbitrary microstrip or coplanar waveguide geometry with high accuracy for all microwave frequencies. It solves for the current distribution in the metallization, including all dispersion, stray coupling, discontinuities, surface waves, moding, metallization loss, dielectric loss, and radiation loss. It, too, will enable us to further improve our designs.

### **III. Conclusion**

We have demonstrated ultra-wide bandwidth time- and frequency-domain instrumentation which can be monolithically integrated and used to 300 GHz for measuring ultrafast electrical phenomena. Work will continue along the directions we have mapped out in order to bring increased bandwidth and accuracy to the instruments we have developed and disclosed.

### **IV. Technology Transfer**

The NLTL and sampler technologies are already finding applications in industry, and exist in 4-6 products: Licensing agreements have been signed with Tektronix and Yokogawa Electric Corp. concerning both technologies. Although negotiations are only beginning with Hewlett-Packard, they have already put the NLTL to use as a strobe generator in their HP-54124T 50 GHz sampling oscilloscope.<sup>4</sup>

## VI. Relevant Stanford Group Publications

M. J. W. Rodwell, D. M. Bloom, and B. A. Auld, "Nonlinear transmission line for picosecond pulse compression and broadband phase modulation," *Electron. Lett.*, **23**, 3, p. 109 (1987).

M. J. W. Rodwell, C. J. Madden, B.T. Khuri-Yakub, D. M. Bloom, Y. C. Pao, N. S. Gabriel, and S. P. Swierkowski, "Generation of 7.8 ps electrical transients on a monolithic nonlinear transmission line," *Electron. Lett.*, **24**, 2, p. 100 (1988).

C. J. Madden, M. J. W. Rodwell, R. A. Marsland, D. M. Bloom, and Y. C. Pao, "Generation of 3.5-ps fall-time shock waves on a monolithic GaAs nonlinear transmission line," *IEEE Electron Device Lett.*, **EDL-9**, 6, p. 303 (1988).

C. J. Madden, R. A. Marsland, M. J. W. Rodwell, D. M. Bloom, and Y. C. Pao, "Hyperdoped GaAs nonlinear transmission line for picosecond shockwave generation," *Appl. Phys. Lett.*, **54**, 11, pp. 1019-1021 (1989).

R. A. Marsland, C. J. Madden, V. Valdivia, M. J. W. Rodwell, and D. M. Bloom, "Picosecond pulse generation and sampling with GaAs monolithic integrated circuits," in *OSA Proceedings on Picosecond Electronics and Optoelectronics*, edited by T. C. L. G. Sollner and D. M. Bloom (Optical Society of America, Washington, D. C.), p. 16 (1989).

R. A. Marsland, V. Valdivia, C. J. Madden, M. J. W. Rodwell, D. M. Bloom, "130 GHz GaAs monolithic integrated circuit sampling head," *Appl. Phys. Lett.*, **55**, pp. 592-594 (1989).

R. A. Marsland, C. J. Madden, D. W. Van Der Weide, M. S. Shakouri, D. M. Bloom, "Monolithic integrated circuits for mm-wave instrumentation," *IEEE GaAs IC Symposium Technical Digest*, New Orleans, LA, pp. 19-22 (1990).

## VII. Dissertations Supported by this Contract

M. J. W. Rodwell, "Picosecond Electrical Wavefront Generation and Picosecond Optoelectronic Instrumentation," (1987).

R. A. Marsland, Jr., "Gallium Arsenide Integrated Circuits for Measurement and Generation of Electrical Waveforms to 300 GHz," (1990).

C. J. Madden, "Picosecond and Subpicosecond Electrical Shock-Wave Generation on a Gallium Arsenide Nonlinear Transmission Line," (1990).

---

## VII. References

- 1 C. J. Madden, R. A. Marsland, M. J. W. Rodwell, D. M. Bloom, and Y. C. Pao, "Hyperabrupt-doped GaAs nonlinear transmission line for picosecond shockwave generation," *Appl. Phys. Lett.*, **54**, 11, pp. 1019-1021 (1989).
- 2 R. A. Marsland, V. Valdivia, C. J. Madden, M. J. W. Rodwell, D. M. Bloom, "130 GHz GaAs monolithic integrated circuit sampling head," *Appl. Phys. Lett.*, **55**, pp. 592-594 (1989).
- 3 R. A. Marsland, C. J. Madden, D. W. Van Der Weide, M. S. Shakouri, D. M. Bloom, "Monolithic integrated circuits for mm-wave instrumentation," IEEE GaAs IC Symposium Technical Digest, New Orleans, LA, pp. 19-22 (1990).
- 4 W. C. Whiteley, W. E. Kunz, W. J. Ankam, "50 GHz sampler hybrid utilizing a small shockline and an internal SRD," IEEE MTT-S Symposium Technical Digest, Boston, MA, pp. 895-898 (1990).

**GALLIUM ARSENIDE  
INTEGRATED CIRCUITS  
FOR  
MEASUREMENT AND GENERATION  
OF  
ELECTRICAL WAVEFORMS TO 300 GHZ**

**A DISSERTATION  
SUBMITTED TO THE DEPARTMENT OF ELECTRICAL ENGINEERING  
AND THE COMMITTEE ON GRADUATE STUDIES  
OF STANFORD UNIVERSITY  
IN PARTIAL FULFILLMENT OF THE REQUIREMENTS  
FOR THE DEGREE OF  
DOCTOR OF PHILPSOPHY**

**By  
Robert A. Marsland, Jr.  
June 1990**

© Copyright by Robert A. Marsland, Jr., 1990  
All Rights Reserved

# Abstract

Until the advent of the monolithic nonlinear transmission line (NLTL), high-speed samplers found in oscilloscopes, network analyzers, frequency counters, frequency synthesizers, and spectrum analyzers were based on the step recovery diode (SRD) and a sampling bridge requiring hybrid assembly. SRD technology is quite mature and switching speeds much faster than  $\sim 20$ ps cannot be expected. Because sensitivity can be traded for speed to some degree, instruments based on this technology have reached 60 GHz. The NLTL and monolithic sampling bridge exploiting  $> 1$ THz cutoff frequency diodes with no package or interconnect parasitics offer a dramatic improvement in bandwidth over the SRD hybrid technology, or similarly, increased sensitivity with similar bandwidth.

As has been shown previously, the shock wave output of a NLTL can have a fall-time of less than 1.6 ps. This thesis presents the first applications of this technology in conjunction with monolithic diode sampling bridges for mm-wave instrumentation to 300 GHz. A two-diode sampling bridge has been monolithically integrated with a NLTL as the strobe pulse generator to achieve a sampling bandwidth of over 290 GHz. In addition, two sampling bridges have been integrated with a resistive directional bridge to form a 60 GHz S-parameter test-set on a chip. The use of a NLTL for phase-matched frequency doubling is also discussed.

These integrated circuits not only provide a dramatic improvement in performance, but also the possibility of mass-production and lower cost of assembly due to reduced part count. In addition, because of their small size, it is possible to mount the integrated circuits on probe tips to provide on-wafer measurement capability to 300 GHz without the reduced sensitivity and directivity caused by coaxial cables.

# Acknowledgements

This work is the result of a collaboration between many people, I would like to thank:

- My wife, Diane Marsland for providing financial and moral support.
- Dave Bloom for his many ideas and broad scientific understanding that helped focus my own creativity.
- Bert Auld, whose comments improved this thesis immeasurably, and Pierre Khuri-Yakub for his timely comments as well.
- Chris Madden and Mark Rodwell for initiating the GaAs process in Ginzton lab and pioneering the nonlinear transmission line effort.
- Brian Kolner, Kurt Weingarten, Mark Rodwell, Reza Majidy-Ahy, and Jim Freeman for developing the electrooptic sampling system into a test instrument that even I could use effectively.
- Mohammad Shakouri for obtaining the experimental data on the distributed doubler presented in Chapter 5 and for continuing this effort.
- Dan Van Der Weide for assistance in the directional bridge testing and continuing work on directional bridge probe discussed in Chapter 6.
- B. Roe Hemenway and Raj Apte for maintenance of the computer so vital to IC layout.
- The entire Bloom group past and present for their insights and discussions.

- Eric Lim, Alistair Black, and Mark Rodwell for inspiring the work on the diatomic lattice for phase-matched frequency multiplication (Chapter 5).
- Yi-Ching Pao, Majid Riaziat, and Gerald Li of Varian for their assistance in processing. Yi-Ching Pao provided all of the MBE material used in the course of this thesis research.
- Lance Goddard and Tom Carver for making the Ginzton microstructures facility a clean and safe place to work.
- John Owens and Chris Storment for help in developing the airbridge process.
- Martin Grace, William Oldfield, Jay Banwait, and Don Bradley of Wiltron Company for their assistance in packaging and advice on network measurements.
- Hugo Vifian of Hewlett-Packard for donating the 8510B used extensively for this thesis work.
- Jim Crowley of Varian III-V Device Center for providing the oscillators used to test the distributed frequency doublers.
- The Office of Naval Research for providing me with a 3 year fellowship that motivated me to apply to Stanford University.

This work was supported by Defense Advanced Research Projects Agency (DARPA) / Office of Naval Research (ONR) contract N00014-89-J-1842, Air Force Office of Scientific Research (AFOSR) contract F49620-88-C-0103, and ONR contract N00014-85-K-0381.

I dedicate this dissertation to my wife Diane, whose patience and encouragement allowed me to complete it in a timely fashion.

# Contents

<b>Abstract</b>	<b>iv</b>
<b>Acknowledgements</b>	<b>v</b>
<b>1 Introduction</b>	<b>1</b>
1.1 Broad-band instrumentation . . . . .	1
1.2 Recent advances in broad-band measurement . . . . .	3
1.2.1 Electrooptic sampling . . . . .	4
1.2.2 The nonlinear transmission line . . . . .	5
1.3 Overview of this thesis . . . . .	7
<b>2 GaAs processing</b>	<b>11</b>
2.1 Introduction . . . . .	11
2.2 Diode fabrication . . . . .	12
2.3 Capacitors and airbridges . . . . .	13
2.4 Design rules . . . . .	16
<b>3 High-speed sampling</b>	<b>22</b>
3.1 Introduction . . . . .	22
3.2 Sampling theory . . . . .	25
3.2.1 Qualitative discussion . . . . .	25
3.2.2 Intermediate frequency response . . . . .	26
3.2.3 Input frequency limitations . . . . .	31
3.3 Monolithic samplers . . . . .	34

3.3.1	Generation I . . . . .	34
3.3.2	Generation II . . . . .	42
3.3.3	Generation III . . . . .	47
<b>4</b>	<b>S-parameter test-set on a chip</b>	<b>57</b>
4.1	Introduction . . . . .	57
4.2	Directional sampler theory . . . . .	59
4.3	Monolithic directional sampler . . . . .	63
4.3.1	Design and layout . . . . .	63
4.3.2	Results . . . . .	65
<b>5</b>	<b>Distributed frequency multiplication</b>	<b>71</b>
5.1	Introduction . . . . .	71
5.2	The diatomic lattice . . . . .	72
5.3	Nonlinear analysis . . . . .	74
5.4	Losses on the distributed doubler . . . . .	75
5.5	Results . . . . .	78
5.6	Conclusion . . . . .	83
<b>6</b>	<b>Future directions</b>	<b>87</b>
6.1	Directional sampler rf probe . . . . .	87
6.2	Circuit interconnects for operation to 300 GHz . . . . .	88
6.3	Optical synthesis . . . . .	92

# List of Tables

2.1 Summary of design rules . . . . .	18
---------------------------------------	----

# List of Figures

1.1	General sampling system . . . . .	2
1.2	Simplified network analyzer block diagram . . . . .	4
1.3	Nonlinear transmission line schematic diagram . . . . .	5
1.4	Simulation of voltage waveforms at various positions on a NLTL . . . . .	6
2.1	Schottky diode plan-view and cross-section . . . . .	13
2.2	Airbridge and MIM capacitor process . . . . .	15
2.3	Completed airbridge and capacitor structures . . . . .	19
2.4	Proton straggle effect on width of active region . . . . .	20
3.1	Callendar's mechanized "null-seeking" sampling system . . . . .	23
3.2	Grove's two diode sampling bridge . . . . .	25
3.3	Simplified equivalent circuit of the two diode sampler . . . . .	27
3.4	Piecewise constant signal representation . . . . .	28
3.5	Intermediate frequency equivalent circuit and noise model. . . . .	30
3.6	Sampler equivalent circuit including diode parasitics . . . . .	32
3.7	Relationship between sampling aperture and voltage strobe pulse width . . . . .	33
3.8	Layout of Generation I sampler . . . . .	36
3.9	Diode layout for the Generation I sampler . . . . .	37
3.10	Risetime limiting factors of the Generation I sampler . . . . .	39
3.11	Generation I sampler strobe pulses . . . . .	40
3.12	Step response of the Generation I sampler . . . . .	41
3.13	Experimental set-up for measuring sampler response . . . . .	42
3.14	Sampler video response from 80 to 128 GHz . . . . .	43

3.15	Coplanar strip (CPS) nonlinear transmission line . . . . .	44
3.16	Sampler designed for the CPS NLTL . . . . .	45
3.17	Experimental set-up for conversion loss measurement of the Generation II sampler . . . . .	47
3.18	Conversion loss of the packaged CPS sampler . . . . .	48
3.19	Scanning electron micrograph of an on-chip NLTL diode . . . . .	49
3.20	Generation III sampler layout . . . . .	50
3.21	Scanning electron micrograph of the completed sampler . . . . .	51
3.22	Step response of the Generation III sampler . . . . .	52
3.23	Electrooptically sampled Generation III sampler strobe pulses . . . . .	53
3.24	Comparison of sampler risetime limiting factors . . . . .	54
4.1	Directional bridge schematic diagram . . . . .	58
4.2	Diagram illustrating how a floating voltage can be sampled . . . . .	60
4.3	Schematic diagram of directional bridge using a floating sampler . . . . .	61
4.4	Layout of the directional sampler . . . . .	64
4.5	Directional sampler S-parameter test set-up . . . . .	66
4.6	Uncalibrated S-parameter measurement with the directional sampler . . . . .	67
4.7	Directional sampler calibration . . . . .	68
5.1	Electrical analog of the diatomic lattice . . . . .	72
5.2	Dispersion relation of the diatomic lattice . . . . .	73
5.3	Radiation sources on the distributed doubler . . . . .	77
5.4	Layout of the distributed frequency doubler . . . . .	80
5.5	Experimental set-up for testing the monolithic doublers . . . . .	81
5.6	Theory and results for the 5-section doubler at 100 and 110 GHz . . . . .	82
5.7	Theory and results for the 17-section doubler at 100 and 110 GHz. . . . .	83
5.8	Proposed doubler using spatial power combining . . . . .	85
6.1	On-wafer probing with GaAs MMICs . . . . .	89
6.2	Optical frequency synthesizer . . . . .	94

# Chapter 1

## Introduction

### 1.1 Broad-band instrumentation

This thesis focuses on the application of GaAs integrated circuits to test instrumentation. This is appropriate since test instruments in general must be superior in performance to the systems or devices that are being tested; therefore, it is here that most high-performance circuits find their first, and sometimes only, application. Here *high-performance* can mean either high-speed or high-frequency. Such nomenclature can be confusing, as researchers working on the next generation of computers want an instrument that can measure fast transients (high-speed) while microwave and mm-wave engineers want broad-bandwidth (high-frequency) instrumentation. The primary distinction is that a large *instantaneous* bandwidth is necessary for time-domain applications while those thinking and working in the frequency domain typically only require operation at a single frequency, provided the instrument can be rapidly adjusted to operate at a new frequency or set of frequencies. Optical communication systems defy even this loose definition since the fractional optical bandwidth is extremely small, yet very high-speed signals are transmitted. In this thesis, *broad-band* will describe a circuit, device, or instrument that provides either an instantaneous or adjustable bandwidth that is exceptionally large.

Most broad-band instruments first convert the waveform to be analyzed to a lower frequency before performing analysis. Sampling is preferred for this purpose

since conversion loss is independent of the local oscillator (LO) harmonic number, allowing a single low frequency low cost LO to be used for rf frequencies ranging from 1 to over 100 times the LO frequency. Another advantage of the 'flat' conversion loss is that periodic, non-sinusoidal waveforms may also be down-converted with low distortion. A general sampling system block diagram is shown in Fig. 1.1. The

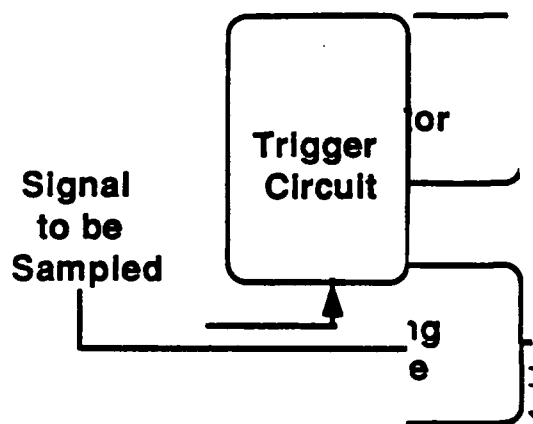


Figure 1.1: General sampling system block diagram. When the sampling device receives a pulse, a short sample is taken of the input signal. The phase relationship between the signal and the pulse generator is controlled by the trigger circuit.

trigger circuit detects a threshold crossing and, after a subsequent delay, sends a trigger pulse to the pulse generator, which turns on the sampling gate to take a short sample of the signal. If the trigger circuit generates the same delay after every threshold crossing, the same point in the rf signal will always be sampled and the hold capacitor will eventually charge up to the full rf voltage at this point in the waveform. If the trigger delay increases by a fixed amount between samples, the voltage on the hold capacitor will trace out the rf waveform at a lower frequency. The most obvious application of the sampling system is for the viewing of repetitive, high-speed waveforms. However, samplers find their way into many instruments.

Samplers can be found in sampling oscilloscopes, vector network analyzers, frequency synthesizers, spectrum analyzers, and frequency counters. Currently, the oscilloscope with the greatest bandwidth is the Hewlett-Packard (HP) 54124T which has a 3-dB bandwidth of 50 GHz [1.1]. This oscilloscope and its 34 GHz predecessor represent the first industrial application of the monolithic nonlinear transmission line (NLTL) technology developed by Rodwell and Madden [1.2,3] and discussed in §1.2.2. Wiltron, on the other hand, boasts the vector network analyzer with greatest bandwidth (60 GHz) using a conventional step-recovery-diode (SRD). Since the network analyzer measures normalized parameters, the samplers can be used well above their 3-dB bandwidth. The upper frequency limit is reached only when the signal-to-noise ratio at the receiver becomes unacceptable.

A simplified network analyzer block diagram is shown in Fig. 1.2. The automatic network analyzer (ANA) block diagram is very similar to that of the sampling oscilloscope. In fact, the same sampler design can be used for both applications. The major difference, besides the additional rf components of the ANA, is that the oscilloscope is a very general instrument and so few assumptions may be made about the input signal. So, typically, every sample must be individually processed. The ANA has a very specific task, which it is optimized to perform: the measurement of  $S$  (scattering)-parameters. In this case, the samples are not individually processed but rather integrated on a hold capacitor as in Fig. 1.1. The samplers used in frequency synthesizers, frequency counters, and spectrum analyzers are used as frequency converters, as in the ANA. The samplers studied in this thesis work were evaluated in terms of both ANA and oscilloscope applications.

## 1.2 Recent advances in broad-band measurement

This section briefly describes two new technologies which provided the motivation for this thesis work: electrooptic sampling and the nonlinear transmission line. Electrooptic sampling with its tremendous bandwidth issued a challenge: what electronic device can be fast enough to require such bandwidth? The nonlinear transmission line responded and in doing so made possible an all-electronic sampler with

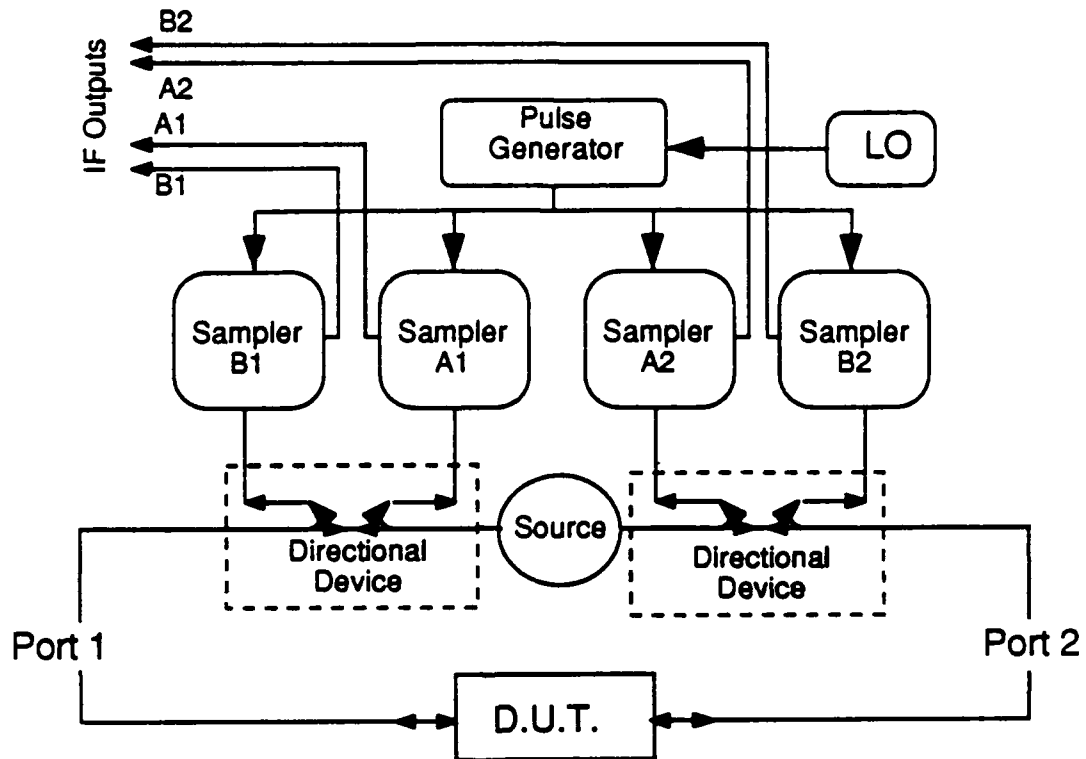


Figure 1.2: Simplified automatic network analyzer block diagram. Directional couplers send portions of the incident and reflected signals to the four samplers where they are down-converted to an intermediate frequency (IF) for further processing.

even greater bandwidth. The all-electronic sampler, its applications, and variations on the nonlinear transmission line are the subjects of this thesis. A description of electrooptic sampling and the nonlinear transmission line is included here for completeness.

### 1.2.1 Electrooptic sampling

Electrooptic (EO) sampling is an optical probing technique that takes advantage of the short pulse width available from an ultra-fast pulsed laser to provide temporal

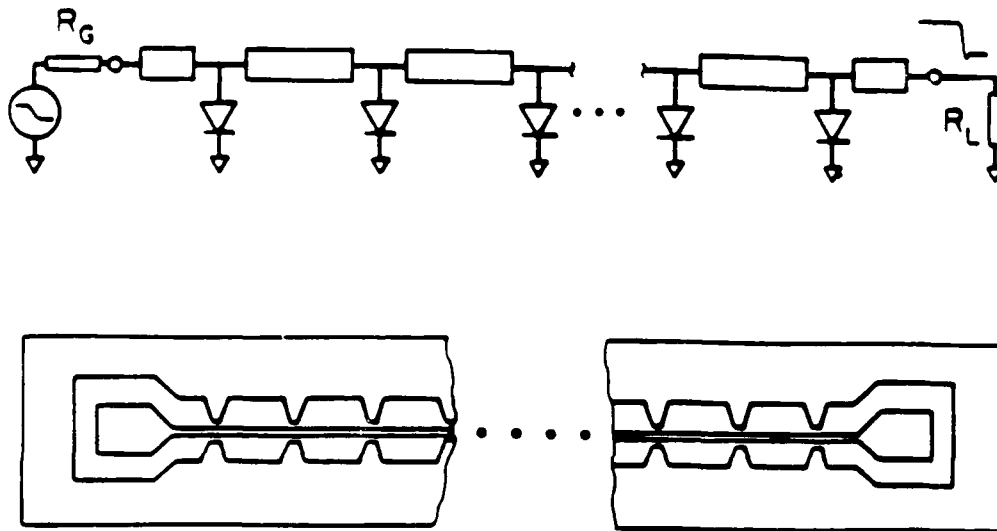


Figure 1.3: Nonlinear transmission line schematic diagram. The inductance of the series high impedance transmission lines and the capacitance of the reverse biased diodes forms a synthetic transmission line with a propagation velocity that is a function of voltage. After Rodwell et al.

resolution on the order of 1 ps or less. The optical beam can interact with an electrical signal by passing through an EO crystal brought sufficiently close to the signal conductor to sense its electric field [1.4,5,6]. Alternatively, when the conductor to be probed is patterned on an electrooptic substrate such as GaAs, the substrate itself can provide the EO interaction [1.7]. The latter technique was developed by Weingarten and Rodwell [1.8,9,10] into a system which can provide internal node probing of GaAs integrated circuits under realistic excitation and loading conditions with a bandwidth of approximately 200 GHz. This system was used extensively for evaluating the circuits described in this thesis.

### 1.2.2 The nonlinear transmission line

The nonlinear transmission line (NLTL), shown schematically in Fig. 1.3, is a relatively high impedance transmission line periodically loaded with reverse biased

Schottky diodes serving as voltage-dependent shunt capacitances [1.11,12,13]. Because the capacitance decreases with increasing reverse bias, the phase velocity of a small signal will be slower when the line is biased near zero volts than when it is strongly reverse biased. If a large gradual-step signal is applied to the line, points on the waveform with amplitude near zero will experience a greater delay than the more negative portion. Therefore, the step will tend to steepen as it propagates. The simulated NLTL waveforms in Fig. 1.4 illustrate this process, known as shock-

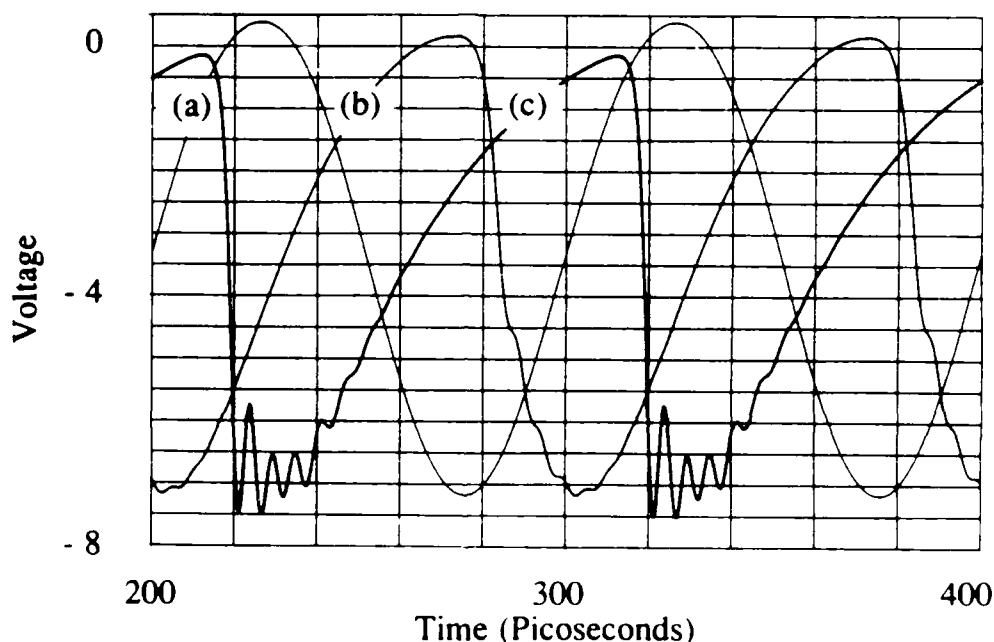


Figure 1.4: Simulation of voltage waveforms at various positions on a NLTL. The input is a 10 GHz  $8V_{pp}$  sinusoid (a). After 15 diode sections, a shock-wave begins to form near zero volts (b). After 30 diodes, shock wave formation is nearly complete (c). Figure courtesy of C.J. Madden.

wave formation. A comparison of waveforms (a) and (b) shows that the portion of the waveform near zero volts, where the change in delay is greatest, steepens first. At point (c) the entire falling edge has been sharpened. The steepening process continues until spreading due to dispersion just balances the compression arising from the nonlinear capacitance.

The two dominant sources of dispersion are line periodicity and device parasitics.

If the diodes are close enough together, so that the filter cutoff is high, the bandwidth of the line will be limited by the RC time constant of the diodes rather than the filter cutoff. Since Schottky diodes have been fabricated with RC time constants as low as 18 fs [1.14], there is the potential for subpicosecond falltimes. The *monolithic* NLTL circuit [1.2,3] is implemented in coplanar waveguide to reduce the parasitic inductance of the shunt diode connection. Processing is also simplified since vias and back-side metalization are not required.

The monolithic NLTL is fabricated on semi-insulating GaAs with the active layers grown by molecular-beam epitaxy. A heavily doped  $N^+$  buried layer provides the diode cathode connection and shorts the two ground planes of the CPW together to suppress the unwanted even CPW mode. The doping profile of the top  $N^-$  layer determines the capacitance and resistance per unit area of the diode. This profile is tailored to provide the lowest RC time constant possible, while achieving the desired change in capacitance with voltage.

### 1.3 Overview of this thesis

The major contributions of this thesis include:

- First application of the monolithic nonlinear transmission line technology to high-speed sampling.
- Fastest all-electronic sampler ( $< 1.6$  ps risetime).
- First monolithically integrated directional bridge with samplers.
- Generation of 100-110 GHz radiation by phase-matched frequency multiplication on a NLTL.

The process technology which is common to all of the ICs of this thesis is described in Chapter 2. Sampling theory and the three design iterations on monolithic sampling bridges are discussed in Chapter 3. The monolithic integration of two samplers with a directional bridge is presented in Chapter 4. Phase matched second harmonic generation of a nonlinear transmission line is studied theoretically

with coupled-mode theory and experimentally by electrooptic sampling in Chapter 5. The conclusion and some possible future work are contained in Chapter 6.

## References

- [1.1] Hewlett-Packard Company, P.O. Box 10301, Palo Alto, CA. 94303.
- [1.2] M.J.W. Rodwell, "Picosecond electrical wavefront generation and picosecond optoelectronic instrumentation," *Ph.D. Thesis*, Stanford University, Stanford CA, 1988.
- [1.3] C.J. Madden, R.A. Marsland, M.J.W. Rodwell, D.M. Bloom, and Y.C. Pao, "Hyperabrupt-doped GaAs nonlinear transmission line for picosecond shock-wave generation," *Appl. Phys. Lett.*, **54**, 1019-1021, 1989.
- [1.4] J.B. Gunn, "Sampling system utilizing electrooptic techniques," U.S. Patent no. 3,614,451, issued Oct. 1971.
- [1.5] J.A. Valdmanis, G.A. Mourou, and C.W. Gabel, "Picosecond electro-optic sampling system," *Appl. Phys. Lett.*, **41**, 211-212, 1982.
- [1.6] B.H. Kolner, B.M. Bloom, and P.S. Cross, "Electro-optic sampling with picosecond resolution," *Electr. Lett.*, **19**, 574-575, 1983.
- [1.7] B.H. Kolner and D.M. Bloom, "Direct electro-optic sampling of transmission line signals propagation on a GaAs substrate," *Electr. Lett.*, **20**, 818-819, 1984.
- [1.8] K.J. Weingarten, M.J.W. Rodwell, and D.M. Bloom, "Picosecond optical sampling of GaAs integrated circuits," *IEEE J. of Quant. Electr.*, **QE-24**, 198-220, 1988.
- [1.9] K.J. Weingarten, "Gallium arsenide integrated circuit testing using electrooptic sampling," *PhD Thesis*, Stanford University, Stanford, CA.1987
- [1.10] M.J.W. Rodwell, K.J. Weingarten, D.M. Bloom, T. Baer, and B.H. Kolner, "Reduction of timing fluctuations in a mode-locked Nd:YAG laser by electronic feed-back," *Optics Letters*, **11**, 638-640, 1986.
- [1.11] S.T Peng and R. Landauer, "Effects of dispersion on steady state electromagnetic shock profiles," *IBM J. Res. and Dev.*, **17**, 4, 1973.

- [1.12] D. Jager and F.-J. Tegude, "Nonlinear wave propagation along periodic-loaded transmission lines," *Appl. Phys.*, **15**, 1978.
- [1.13] D. Jager, "Characteristics of travelling waves along the non-linear transmission line for monolithic integrated circuits: a review," *Int. J. Elect.*, **58**, 4, 1985.
- [1.14] C.O. Weiss and A. Godone, "Harmonic mixing and detection with schottky diodes up to the 5 THz range," *IEEE J. of Quant. Electr.*, **QE-20**, 2, 1984.

# Chapter 2

## GaAs processing

### 2.1 Introduction

The bandwidth of the circuits discussed in this thesis relies, at least in part, on the RC cut-off frequency of the Schottky diodes. Low-loss transmission lines, airbridge interconnects, and  $N^+$  resistors are also required. In addition, it is important to understand the constraints imposed by the process technology before a circuit design is finalized. Very often a small change in the circuit design which has a minimal impact on the circuit function but will greatly increase the yield of the completed circuits. Similarly, there may be a small adjustment in the physical layout which significantly improves the high-frequency circuit performance. An understanding of the process constraints and their origins allows the proper balance to be struck between circuit performance, yield, and processing difficulty. This chapter contains a description of the process developed to satisfy these demands. Monolithic diode fabrication steps developed by Rodwell and Madden [2.1,2] are discussed first. Airbridges and metal-insulator-metal capacitors added for the purposes of this thesis are described next. Design rules are described in the last section. The entire process was developed in accordance with standard industry practices to keep things simple and facilitate technology transfer.

## 2.2 Diode fabrication

The starting material for this process is semi-insulating [100] GaAs polished on both sides to allow EO sampling by backside probing (see §1.2.1). The active layers consist of a heavily doped  $N^+$  layer and a more moderately doped  $N^-$  layer grown by molecular-beam-epitaxy (MBE). The underlying  $N^+$  layer, typically  $0.8 \mu\text{m}$  thick, provides the diode cathode connection, while the  $N^-$  layer determines the capacitance and resistance per unit area of the diode. This profile is tailored to provide the lowest RC time constant possible, while achieving the desired change in capacitance with voltage. With the thick layers required for Schottky diodes, other epitaxial techniques may be used, but MBE material is readily available because of our collaboration with Yi-Ching Pao of Varian III-V Device Center. Specific diode designs are discussed in later chapters.

A typical Schottky plan-view and cross-section are shown in Fig. 2.1. The layer structure shown in this figure was used for sampler Generations I and II but was modified for Generation III. Ohmic contacts are formed by etching down to the  $N^+$  layer and performing a self-aligned liftoff of  $108\text{\AA}$  Ge/ $102\text{\AA}$  Au/ $63\text{\AA}$  Ge  $236\text{\AA}$  Au/ $100\text{\AA}$  Ni/ $x\text{\AA}$  Au, where  $x$  is the thickness required to fill the etch-well. After liftoff, the contacts are annealed for 25 seconds at  $450^\circ\text{C}$ . Isolation between diodes is achieved with a multienergy proton implant. During implantation, the active areas are protected by  $1.8 \mu\text{m}$  of Au on  $1.4 \mu\text{m}$  of polyimide. Isolation provided by the proton damage is  $> 40\text{M } \Omega/\square$ . After implant, the Au mask is stripped by dissolving the polyimide in its solvent.

Schottky contacts and interconnects are simultaneously patterned with a liftoff of  $1000\text{\AA}$  Ti/ $750\text{\AA}$  Pt/ $1.4 \mu\text{m}$  Au. Schottky diodes are formed where the center conductor crosses over an undamaged active region. Using the same metalization for Schottky contacts as interconnect metal saves one mask step and the need for alignment. Unfortunately, it is difficult to make small ( $< 2 \mu\text{m}$ ) diodes, since the interconnect metal must be thick for low microwave loss. For the very highest performance sampler described in §3.3.3, the patterning was separated into two mask steps. A thin metal was used for the small geometry diodes while a thick metal with

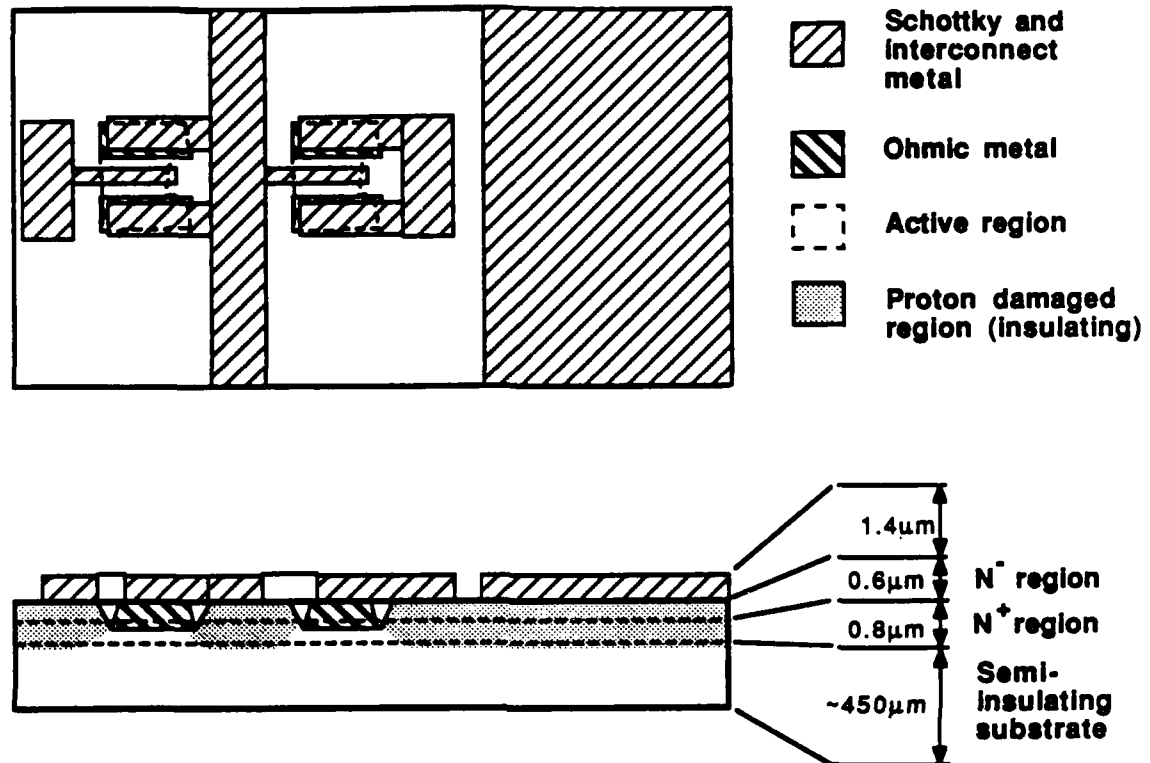


Figure 2.1: Two Schottky diodes are shown in plan-view (top) and cross-section (bottom). The layout shown here is typical for switching diodes.

lower titanium content was used for interconnect metal.

### 2.3 Capacitors and airbridges

The three masks steps of the diode fabrication process of §2.2 are sufficient for nonlinear transmission line fabrication, but metal-insulator-metal (MIM) capacitors and airbridges are needed to add a sampling bridge. Silicon nitride (also called just *nitride* or  $Si_3N_4$ ), deposited by plasma-enhanced chemical vapor deposition (PECVD) was chosen as the capacitor dielectric because it has a high dielectric constant  $\sim 7.3$ , provides some scratch protection, and is used extensively in industry.

The nitride must be deposited at relatively low temperature to avoid degradation of the Schottky junction [2.3]. At a deposition temperature of  $290^{\circ}\text{C}$  the Schottky diode breakdown voltage was reduced from 18 V to 10 V. At  $350^{\circ}\text{C}$ , the breakdown voltage was reduced to 4 V. Deposition temperatures below  $275^{\circ}\text{C}$  caused only small ( $\sim 1\text{V}$ ) degradation. Producing high quality nitride at such a low temperature is difficult. However, Gerald Li, then at Varian III-V Device Center, had already developed a low-temperature nitride process and was willing to perform the deposition himself. Nitride can be etched with hydrofluoric or phosphoric acid solutions [2.4]. Unfortunately, the etch rate is low ( $\sim 10\text{\AA}/\text{min}$ ) and the titanium sticking layer used for the Schottky contacts is attacked. Dry-etching in a  $\text{C}_2\text{F}_6$  plasma, on the other hand, provides very reasonable etch rates ( $\sim 300\text{\AA}/\text{min}$ ) without significant damage to other films on the substrate. Surface damage due to physical sputtering is not a problem since the active regions are protected by metal or photoresist or both.

Once contact holes have been opened through the nitride, a  $1.6\ \mu\text{m}$  layer of photoresist is patterned to define where airbridges will contact the underlying metal (Fig. 2.2). This resist is hard-baked for 20 minutes at  $120^{\circ}\text{C}$  to cause the resist to flow slightly and provide sloping resist sidewalls. A  $100\text{\AA}\text{Ti} / 2000\text{\AA}\text{Au} / 300\text{\AA}\text{Ti}$  film is then evaporated. This metal will be the current carrying layer for later electroplating. The titanium layers improve adhesion to the photoresist above and below. The thick gold layer is necessary to avoid breaks at resist edges. A thinner layer could be used if it was sputtered rather than evaporated. Finally, a  $4\ \mu\text{m}$  layer of resist defines where the thin gold layer is to be plated.

The  $300\text{\AA}$  layer of Ti is etched in a weak (10:1)  $\text{H}_2\text{O} : \text{HF}$  solution immediately prior to plating. This keeps the gold vacuum clean until it is ready to be plated. Once the gold is exposed, it is plated to a thickness of 2.3 to  $3.0\ \mu\text{m}$ . After plating, the upper level resist is removed by spraying the surface with acetone. The Ti/Au/Ti film is then removed with weak HF and gold etchants. Finally, the underlying resist is removed with an overnight soak in acetone. The completed structure is shown in Fig. 2.3.

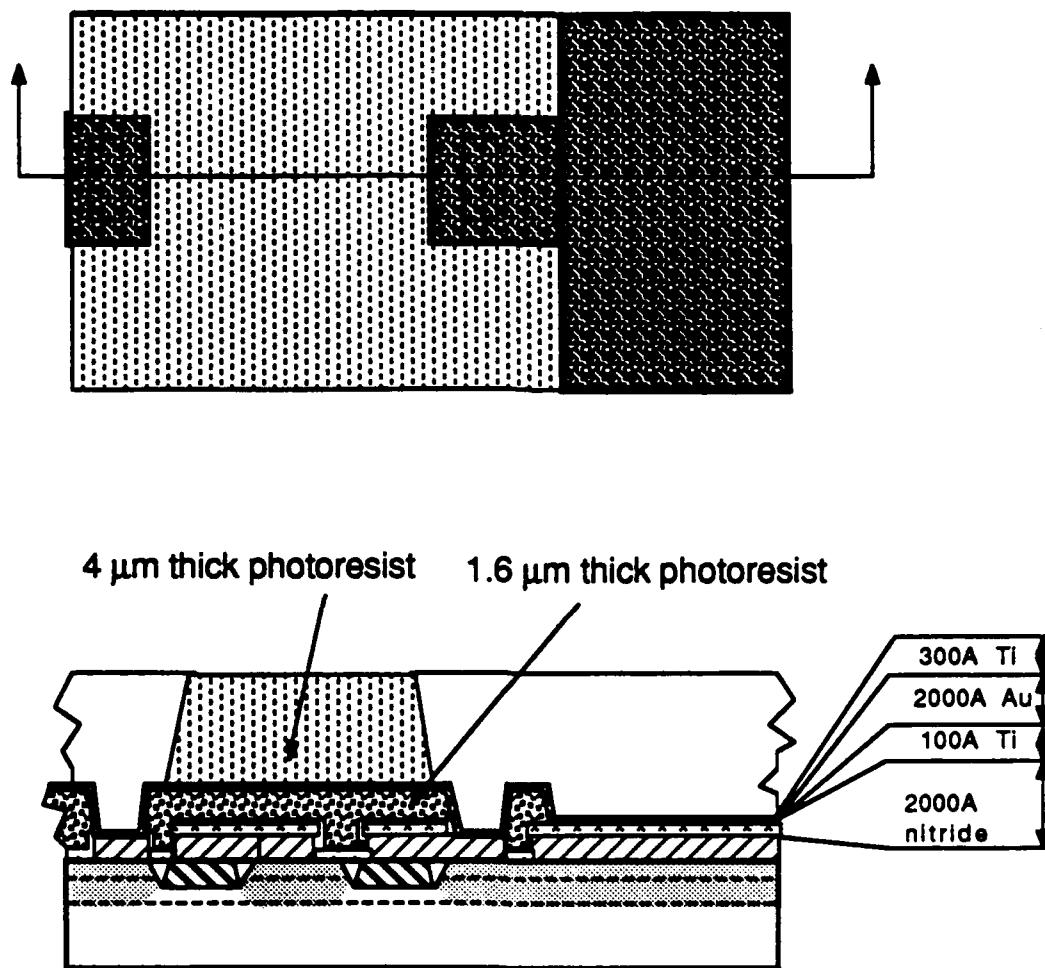


Figure 2.2: Airbridge and MIM capacitor process. The lower layer of resist defines where the airbridges will contact the underlying metal or nitride and acts as a temporary support for the metal which is evaporated next. The final layer of photoresist defines the regions to be plated.

## 2.4 Design rules

Designing an integrated circuit to minimize the effects of parasitics often results in layout geometries which are difficult to fabricate. Therefore, it is important to understand the constraints imposed by the fabrication process before committing to a particular design. It is usually better to design around a process problem than to process around a design problem.

Ohmic contacts to the  $0.8 \mu\text{m}$   $N^+$  layer doped  $3 \times 10^{18} \text{cm}^{-3}$  prepared by alloying a Au/Ge/Ni/Au film, as described in §2.2, routinely achieve  $0.035 \Omega\text{mm}$  contact resistance with a standard deviation of  $0.015 \Omega\text{mm}$  over the wafer. The sheet resistance of the  $N^+$  layer is typically  $9.6 \Omega/\square$  with a standard deviation of  $0.4 \Omega/\square$  across the wafer although actual resistance can vary with the width of the active region. In three wafer runs, the average sheet resistance of the  $N^+$  layer was 8.6, 11.7, and  $9.6 \Omega/\square$  for an overall average of  $10 \Omega/\square$  and a deviation of  $1.6 \Omega/\square$ . The active region width dependence is most likely because the protons can "straggle" underneath the implant mask, reducing the width of the undamaged region (Fig. 2.4). In practice, a  $5 \mu\text{m}$  wide resistor has a resistance per square of  $N^+$  material that is approximately 20% higher than a  $100 \mu\text{m}$  wide resistor. This indicates a proton straggle of approximately  $0.5 \mu\text{m}$  on each side, which is approximately 50% of the vertical proton projected range.

If allowance is made for straggle, the major source of error in resistance values will be due to variation in contact resistance. To minimize this effect, the contacts should be made as large as possible. For example, a  $50 \Omega$  resistor designed to have  $5 \mu\text{m}$  wide ohmic contacts and use 3 squares of material would have a tolerance of

$$2 \frac{0.035 \Omega\text{mm}}{0.005\text{mm}} \times 43\% + 3 \square \times 12 \Omega/\square \times 16\% = 24\%$$

whereas a resistor with  $20 \mu\text{m}$  wide ohmic contacts and 4.6 squares of material would have a 18% tolerance.

Another problem with small ohmic contacts is that they tend to fail at approximately  $17 \text{mA}/\mu\text{m}$  of design width. This failure is probably due to electron velocity saturation at some point in the resistor. Any additional voltage beyond the onset of saturation will drop across the region of saturated velocity. Power dissipation

will therefore increase in this small region until the power density exceeds what the material can bear. Assuming an elevated temperature saturation velocity of  $0.5 \times 10^7 \text{ cm/s}$  [2.5] and a cross-sectional area of

$$0.65 \mu\text{m} (N^+ \text{ thickness} - \text{ohmic recess over-etch}) \times 3 \mu\text{m} (\text{ohmic contact width})$$

gives a saturation current of 47 mA. This agrees well with the observed failure of a  $3 \mu\text{m}$  ohmic at 55 mA after saturating at 50 mA.

The small capacitors required in high-frequency circuits do not present nearly the design problem as resistors. When the nitride thickness is greater than  $1000 \text{ \AA}$ , shorts through pin-holes in the nitride are not a problem for capacitors smaller than 2 pF. It is important, however, to keep the top plate of the capacitor away from the edge of the bottom plate to avoid possible voids in the nitride on the metal edge.

The remaining design rules are related to lithography. For thick metal lift-off [2.1] used for interconnect metal, the minimum line width and space are 2 and  $3 \mu\text{m}$ , respectively. Thin metal, which was added for the Generation III sampler, can achieve  $1 \mu\text{m}$  lines and  $2 \mu\text{m}$  spaces. Airbridge metal can only attain  $5 \mu\text{m}$  lines and spaces because of the very thick photoresist used and the difficulty of clearing the post holes all the way down to the underlying metal. The design rules for this process are summarized in Table 2.1.

Design Rules		
Resistors	Maximum current per micron width	10 mA
	Minimum width	5 $\mu\text{m}$
	Allowance for proton straggle	1 $\mu\text{m}$
	Ohmic contact resistance	$0.035 \pm 0.015 \Omega\text{mm}$
	$N^+$ layer sheet resistance	$10 \pm 1.6 \Omega/\square$
Capacitors	Maximum size	2 pF
	Top plate clearance from bottom plate edge	2 $\mu\text{m}$
Metal	Thick metal minimum line / space	2 / 3 $\mu\text{m}$
	Thin metal minimum line / space	1 / 2 $\mu\text{m}$
	Airbridge minimum line / space	5 / 5 $\mu\text{m}$
All layers	Alignment tolerance	$\pm 0.5 \mu\text{m}$

Table 2.1: Summary of design rules for circuits fabricated using the process outlined in this chapter.

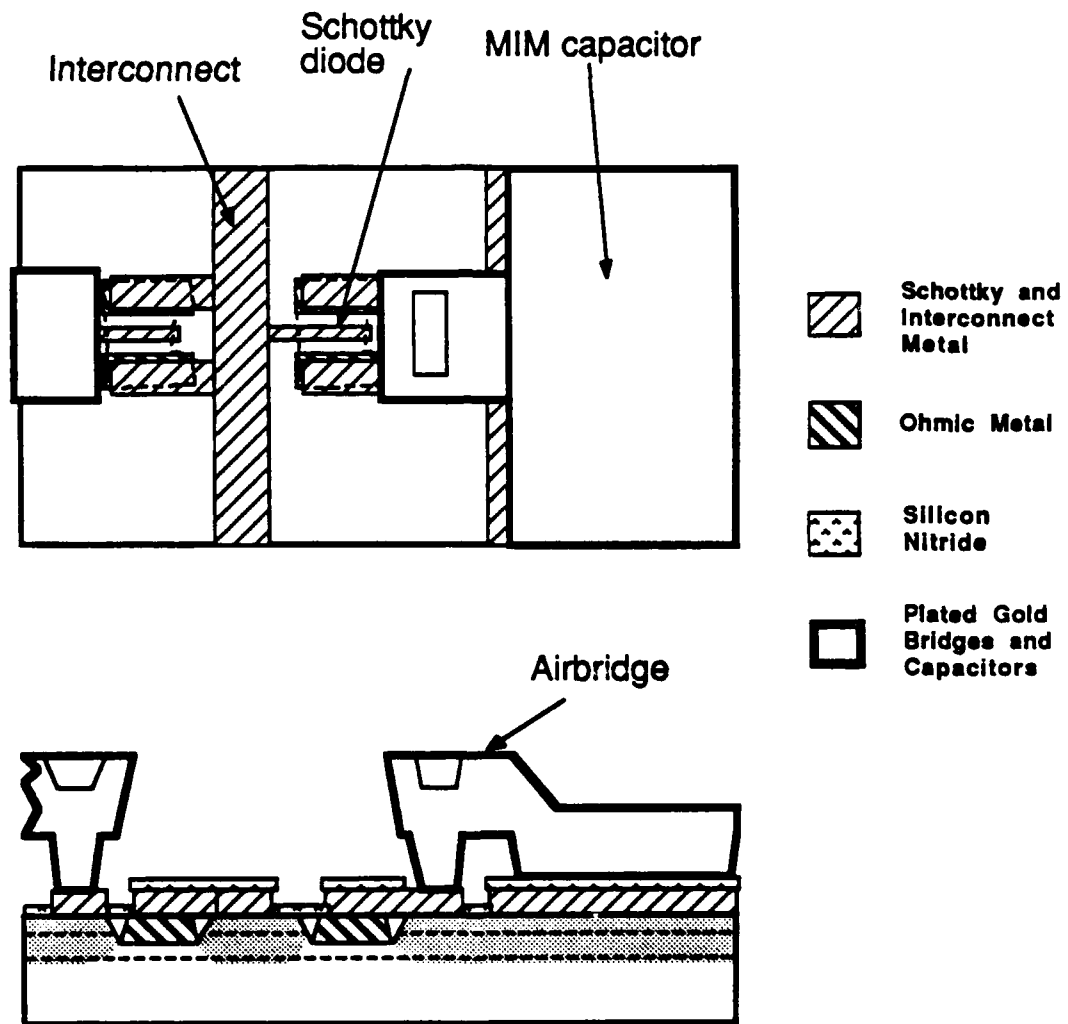


Figure 2.3: Completed airbridge and capacitor structures.

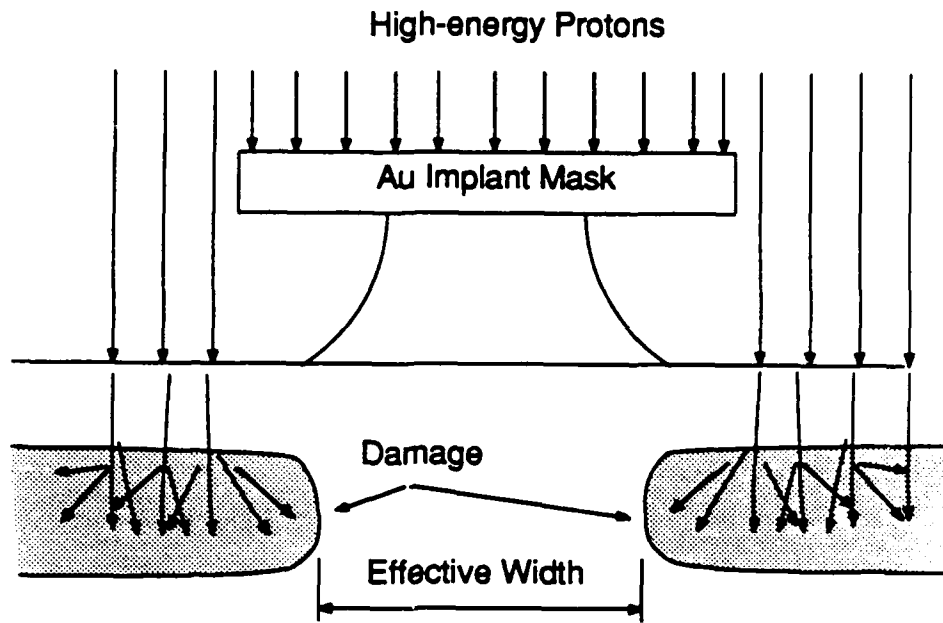


Figure 2.4: Proton straggle effect on width of active region

## References

- [2.1] M.J.W. Rodwell, "Picosecond electrical wavefront generation and picosecond optoelectronic instrumentation," *Ph.D. Thesis*, Stanford University, Stanford CA, 1988.
- [2.2] M.J.W. Rodwell, C.J. Madden, B.T. Khuri-Yakub, D.M. Bloom, Y.C. Pao, N.S. Gabriel, S.P. Swierkowski, "Generation of 7.8ps electrical transients on a monolithic nonlinear transmission line," *Electr. Lett.*, **24**, 100-101, 1988.
- [2.3] H.J. Howes and D.V. Morgan, editors, *Gallium Arsenide: Materials, Devices, and Circuits*, Wiley-Interscience, New York, (1985).
- [2.4] S. Wolf, R.N. Tauber, *Silicon processing for the VLSI era Volume 1. Process Technology*, Lattice Press, Sunset Beach, CA, (1986).
- [2.5] S.M. Sze, *Physics of semiconductor devices*, Wiley-Interscience, New York, (1981).

## Chapter 3

# High-speed sampling

### 3.1 Introduction

Sampling has long been used as a means of measuring phenomena that occur on a time scale shorter than the response time of existing instrumentation. In electronics, possibly the earliest "sampler" was the "cycle contact maker". This instrument placed a potentiometer across a bipolar dc voltage source. The sliding contact was connected through a galvanometer to the output of an ac power generator. This contact was made for only a small fraction of every ac cycle. The sliding contact was then adjusted manually over many cycles for zero deflection of the galvanometer, at which point the generator voltage could be determined at this particular instant in its cycle by the position of the potentiometer's sliding contact. Credit for the first sampling system should probably go to H.L. Callendar [3.1] who combined the "cycle contact maker" with a "recording potentiometer" and a synchronous motor to provide automatic recording of the potentiometer position as the relative phase of the contact maker was gradually advanced. In this instrument, the galvanometer was replaced by a relay that connected a servo motor to the bipolar dc voltage source (Fig. 3.1). The servo motor automatically adjusted the sliding contact to null the voltage across the relay coil, and the contact position was automatically recorded by a pen attached to the potentiometer's sliding contact so as to trace out the generator waveform on a strip recorder. A remarkable thing about this invention is not only

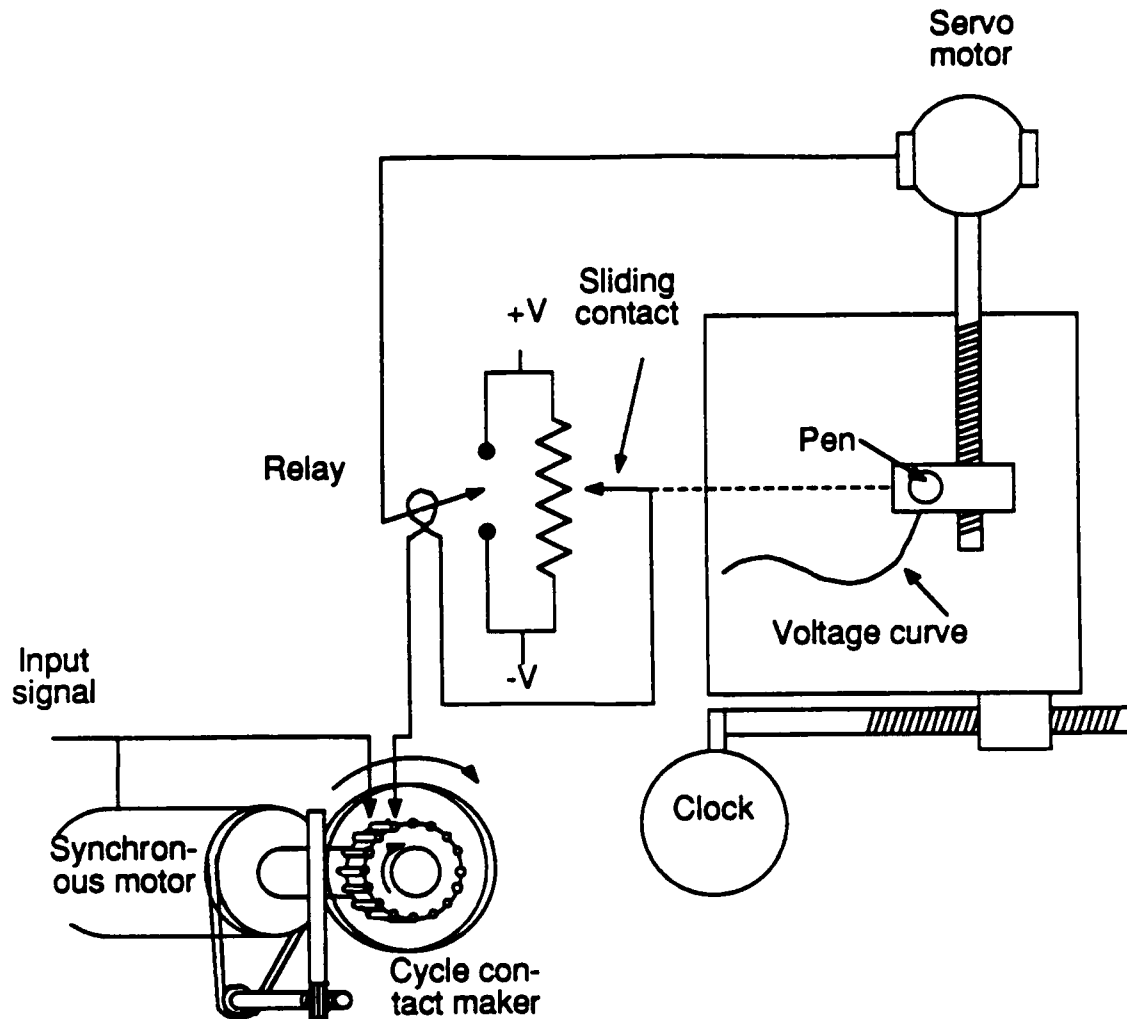


Figure 3.1: Callendar's mechanized "null-seeking" sampling system. The servo-motor adjusts the potentiometer sliding-contact position to null the voltage across the relay coil and record the instantaneous voltage with a pen connected directly to the bridge wire.

its ability to record 'high-frequency' waveforms, but also its inherent accuracy due to the null-seeking technique.

To make his "alternating cycle curve recorder" Callendar had to confront many of the same issues as today's sampling oscilloscope designer. He used the potentiometer to provide a null-seeking system that would be tolerant of the inevitable variations in contact resistance and avoid errors due to device nonlinearities and hysteresis. He realized that although contact resistance would not effect the accuracy directly, it

would "make the pen lag behind the correct reading, owing to want of quickness in responding." The quickness in responding is now called "dot-response" (response to a single sample) or "sampling efficiency." The recording drum rotation was controlled by a clock, while the phase advance was controlled by a synchronous motor which played the role of today's "time-base" and "trigger-recognizer."

Reeves [3.2] provides a history of stroboscopic sampling from the time of Callendar through the two and four diode sampling bridges and divides the various instruments into two classes: open loop (class 1) and closed loop (class 2). Reeves goes on to describe his own machine [3.3] which he claims is the first class 2 strobing oscilloscope. His work is emphasized here because it contains all of the elements and addresses most of the problems of even the most modern sampling oscilloscope. With the possible exception of random sampling [3.4] and the traveling wave bridge [3.5], contributions to this field since Reeves have involved the application of new technologies and new circuit design techniques to the basic circuits and functional blocks discussed by Reeves. The work presented in this chapter is no exception. Gallium Arsenide (GaAs) integrated circuit technology and microwave design techniques are applied to the sampling gate to produce a ten times improvement in bandwidth over the state of the art.

Although the history of the sampling gate is long, the design techniques presented in the literature are either highly qualitative or only apply for a specific signal processing technique. In addition, many major contributors to the development of high-speed sampling have either never published their work or have reported in obscure corporate publications. This is possibly because most of the 'art' of sampler design is considered proprietary by those working in the field. Grove's analysis [3.6] is quite thorough for the rf design, but does not derive the IF response. An attempt is made in the following sections to cover sampler theory at the level necessary for design.

## 3.2 Sampling theory

### 3.2.1 Qualitative discussion

A general sampling system was considered in §3.1. For a more detailed look at the sampling bridge operation, Fig. 3.2 shows the sampling bridge structure used

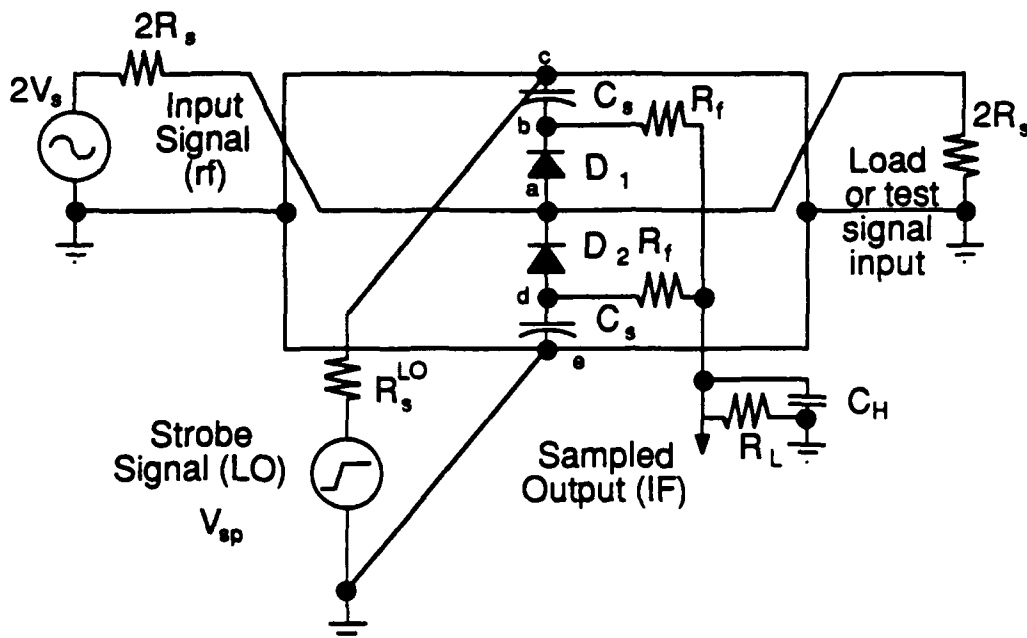


Figure 3.2: Grove's two diode sampling bridge. The signal to be sampled is input from the left and travels to the right. The sampled signal is stored on the sampling capacitors. A test signal may be brought in from the right, or the port may be terminated.

in 1966 by Grove in Hewlett-Packard's 12 GHz sampling oscilloscope [3.6]. This was the first major step of the sampling scope into the microwave regime and is illustrative of modern sampling techniques. The signal to be sampled is input from the left and travels through the sampling structure. The ground of the signal line is

split and the sampling diodes are placed across the gap in series with two coupling capacitors. The step, which is to drive the sampling diodes is applied across this split in the signal ground which acts a balanced transmission line that is shorted at both ends. This shorted transmission line differentiates the input step function so that the voltage applied across the diodes is impulse like. The pulses will also be balanced with respect to the signal line so that there is little coupling between the strobe generator line and the signal line.

If the strobe pulses are synchronous with the rf signal, the samples will always be taken at the same time,  $t_0$ , in the rf waveform. The capacitors will charge up a small amount during each sample period until node (d) charges to  $-\frac{V_{sp}}{2} + V_s(t_0)$  and node (b) charges to  $\frac{V_{sp}}{2} + V_s(t_0)$ . The IF output into an open circuit will then be  $V_s(t_0)$ , where  $t_0$  is the time of arrival of the sampling pulse. If the rf frequency is offset by a small amount from a harmonic of the pulse repetition rate, the output will trace out the rf input at the offset frequency.

### 3.2.2 Intermediate frequency response

For further consideration of the IF response, Grove's sampler can be represented by the circuit shown in Fig. 3.3, where the sampling diode has been replaced by an ideal switch with resistance  $(R_d + R_j)/2$ , which represents the parallel combination of the two sampling diodes' ohmic resistance  $R_d$  and junction resistance  $R_j$  when the diodes are 'on',  $R_s$  is the equivalent source resistance,  $C_H$  is the hold capacitance,  $R_L$  is the load resistance on the IF port, and  $V_s$  is a periodic voltage source with fundamental frequency  $f_{rf}$ . When the switch is closed, the current through the sample capacitor  $C_s$  will increase rapidly. The small filter resistance  $R_f$  isolates this high-speed waveform from the low-frequency components connected to the IF output port. Once the switch reopens, the charge on  $C_s$  will redistribute between  $C_s$  and  $C_H$ . The net effect is the same as if the two capacitors were connected in parallel, but high-frequency resonances in the IF circuitry are isolated from the high-speed switch. For the remainder of this analysis,  $R_f$  will be neglected.

Since the switch will only be closed for a small fraction of the input signal cycle,  $V_s$  can be replaced with a *piecewise constant* source  $V'_s$  which only changes value at

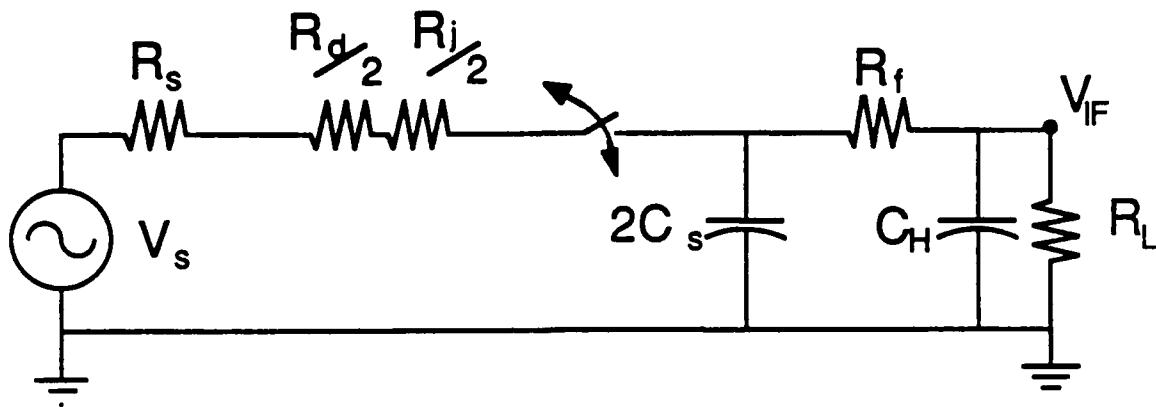


Figure 3.3: Simplified equivalent circuit of the two diode sampler.

the moment the switch is closed,  $t_m$ . So

$$V'_s(t) = \begin{cases} V_s(t) & \text{if } t = t_1, t_2, \dots \\ V_s(\text{int}(t/\Delta t)\Delta t) & \text{otherwise} \end{cases} \quad (3.1)$$

where  $\text{int}()$  means integer part and  $\Delta t$  is the time between switch closings. The strobe pulse repetition rate, also called the local oscillator (LO) frequency, is

$$f_{LO} = \frac{1}{\Delta t}$$

An example of an rf waveform and its piecewise constant representation is shown in Fig. 3.4. Now let the fundamental frequency component of  $V'_s$  be

$$f_{IF} = qf_{LO} - f_{rf}$$

where  $q$  is an integer, so that  $V'_s$  has a repetition rate of  $f_{IF}$ . So, assuming that  $f_{IF}$  is sufficiently small,  $V'_s$  is varying much more slowly than the sampling rate, and the circuit of Fig. 3.3 can be analyzed as a switched capacitor filter [3.7].

The output voltage,  $V_{IF}$  after the  $m + 1$  sample is equal to that after the  $m$ th sample plus the voltage change due to current integrated by capacitor  $C_H + 2C_s$ ,

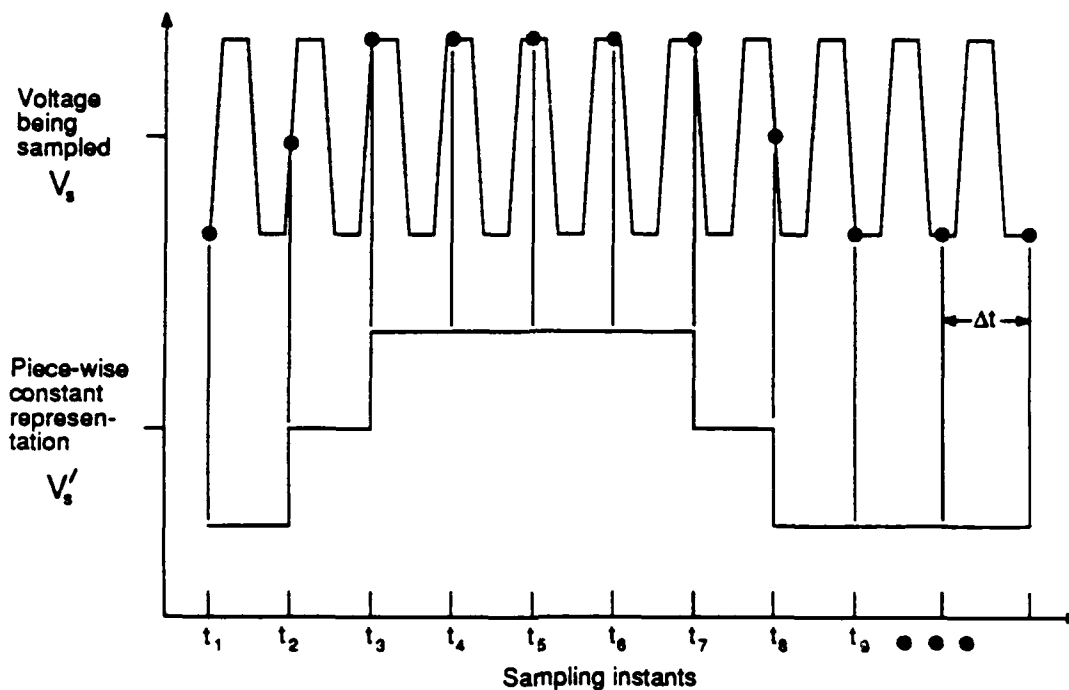


Figure 3.4: Piecewise constant sampled signal representation.

during the  $m + 1$  sample, minus that due to the current leaking off through resistor  $R_L$  between samples. Assuming that the sampling interval  $t_{on}$  is much less than the charging time constant  $\tau_f$ ,

$$t_{on} \ll \tau_f = (C_H + 2C_s) \frac{R_L(R_s + R_d/2 + R_j/2)}{R_L + R_s + R_d/2 + R_j/2}$$

and that the time between samples  $\Delta t$  is much less than the slow leakage time constant  $\tau_s$ ,

$$\Delta t \ll \tau_s = R_L(C_H + 2C_s)$$

$V_{IF}$  after the  $m + 1$  sample may be written

$$V_{IF}^{(m+1)} = V_{IF}^{(m)} + \frac{t_{on}}{\tau_f} (V_s' - V_{IF}^{(m)}) - \frac{\Delta t}{\tau_s} V_{IF}^{(m)} \quad (3.2)$$

This can be solved using the z-transform to get

$$V_{IF}(z) = \frac{t_{on}/\tau_f}{1 - z^{-1}(1 - \frac{\Delta t}{\tau_s} - \frac{t_{on}}{\tau_f})} V'_s(z) \quad (3.3)$$

which has an impulse-invariant equivalent analog transfer function [3.8]

$$V_{IF}(f_{IF}) = \frac{\frac{t_{on}}{\tau_f \Delta t}}{j2\pi f_{IF} + \frac{1}{\tau_s} + \frac{t_{on}}{\tau_f \Delta t}} V'_s(f_{IF}) \quad (3.4)$$

The *voltage* conversion efficiency is therefore given by,

$$(CE)_v = \frac{\frac{t_{on}}{\tau_f \Delta t}}{\sqrt{(2\pi f_{IF})^2 + (\frac{1}{\tau_s} + \frac{t_{on}}{\tau_f \Delta t})^2}} \quad (3.5)$$

The *power* conversion efficiency is just the square of the voltage conversion efficiency multiplied by the ratio of the actual rf source and IF load impedances

$$(CE)_p = (CE)_v^2 \frac{2R_s}{R_L} \quad (3.6)$$

It can readily be shown that the power conversion efficiency is maximized for  $R_L = (R_s + R_d/2 + R_j/2)/D$ , where  $D = t_{on}/\Delta t$  is the duty cycle, yielding an optimum conversion efficiency of

$$(CE)_p = \frac{1}{2} \frac{DR_s}{R_s + R_d/2 + R_j/2} \quad (3.7)$$

as if the sampler were replaced by a resistor  $R_{IF}$  as shown in Fig. 3.5a. The value of the equivalent sampler resistance at the IF frequency is given by

$$R_{IF} = \frac{(R_s + R_d/2 + R_j/2)}{D} \quad (3.8)$$

which is simply the resistance connected to the ideal switch divided by the duty cycle. That  $(CE)_p$  varies *linearly* with the duty cycle, is one of the primary advantages, in some applications, of the sampler over the harmonic mixer, which has a power conversion efficiency that varies with the square of duty cycle. This simple model also gives the correct value of the IF bandwidth,

$$f_{IF(3-dB)} = \frac{1}{2\pi(R_{IF} \parallel R_L)C_H} \quad (3.9)$$

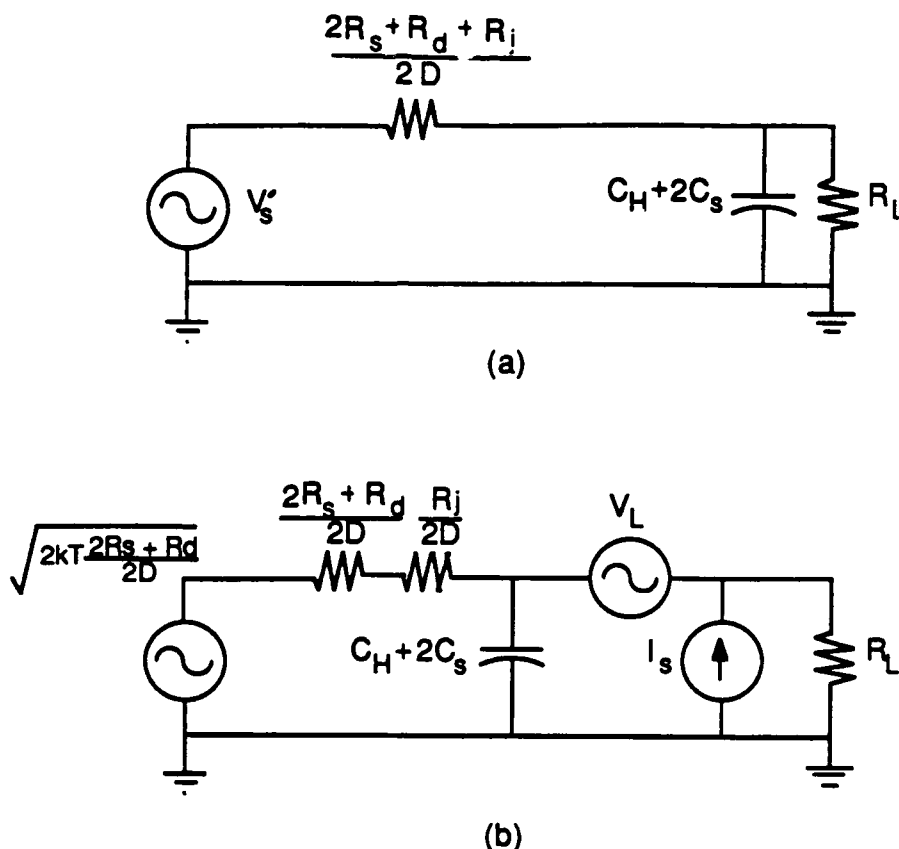


Figure 3.5: Intermediate frequency equivalent circuit (a) and noise model (b).

The thermal noise voltage of the physical resistances scales in the same manner as the resistor value, as shown in Fig. 3.5b. From this model, the input-referred mean-square voltage noise spectral density is determined to be

$$v_n^2 = \frac{2k_B T}{D} (R_s + R_d/2) + v_L^2 + (I_s R_L)^2 \quad (3.10)$$

where  $k_B$  is the Boltzmann constant and  $T$  is absolute temperature. Here,  $v_L$  is the input noise voltage of the IF load, which may not be a physical resistor, and  $I_s$  is the diode shot noise current. Using this model, it can readily be determined that the noise figure of the sampler is approximately equal to its power conversion loss if shot noise is neglected.

### 3.2.3 Input frequency limitations

In §3.2.2, the IF response was not a function of the input frequency so long as  $\Delta t$  could be chosen to give the desired  $f_{IF}$ . However, the input frequency – also called radio frequency input (rf) – is restricted by several major factors. The lower limit will be set by the longest  $\Delta t$  that can be attained. The upper limit is a function of  $t_{on}$  and sampling device parasitics. If  $t_{on}$  is not much less than an input signal period,  $V_s$  can not be replaced by a piecewise constant source as in §3.2.2. In this case, the time dependant conductance of the switch must be multiplied by the input signal to obtain the capacitor charging current. At each sample, the switch conductance will be multiplying a slightly different portion of the input waveform so that the integrated current on the capacitor is proportional to the *convolution* of the switch conductance and the input signal voltage. The switch conductance waveform can therefore be considered the impulse response of the system. For a square shaped aperture the transfer function is  $\sin(\pi f t_{on})/\pi f t_{on}$  so the 3-dB bandwidth is,  $f_{rf(3-dB)}^{(1)} = 0.44/t_{on}$ . However, the widely used rule of thumb,  $f_{rf(3-dB)}^{(1)} = 0.35/t_{on}$  [3.6] provides a more conservative estimate.

While IF response can be discussed in general terms, the rf bandwidth is dependant on the particular implementation. The samplers discussed here are all of the two diode variety briefly outlined in §3.2.1. When a diode replaces the ideal switch, as in Fig. 3.6, capacitance and series resistance prevent in two ways the sampler from attaining the bandwidth made possible by the strobe pulse. First, the capacitive loading of the shunt diodes on the rf line causes rf voltage at the diodes to have a pole in its frequency response at  $f_{rf(3-dB)}^{(2)} = 1/(4\pi C_{j0}(R_s + R_d/2))$ , where  $C_{j0}$  is the zero-bias junction capacitance. Secondly, the diode capacitance broadens the strobe pulsewidth applied to the diodes by introducing a pole in the LO transfer function at  $f_{LO(3-dB)} = 1/\pi R_{se} C_{j0}$ . From Fig. 3.6, the equivalent resistance in series with the diodes is  $R_{se} = 2R_d + (R_s^{LO} Z_e)/(R_s^{LO} + Z_e)$ , where  $Z_e$  is the impedance of the even mode on the rf transmission line, and  $R_s^{LO}$  is the LO source impedance.

To determine the rf bandwidth due to all the factors discussed above, it is first necessary to determine the effect of the pole in the LO transfer function on the rf transfer function. This is handled in a quasi-empirical manner by assuming that  $t_{on}$

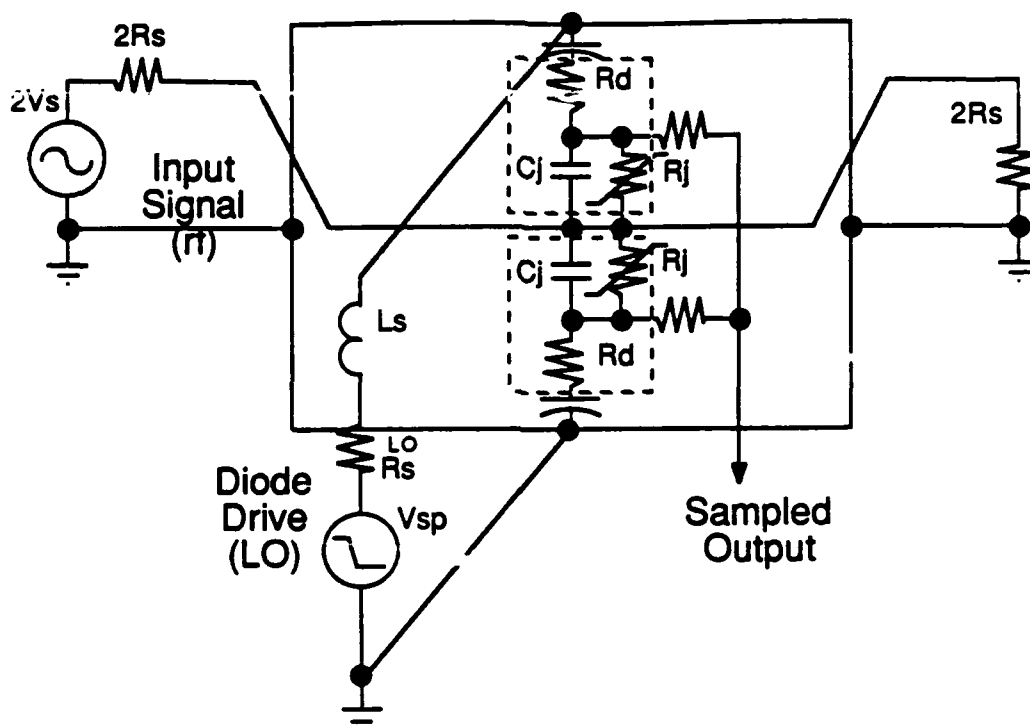


Figure 3.6: Sampler equivalent circuit including diode parasitics.

is one half the actual voltage pulse width. That this could be the case is illustrated in Fig. 3.7. Obviously, by adjusting the diode bias,  $t_{on}$  may be varied without changing the voltage pulse. However, in a typical system, the range of adjustment is limited since too little reverse bias will result in unwanted diode switching due to LO pulse ringing, and too much reverse bias will degrade the conversion efficiency of the sampler. So, under typical conditions, if the LO input pulse is known, the broadened pulse can be computed from the LO transfer function. One half of the broadened pulse width is then taken as  $t_{on}$ . Now, by using the root-sum-squared (RSS) technique [3.9], the various factors can be combined to produce an estimate of the rf bandwidth:

$$f_{rf(3-dB)} = \frac{1}{2\pi\sqrt{(2C_{j0}(R_s + R_d))^2 + (R_{se}C_{j0}/4)^2 + (PW/2)^2}} \quad (3.11)$$

Here, PW is the sampling voltage pulse width in the absence of parasitics, which is approximately equal to the fall time of the strobe signal generator.

Inductive parasitics in the fully monolithic samplers discussed later are on the order of a few picohenrys. While this is not totally negligible, it is small enough to

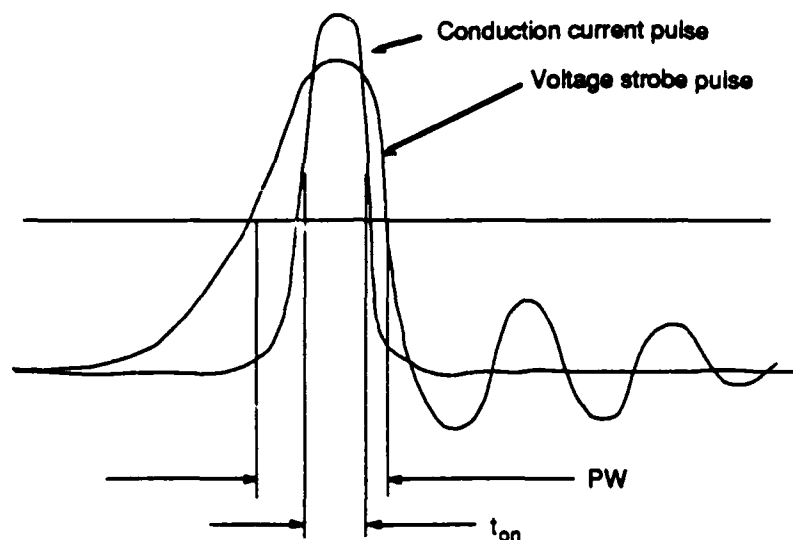


Figure 3.7: Relationship between sampling aperture, defined by the conduction current pulse, and voltage strobe pulse width. The aperture,  $t_{on}$  is typically one half of the strobe pulse width,  $PW$ .

ignore for this simple analysis. In samplers which require hybrid assembly, inductive parasitics can be one of the primary design constraints. Even the modern beam-leaded diode can have parasitic inductance greater than  $\sim 100pH$  [3.10]. Grove [3.6] presents an analysis which includes inductive effects and provides the following design equations:

$$f_n = \frac{1}{2\pi\sqrt{LC}}, \quad \delta = \frac{R_d/2 + R_s}{2} \sqrt{\frac{C}{L}} \quad (3.12)$$

where  $f_n$  is the rf cutoff frequency,  $L$  is the diode package inductance divided by two,  $C$  is two times the diode junction capacitance, and  $\delta$  is the damping factor. These equations must be used when designing a monolithic sampler to be certain that inductance is not becoming a significant factor. Also, in a monolithic sampler, inductance may be added to reduce the damping factor and increase the bandwidth.

The analysis of the preceding sections presented the following elements which must be considered for maximum rf bandwidth:

- Sampling diode capacitance and series resistance
- Inductive and other parasitics associated with layout and interconnections
- Falltime of the strobe signal generator.

The nonlinear transmission line described in §1.2.2 provides a ten times improvement in slew rate over the step recovery diode while maintaining similar amplitude. Because the NLTL is implemented in monolithic GaAs IC technology, it can be integrated with the sampling head to drastically reduce the inductance normally associated with the connection between the sampler and the strobe signal generator. Thus, the NLTL in conjunction with a low-parasitic monolithic sampler provides the possibility of dramatic improvements in rf bandwidth. Several designs of such a sampling system are presented in the following sections.

### 3.3 Monolithic samplers

#### 3.3.1 Generation I

##### Design and layout

The objective of the first monolithic sampler design was to demonstrate the superior performance afforded by the NLTL, with minimum risk. To accomplish this objective, the sampler was designed around a proven NLTL design [3.11]. Choosing the same epitaxial layer doping and thickness allowed use of measured diode and resistor properties which are highly reproducible using molecular beam epitaxy (MBE). The two diode sampling bridge was selected because of its simplicity. The problem with this structure is that, even in more modern implementations [3.12,13], it is highly three dimensional and requires hybrid assembly. By using coplanar waveguide for the transmission lines, it can be collapsed into one plane, so that it can be monolithically integrated with a NLTL strobe signal generator [3.14].

The design of Fig. 3.8 reduces the structure to one plane by using the even and odd modes of CPW [3.15], allowing monolithic integration of the entire sampling

head. The design is similar to that reported by Hunton [3.16] for a 4 GHz double balanced mixer. The major improvement of this design is that it minimizes the use of slotline which is lossy and dispersive. In addition, monolithic integration and the use of a NLTL strobe pulse generator provide a much greater bandwidth. The RF signal to be sampled is applied to the port labeled "External signal input" and travels in the normal (odd) mode on the vertical CPW. NLTLs drive the ports labeled "Strobe pulse input", and "Internal test signal input". Only the final sections of the on-chip NLTLs are shown in the figure. The NLTL design is identical to that reported in [3.11]. The sawtooth wave applied to the "Strobe pulse input" of Fig. 3.8 travels in the odd mode on the horizontal CPW until it is applied to the sampling diodes and the slotline (even) mode of the RF CPW. The even mode is shorted by airbridge connections 180  $\mu\text{m}$  from the sampling diodes. The reflected wave turns the diodes off after a round trip time of  $\sim 4$  ps. An additional NLTL is located below the sampling head to provide a high speed test signal to evaluate the sampler risetime. Beyond the diodes, the ground planes were taken back to a 130  $\mu\text{m}$  spacing to increase the impedance of the even CPW mode, while maintaining 50 $\Omega$  for the odd mode.

The central portion of the sampler has a CPW ground-to-ground spacing just large enough to accommodate the two sampling diodes. In this first design, Schottky metal was the same as the (thick) interconnect metal, so, using the design rules of Chapter 2, the minimum spacing was 3  $\mu\text{m}$ . In the layout of Fig. 3.9 the two diodes required 45  $\mu\text{m}$ . This is the distance the center conductor of the strobe line must protrude to make connection to the opposite ground plane. The inductance of this protrusion can be estimated to be 28 pH from

$$L = 2 \times 10^{-4} l \left[ \ln\left(\frac{l}{w+t}\right) + 1.19 + 0.22 \frac{w+t}{l} \right] \quad (3.13)$$

where  $L$  is in nH,  $l = 45$ ,  $t = 1.4$ , and  $w = 5$  are the length, thickness, and width of the strip in microns [3.17]. It would be preferable to choose the diode junction capacitance such that when two are driven in series,  $R_{se}C \geq L/R_{se}$ , where  $R_{se}$  is given in §3.2.3 and  $C$  is half the diode junction capacitance. In this case the design would not depend critically on the exact value of  $L$ .

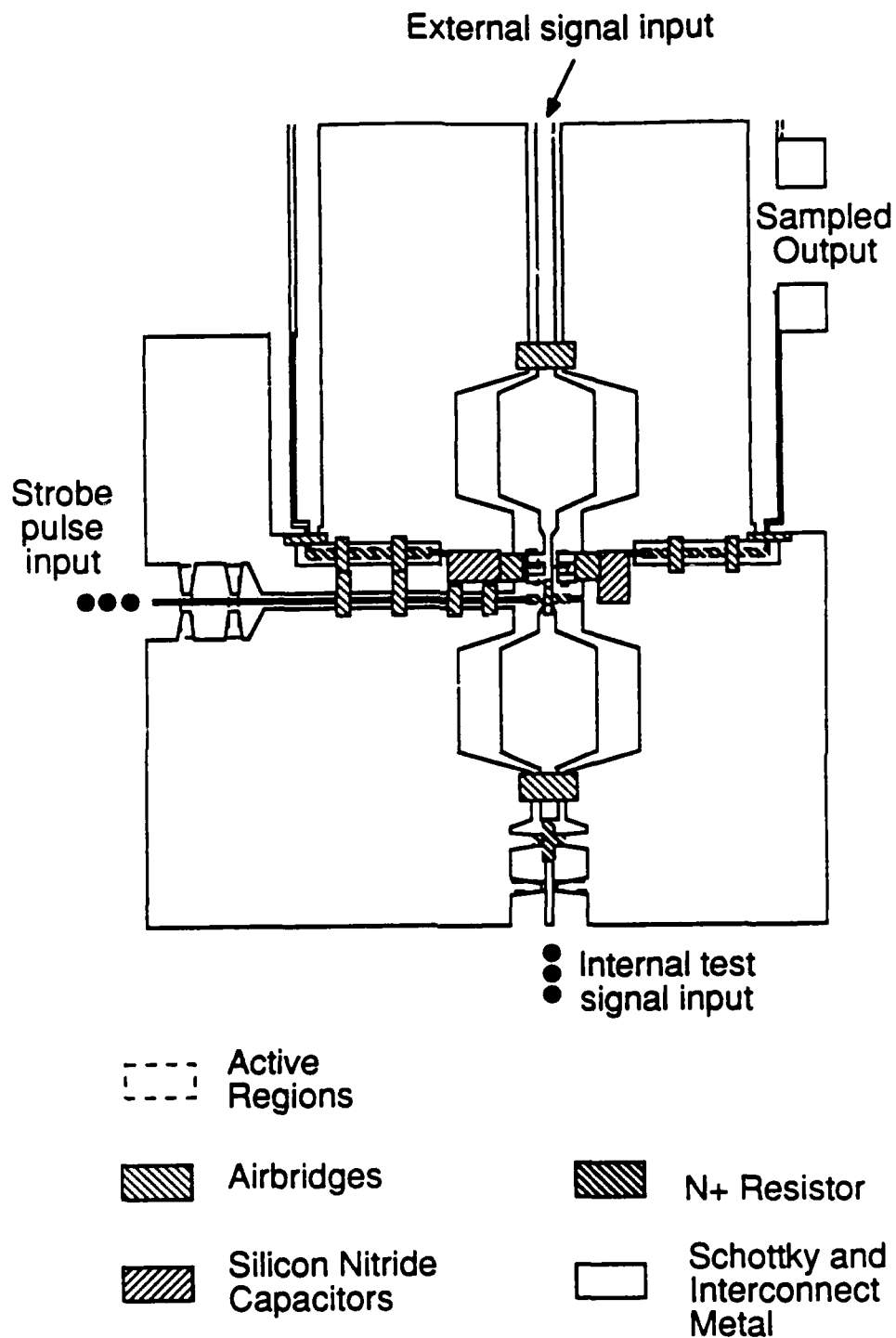


Figure 3.8: Layout of Generation I sampler showing the sampler and portions of two nonlinear transmission lines.

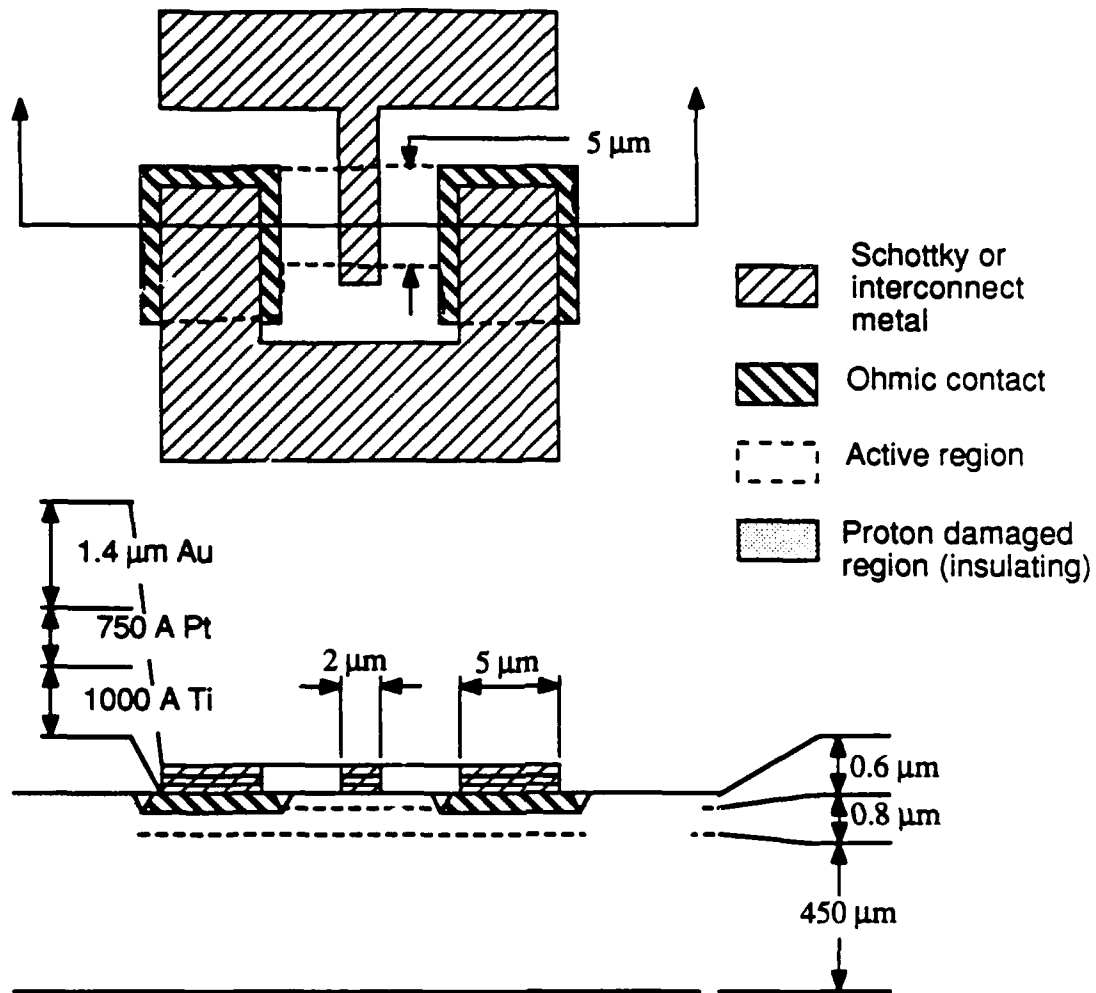


Figure 3.9: Diode layout for the Generation I sampler. The Schottky contact extends beyond the active region so that alignment error does not change area of the diode.

The actual value of the diode junction capacitance was chosen so that the diode conduction current was larger than the displacement current of the junction capacitance. This is desirable because the sampling diodes are also varactors. That is, there will be mixing due to both nonlinear resistance and capacitance. Since the nonlinear capacitor current is maximum where the slope of the diode strobe pulse is maximum, the capacitive sampling function is more broad than the resistive and has a double peak. Since the relative contributions of the two nonlinear processes are related to the respective currents, the ratio of the diode conduction current to the peak junction capacitor current should be maximized. For a diode forward conduction

current of 5 mA and a strobe pulse slew rate of  $7.1 \times 10^{11}$  V/s, the diode capacitance should be less than 7 fF. The value chosen was 6 fF, which is a  $2 \times 5 \mu\text{m}$  diode on the  $3 \times 10^{16}$  doped  $N^-$  layer. Diodes smaller than this were judged impractical because of excessive  $N^-$  resistance.

Assuming 2 fF of stray capacitance in addition to the 6 fF junction capacitance and a diode series resistance of  $60\Omega$ , the damping factor of the sampling loop, which includes the two sampling diodes in series and the inductance of the connection, is 0.9. With this damping factor, the bandwidth predicted with the simple RC model of §3.2.3 is pessimistic by a factor of 2. Using the RC model in this case gives substantial room for error in the calculated sampling-loop bandwidth of 250 GHz.

The NLTL used as a strobe pulse generator (also called the local oscillator or LO) produces a 2.5 V, 3.5 ps falltime sawtooth wave when driven with an 8 GHz, 23 dBm sine wave. Since the slope of the rising edge is negligible in comparison with that of the falling edge, the derivative of the waveform is a 3.5 ps impulse, full-width at half-maximum (FWHM). Used as a strobe pulse generator, this can give  $\sim 1.8$  ps sampling bridge aperture times if the diode bias is set at  $\sim 50\%$  of the impulse magnitude.

When the strobe is applied to the CPW even mode and the sampling diodes, voltage will be divided across the strobe source impedance and the CPW even mode impedance. To achieve maximum voltage across the sampling diodes, the even mode impedance should be maximized. Using scale models on Stycast<sup>1</sup> material, it was determined that the largest even mode CPW impedance that could be obtained without introducing excessive parasitics to the odd mode was  $75\Omega$ . Driving the even mode from the center of the transmission line reduces the impedance by two. So, in this design,  $Z_e = 75\Omega/2$ ,  $Z_s = 90\Omega$ ,  $r_s = 60\Omega$ , and  $C_{j0} = 8\text{fF}$ , giving the sampling loop a time constant of 0.6 ps. Using root-sum-squares (RSS) convolution, the predicted strobe pulse width is,  $\sqrt{3.5^2 + 0.6^2} = 3.6$  ps, giving an aperture time of 1.8 ps. The pole in the RF circuit will contribute 1.9 ps to the system risetime, so the total system will have a risetime of  $\sqrt{1.8^2 + 1.9^2} = 2.6$  ps and a corresponding 3 dB bandwidth of 130 GHz.

<sup>1</sup>Stycast is a trademark of Emerson & Cuming

The relative contributions of the various parasitics to the system time constant discussed above are summarized in Fig. 3.10. The 3.5 ps strobe fall time and the 0.6 ps time constant of the sampling loop are divided by two since the resulting sampling aperture is approximately one half of the parasitic-broadened strobe pulse (see Fig. 3.7). Note that strobe parasitics are negligible in comparison with the diode loading on the rf line (rf pole).

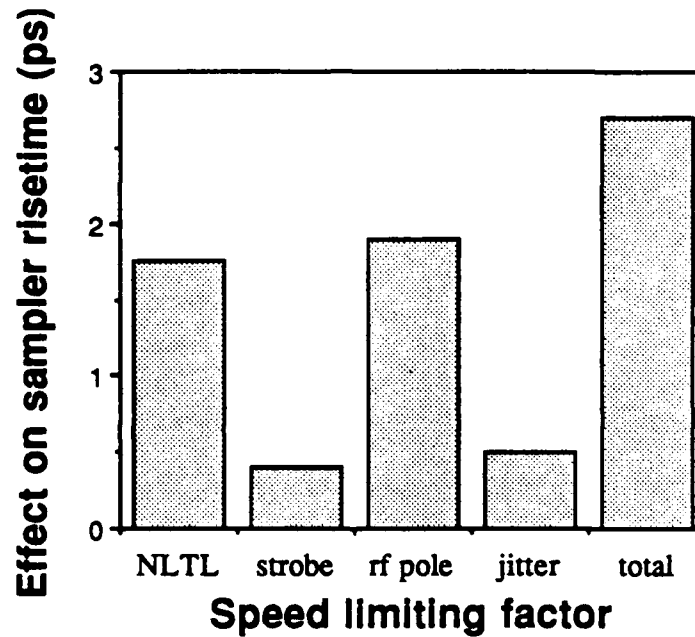


Figure 3.10: Risetime limiting factors of the Generation I sampler. Column 1 is the NLTL output falltime divided by two, which is the diode aperture time in the absence of parasitics. Column 2 represents the contribution the sampling diodes loading the strobe circuit while Column 3 shows their effect on the rf circuit. Timing jitter is depicted in Column 4 and the RSS total is shown in Column 5.

### Results

The sampler bandwidth was evaluated by probing internal nodes of the circuit using direct electrooptic sampling and by using the sampling circuit to measure the output of both the NLTL internal test signal generator and an external 80–128 GHz

frequency multiplier. A strobe pulse width of 4.0 ps was measured using direct electrooptic sampling (Fig. 3.11). From RSS deconvolution of the 1.9 ps electrooptic

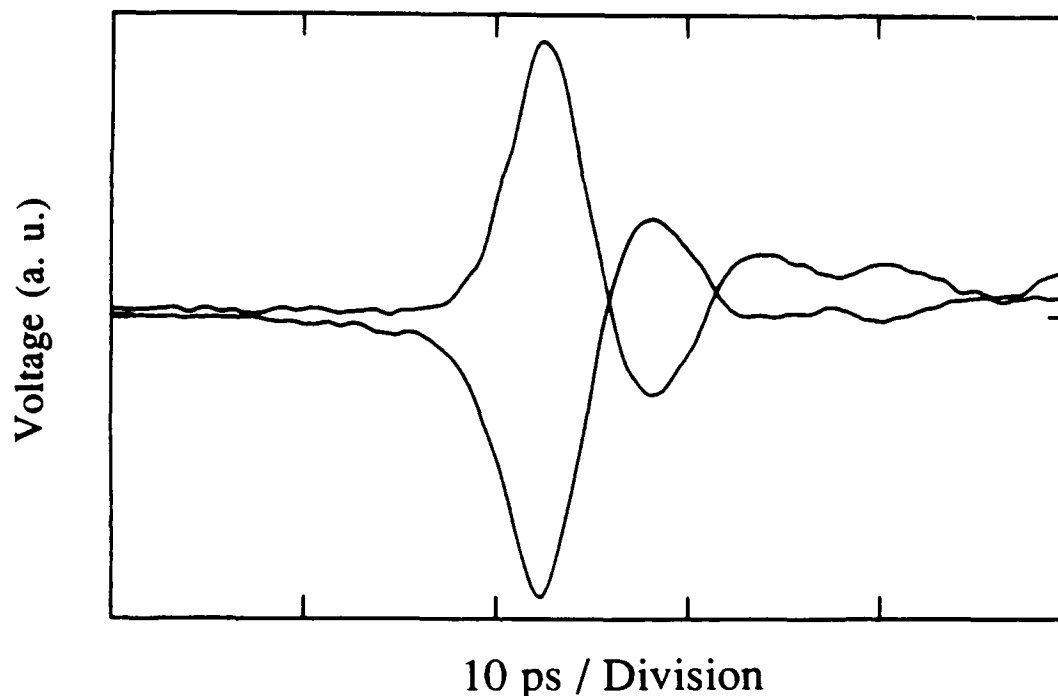


Figure 3.11: Electrooptically sampled Generation I sampler strobe pulses. The positive going waveform is the voltage strobe pulse appearing at the anode of  $D_2$ ; the negative going pulse is at the cathode of  $D_1$ .

measurement system impulse response, the strobe pulse width is  $\sim 3.5$  ps FWHM. Depending on the diode bias, the corresponding diode sampler aperture time is between 1.8 and 3.5 ps.

The test signal generator, identical to the LO strobe pulse generator, is a NLTL whose output is attenuated 50:1. Measured by electrooptic sampling, the test signal has a falltime of approximately 3.5 ps. The test signal 10%–90% falltime measured by the diode sampling head was 4.0 ps (Fig. 3.12). Using RSS deconvolution, the sampling circuit is found to have a 2.7 ps 10%–90% risetime, with a corresponding

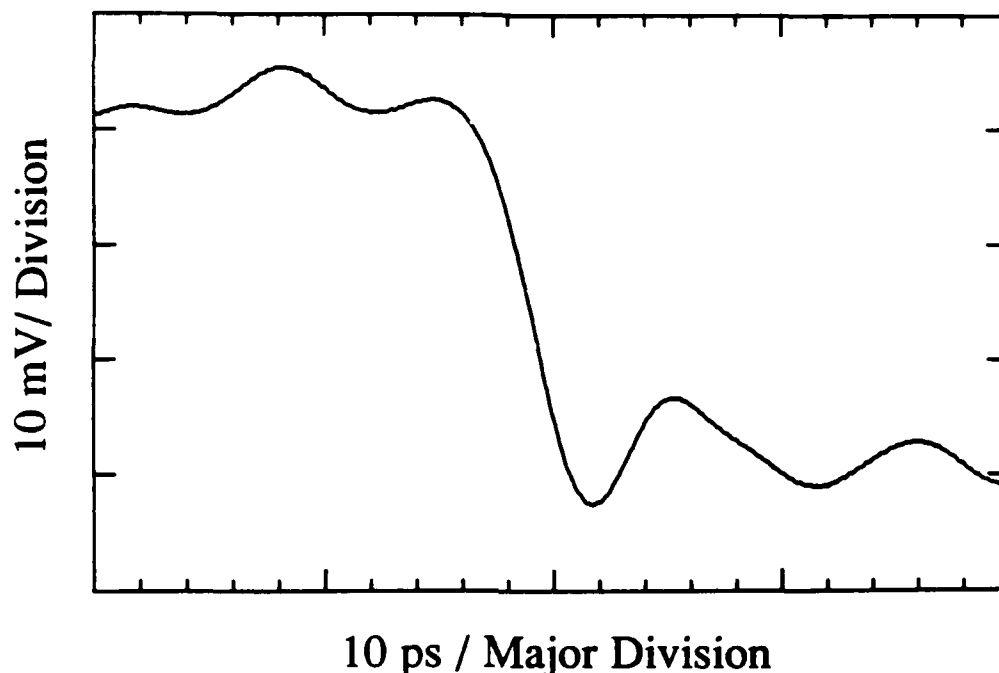


Figure 3.12: Sampled output of a 50:1 attenuated nonlinear transmission line. The measured falltime is 4.0 ps; the actual falltime is estimated to be 3.5 ps.

bandwidth of roughly 130 GHz.

To get a better measure of the speed of this sampler, a 5 times frequency multiplier probe, which has measurable power from 80 to 128 GHz [3.18], was used. With the multiplier probe providing the input test signal, the node being electrically sampled was simultaneously probed by the electrooptic sampler (see Fig. 3.13). The power computed from the voltage measured by the sampling head was divided by that measured with the optical probe. The result is shown in Fig. 3.14, where 0 dB corresponds to the video response at 82 MHz. The graph shows that the response is relatively flat up to 128 GHz. If the phase were linear up to this frequency, the time resolution of this all electrical sampler would be better than 2.7 ps. However, as this measurement is normalized to the node being sampled, it does not include

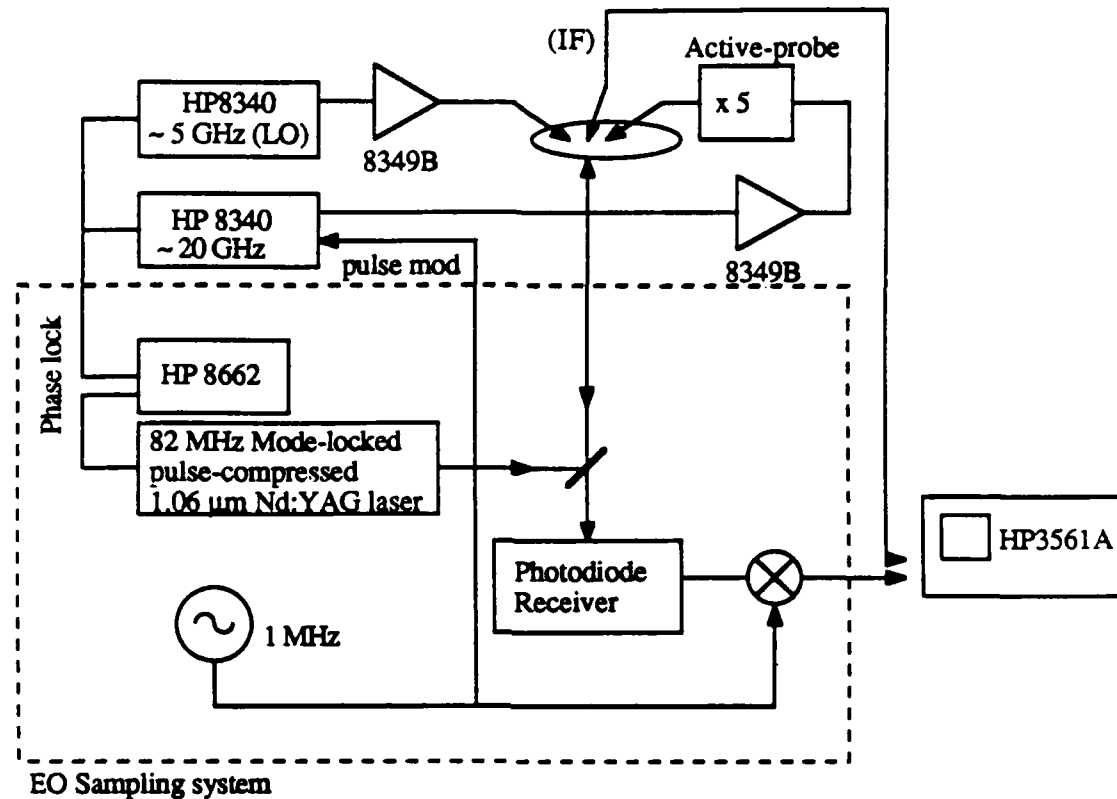


Figure 3.13: Experimental set-up for measuring sampler response.

the effect of the rf pole.

Depending on the LO drive power, the 1 dB compression point was as high as 10 dBm. The equivalent input noise voltage was  $90 \text{ nV}/\sqrt{\text{Hz}}$ . At 5 GHz, RF to IF isolation was 55 dB, LO to IF isolation 63 dB, and the LO to RF isolation was 68 dB [3.19].

### 3.3.2 Generation II

#### Design and layout

The motivation behind development of the second generation sampler was to produce more samplers that could be used in various applications, not necessarily to improve the design. However, to increase the number of samplers that could fit on

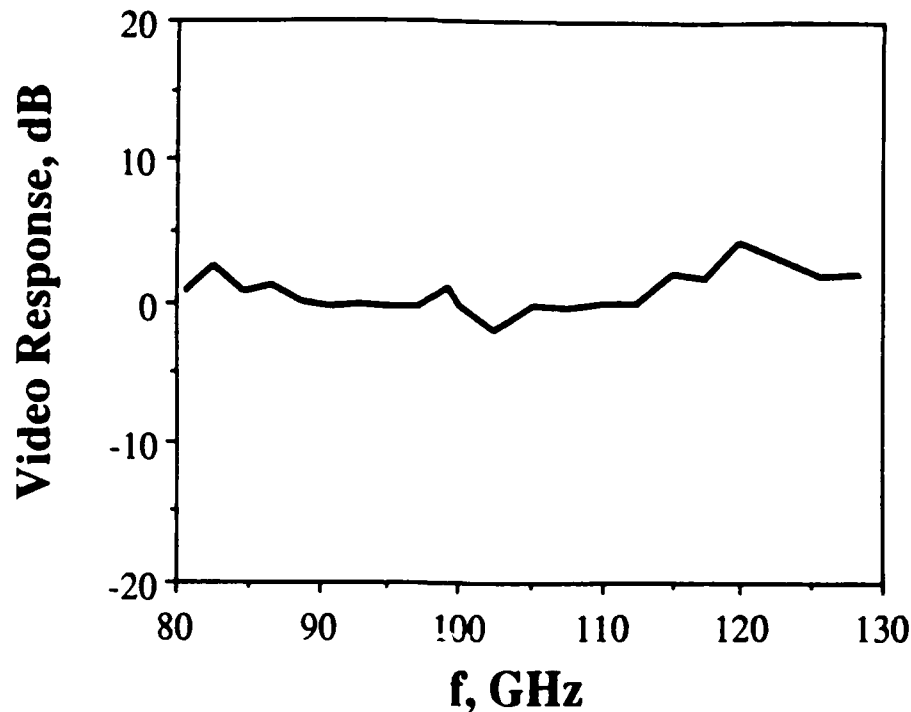


Figure 3.14: Sampler video response from 80 to 128 GHz. To obtain the video response, the sampler measured power was divided by that measured by EO sampling at the node being electrically sampled.

the wafer, it was necessary to design a more compact NLTL. This is readily accomplished by using coplanar-strip (CPS) for the interconnecting transmission lines rather than coplanar-waveguide (CPW) with its large ground planes. Unfortunately, CPS is a balanced transmission line and therefore a new sampler had to be designed which could be driven from a balanced line. Still, no changes were made to the epitaxial layer structure.

The CPS nonlinear transmission line is shown in Fig. 3.15. It is nearly electrically equivalent to the CPW NLTL used in the previous design. The major difference is that a  $90\Omega$  CPS can have a smaller transverse dimension and lower ohmic losses. Also, the varactor diodes must be rotated  $90^\circ$ . This creates some difficulty since now the length of the ohmic is parallel to the transmission line rather than the width. It is usually desirable to make the ohmic at least  $20\ \mu\text{m}$  long to minimize its resistance per unit width. If the varactor ohmics were made  $20\ \mu\text{m}$  long, the total length of the discontinuity presented to the transmission line would be greater

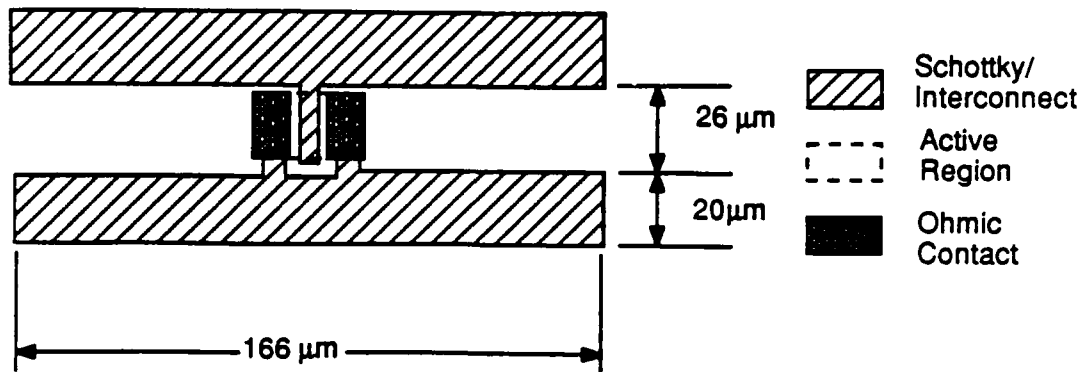


Figure 3.15: Coplanar strip (CPS) nonlinear transmission line.

than  $45 \mu\text{m}$  (two ohmics and a  $5 \mu\text{m}$  Schottky contact) which is over twice that in the CPW design. For this reason, the ohmics were made only  $10 \mu\text{m}$  long and the consequent increase in varactor series resistance was suffered.

The sampler designed for the CPS NLTL is shown in Fig. 3.16. It is considerably simpler than the previous design since the strobe is already balanced. It is only necessary to apply the strobe to the sampling diodes in a fashion that provides a low inductance connection and isolation from the rf port. This sampler is not a feed-through sampler as in the previous design so it is not possible to provide self-test capability by adding a second NLTL. This reduces the die area substantially but makes testing much more difficult.

### Results

Because of the lack of an internal test signal generator in this design, it is necessary to bring in an external test signal and use electrooptic sampling to determine the actual voltage. This is also made difficult by the CPS geometry since the small ground plane area on wafer does not suppress signals that may be on the ground plane of the test signal probe. This is in fact the case with the frequency

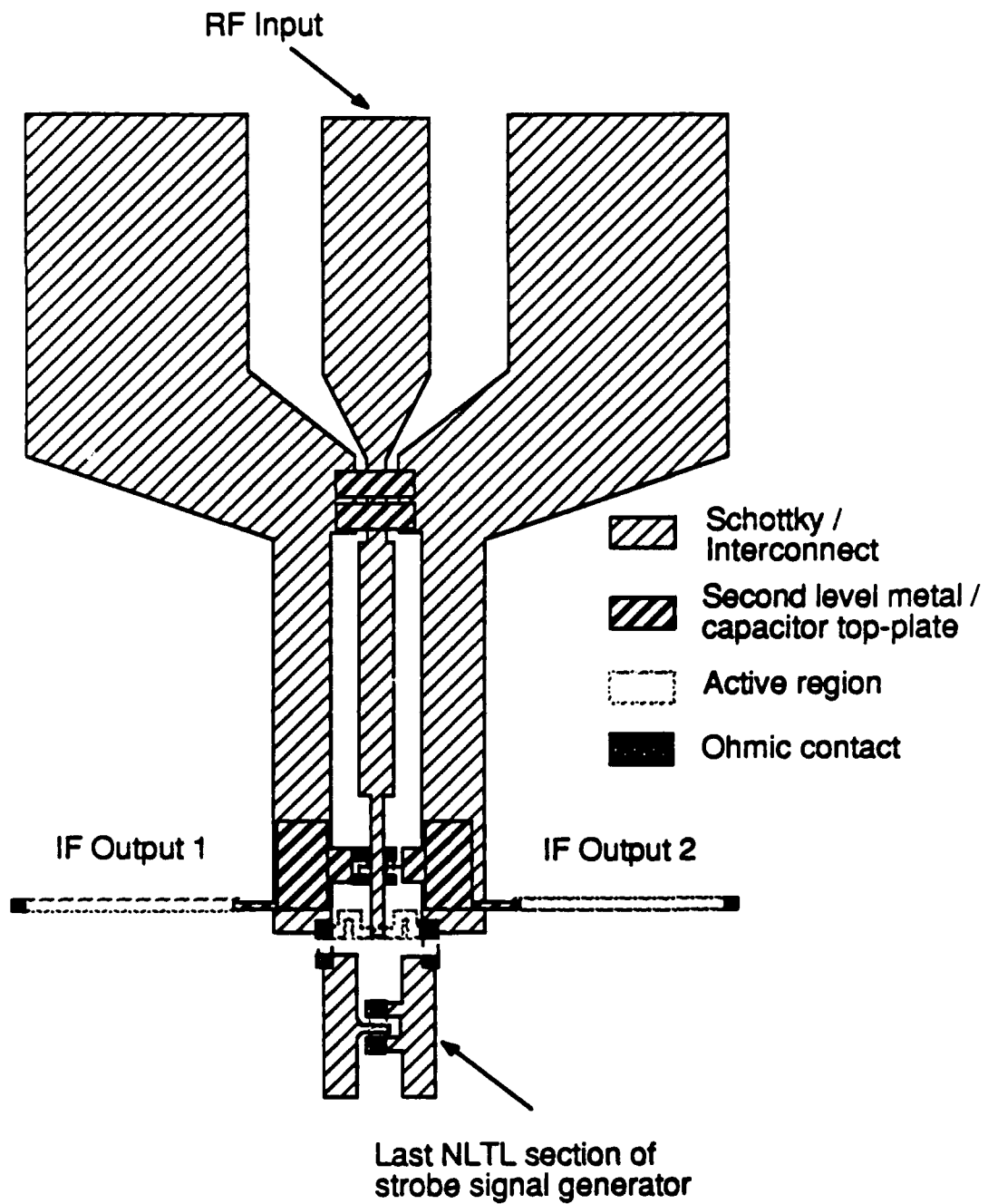


Figure 3.16: Sampler designed for the CPS NLTL.

multiplier probe used to test the previous design. This is a problem since the sampler only measures the voltage between the center conductor and ground while the EO sampler measures absolute voltage. Therefore, it is necessary to EO sample the voltage on the center conductor and subtract the the EO sampled voltage on the ground to obtain a value that can be compared with the electrically sampled result. Because these two voltages are similar in magnitude, the error involved in this measurement can be very large. Although an absolute reference could not be established, the power measured with this sampler at 100 GHz compared favorably with that measured with the previous design.

Given the problems mentioned above, on-wafer tests were abandoned and instead the performance of a packaged sampler was evaluated. This was simplified by the 'in-line' design which made the CPS sampler chip nearly a 'drop-in' replacement for the sampler used in the 40 GHz Wiltron 360 [3.20] vector network analyzer. A hybrid power splitter/balun was designed by Jay Banwait of Wiltron Company to allow two CPS NLTLs to be driven from the same coaxial connector. The two sampler dies were mounted with the power splitter and two CPW tapers for the rf ports in the Wiltron sampler package. The completed package could then be plugged directly into the IF buffer amplifier used in the Wiltron 360 network analyzer. The experimental test set-up is shown in Fig. 3.17. The conversion loss of this sampler when driven with a 500 MHz local oscillator strobe signal from a step recovery diode is shown in Fig. 3.18. The displayed conversion loss includes the 6 dB conversion loss of the second-IF mixer, the 32 dB attenuation of the first-IF monitor port, and the 39 dB gain of the buffer amplifier. The conversion loss is high because the Wiltron buffer amplifier has an input impedance of approximately  $12k\Omega$  while the sampler has an IF output impedance of  $\frac{2n_s}{1.8ps}(25 + 30) = 64k\Omega$ . This gives a 16dB loss due to the voltage divider, 10 dB higher than the matched condition. The conversion loss for a matched IF is 37 dB according to Eq. (3.7). The rf test signal was provided by a Hewlett-Packard (HP) 8340A synthesizer with a frequency doubler and tripler to reach 60 GHz. The sampler measured power was normalized to that measured with a frequency-extended HP 8566B spectrum analyzer.

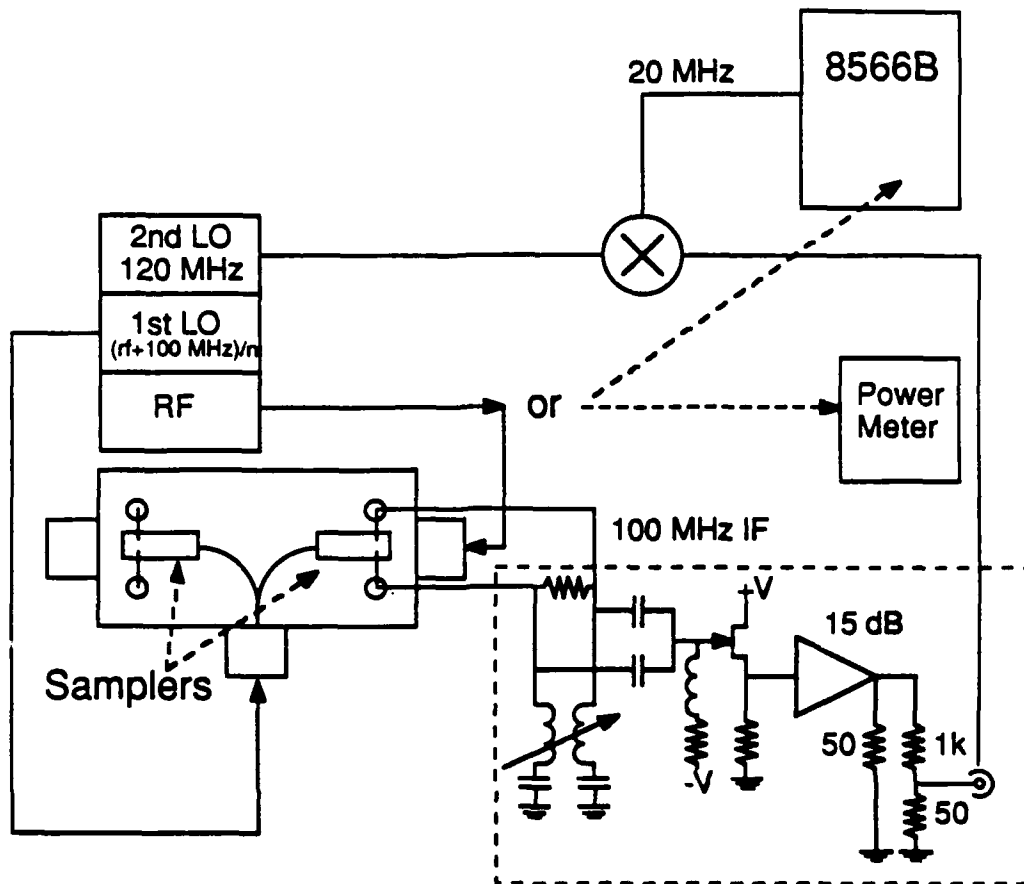


Figure 3.17: Experimental set-up for conversion loss measurement of the packaged Generation II sampler.

### 3.3.3 Generation III

#### Design and layout

The goal of the third generation sampler was to achieve the greatest bandwidth possible. Improvements were made to the NLTL, the sampling diodes, and layout. To avoid conflict between the changes to the NLTL and sampler, most of the NLTL was placed on a separate chip. This chip used a hyperabrupt doping profile as described previously [3.21] to achieve a 6 V, 1.6 ps transition. A small NLTL was placed on chip with the sampler since the output of the NLTL chip was limited to about 5 ps by the interconnecting bond wires. The sampling diode series resistance

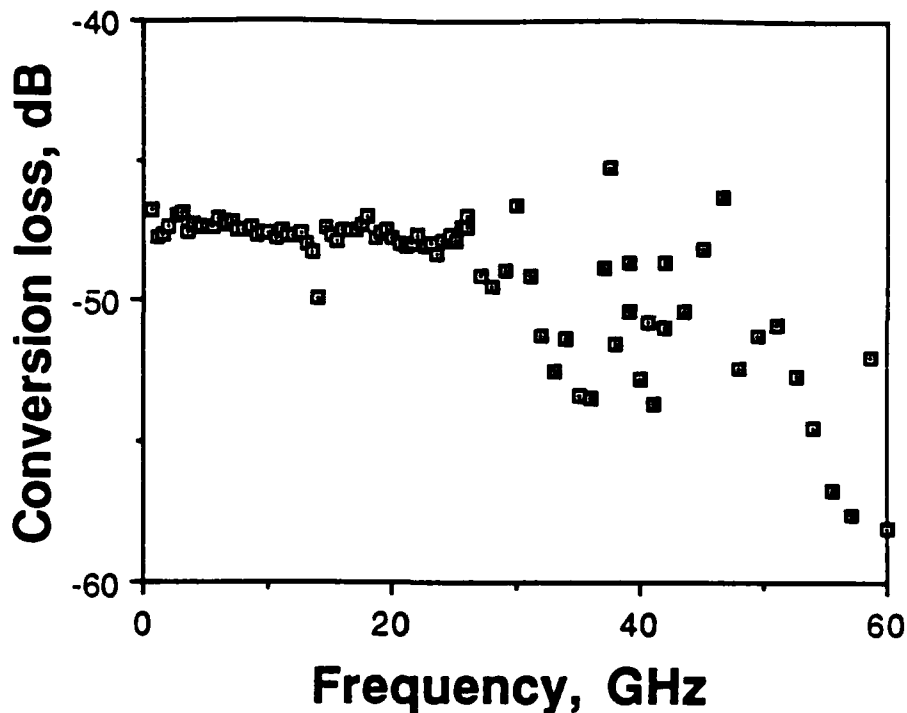


Figure 3.18: Conversion loss of the packaged CPS sampler with a 500 MHz LO using the Wiltron IF buffer amplifier.

was reduced to  $12.5\Omega$  by using an  $N^-$  layer half as thick,  $0.3\ \mu\text{m}$ , with 4 times the doping,  $1.2 \times 10^{17}/\text{cm}^3$  while maintaining the zero bias junction capacitance,  $C_{j0}$  near  $9.5\ \text{fF}$ . The cut off frequency of the on-chip NLTL diodes was also improved by widening the ohmic contacts and bringing the ohmic metal closer to the Schottky contact to reduce series resistance. A scanning electron micrograph (SEM) of a completed NLTL diode is shown in Fig. 3.19.

Layout is perhaps the most important consideration in designing a high-speed sampler. In this design, the NLTL drives the two ground planes of the rf CPW (Fig. 3.20). To minimize the inductance of this connection, the ground planes must be close together. However, the sampling diodes must be placed between these ground planes to reduce the inductance of their connection. These conflicting goals are met by imbedding the sampling diodes into the ground planes so that only the portion of the diode which is not at zero rf potential protrudes. This reduces the length of the sampling diode connection to  $8\ \mu\text{m}$ . To improve yield and provide a better input match, airbridge crossovers were avoided in the rf center conductor and diode

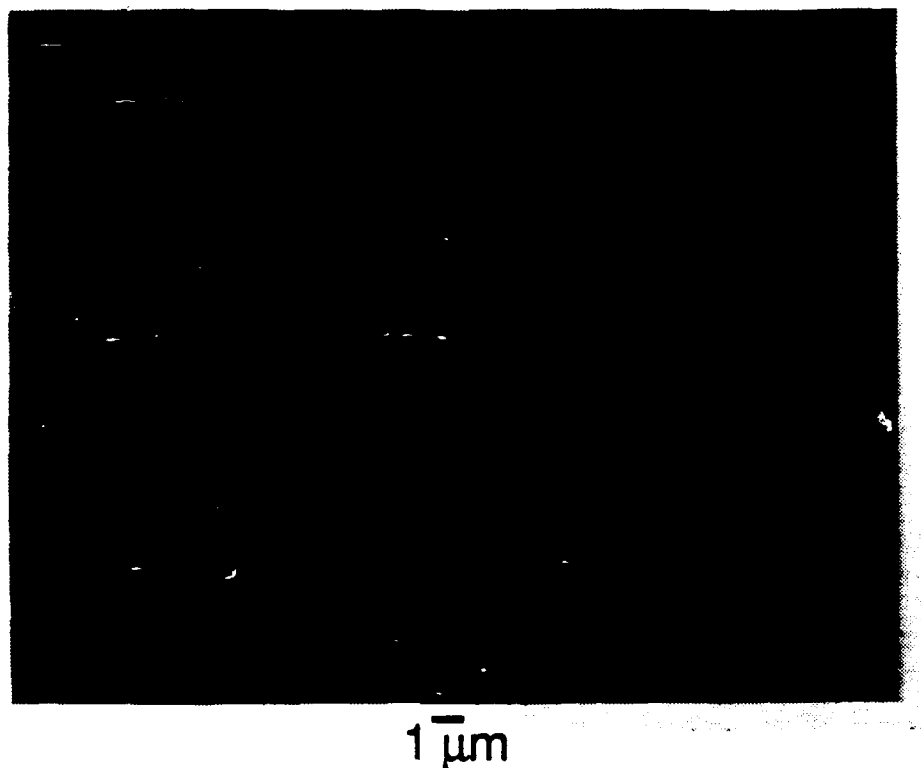


Figure 3.19: Scanning electron micrograph of an on-chip NLTL diode. Ohmic metal is brought within  $1 \mu\text{m}$  of the Schottky contact.

connection and instead were used in the ground plane where many could be placed in parallel (Fig. 3.21).

### Results

The speed of the sampler was evaluated by using the on-board NLTL test signal generator and by direct electrooptic sampling. With the test NLTL driven at  $10 \text{ GHz} + 100 \text{ Hz}$  and the strobe NLTL driven at  $5 \text{ GHz}$ , the sampled output showed a  $160 \mu\text{s}$  90% to 10% fall-time, which corresponds to  $1.6 \text{ ps}$  in real-time (Fig. 3.22). This is the fastest transition ever measured by an all electronic device. The strobe pulses driving the sampling diodes had an estimated width of  $1.7 \text{ ps}$  after deconvolving the impulse response of the electrooptic sampler (Fig. 3.23). The diodes were only

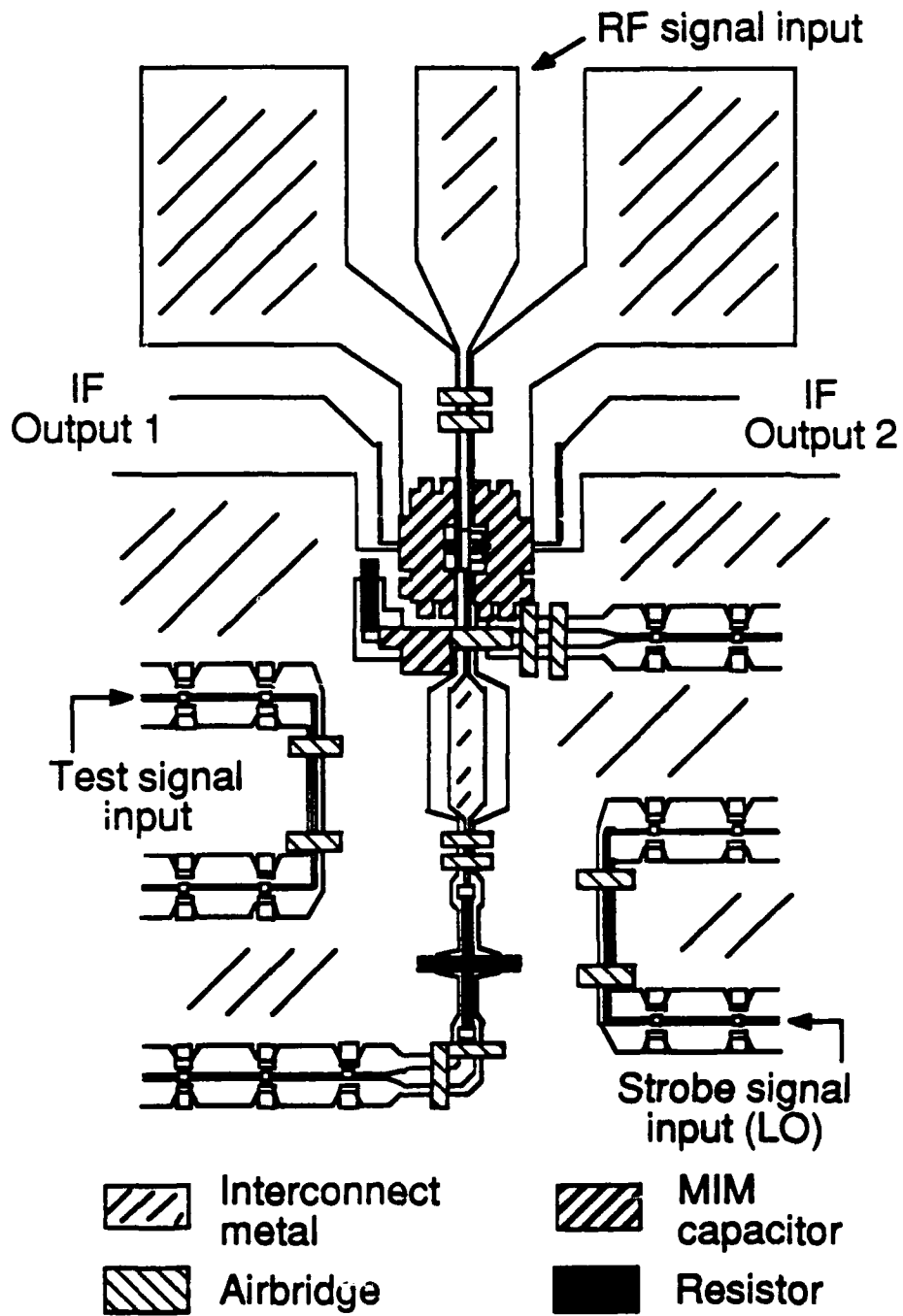


Figure 3.20: Generation III sampler layout.

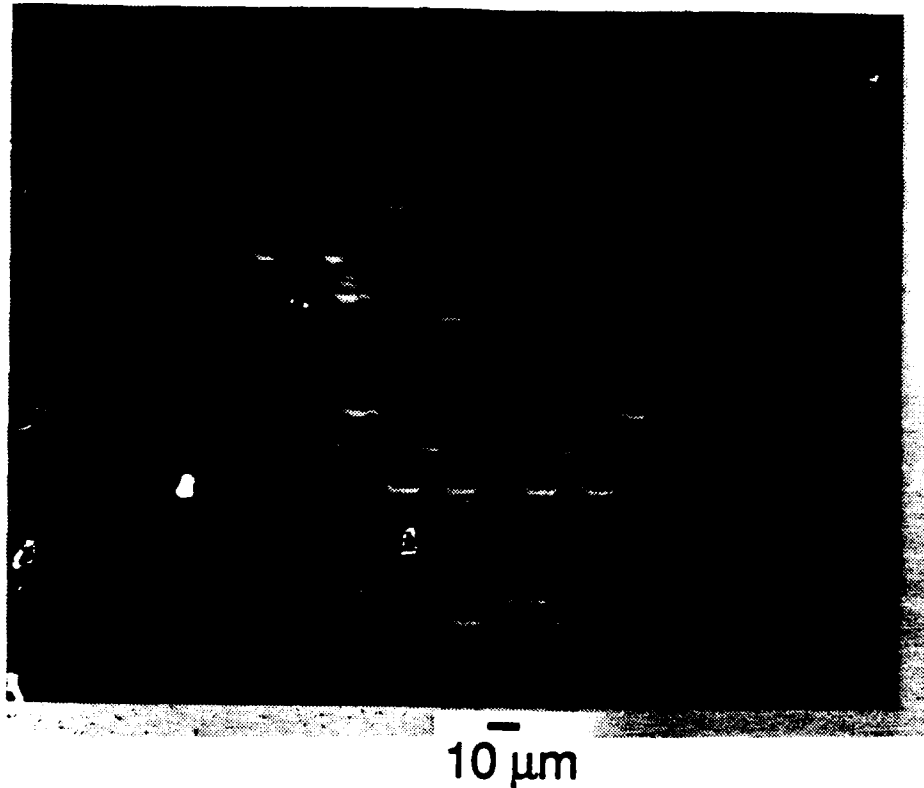


Figure 3.21: Scanning electron micrograph of the completed sampler

on for half of this time, 0.8 ps, as determined from the IF output impedance. The risetime limiting factors are summarized in Fig. 3.24 and compared with those of Generation I, Generation II being essentially the same as Generation I. The input-referred noise voltage was  $0.6\mu V/\sqrt{Hz}$ . The 1 dB compression point was -1 dBm. The rise-time of the sampler is estimated at 1.2 ps, which corresponds to a 290 GHz 3 dB bandwidth.

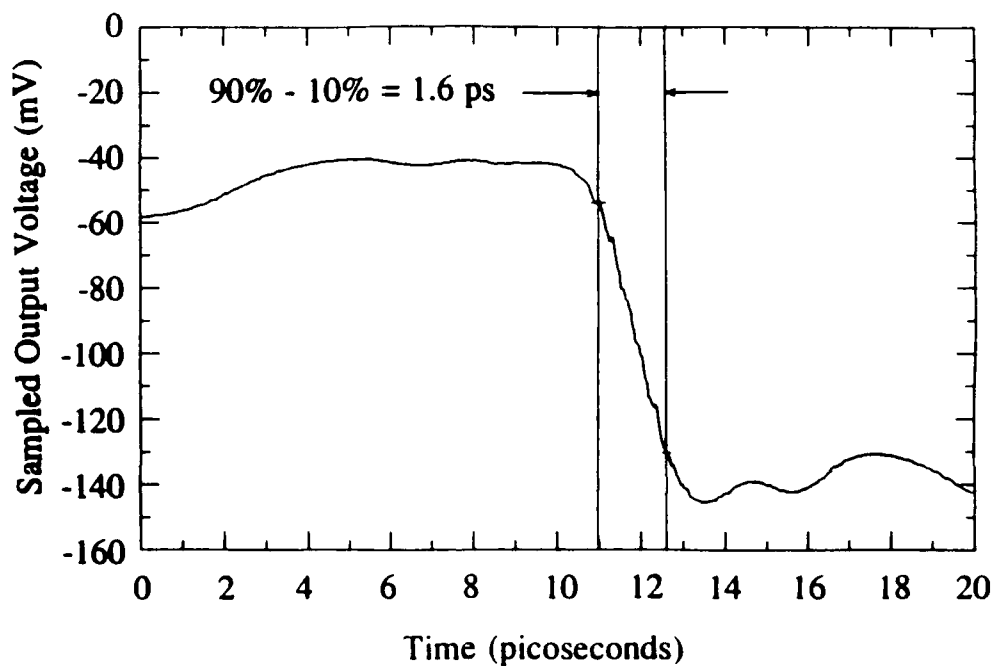


Figure 3.22: Sampled output of the 10:1 attenuated nonlinear transmission line. The measured falltime is 1.6 ps; the actual falltime is estimated to be 1.1 ps.

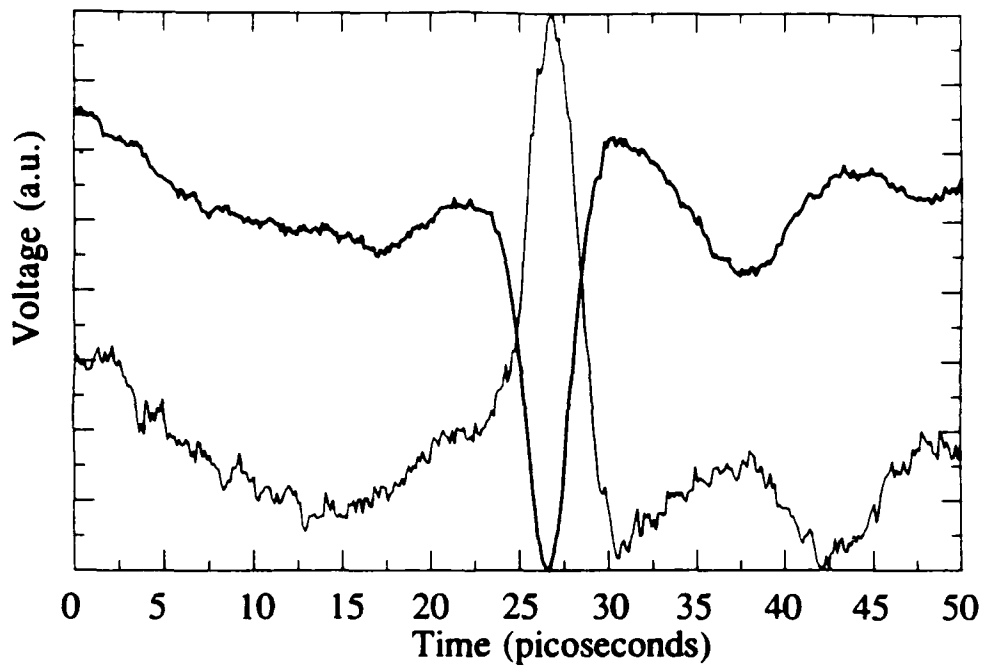


Figure 3.23: Electrooptically sampled Generation III sampler strobe pulses. The positive going waveform is the voltage strobe pulse appearing at the anode of  $D_2$ ; the negative going pulse is at the cathode of  $D_1$ .

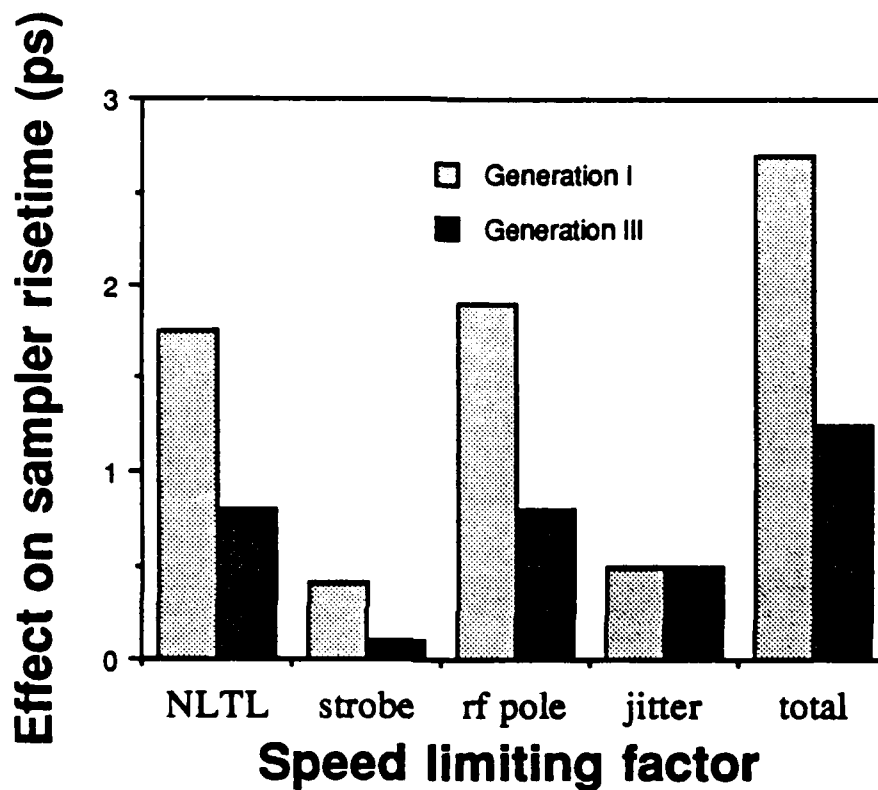


Figure 3.24: Comparison of risetime limiting factors. Column 1 is the NLTL output falltime divided by two which is diode aperture time in the absence of parasitics. Column 2 represents the contribution the sampling diodes loading the strobe circuit while Column 3 shows their effect on the rf circuit. Timing jitter is depicted in Column 4 and the RSS total is shown in Column 5.

## References

- [3.1] H.L. Callendar, "An alternating cycle-curve recorder," *The Electrician*, 41, 582-586, August 26, 1898.
- [3.2] R.J.D. Reeves, "The recording and collocation of waveforms (part 1)," *Electronic Engrg.*, 31, 130-137, 1959.
- [3.3] R.J.D. Reeves, "The recording and collocation of waveforms (part 2)," *Electronic Engrg.*, 31, 204-212, 1959.
- [3.4] G.J. Frye, N.S. Nahman, "Random sampling oscillography," *IEEE Trans. Meas.*, IM-13, 8-13, 1964.
- [3.5] G.J. Frye, "Sampling system," United States patent no. 3,629,731, 1971.
- [3.6] W.M. Grove, "Sampling for oscilloscopes and other rf systems: dc through x-band," *IEEE Trans. on Microwave Theory Tech.*, MTT-14, 629-635, 1966.
- [3.7] P.E. Allen, *Switched capacitor circuits*, Van Nostrand Reinhold, New York, (1984).
- [3.8] R.E. Ziemer, W.H. Tranter, D.R. Fannin, *Signals and systems: continuous and discrete*, Macmillan, New York, (1983).
- [3.9] H. Wallman and G.E. Valley, Jr., *Vacuum tube amplifiers*, McGraw-Hill, New York, (1948).
- [3.10] R.J. Matreci, "Unbiased subharmonic mixers for millimeter-wave spectrum analyzers," *Hewlett-Packard Journal*, 22-26, Nov. 1986.
- [3.11] C.J. Madden, M.J.W. Rodwell, R.A. Marsland, D.M. Bloom, and Y.C. Pao, "Generation of 3.5 ps fall-time shock waves on a monolithic nonlinear transmission line," *IEEE Electron Device Lett.*, 9, 303-305, 1988.
- [3.12] J. Merkelo, R.D. Hall, "Broad-band thin-film signal sampler," *IEEE J. Solid-State Circuits*, SC-7, 50-54, 1972.

- [3.13] S.R. Gibson, "Gallium arsenide lowers cost and improves performance," *Hewlett-Packard Journal*, **37**, No. 2, 4, 1986.
- [3.14] M.J.W. Rodwell, D.M. Bloom, and B.A. Auld, "Nonlinear Transmission Line for picosecond pulse compression and broadband phase modulation," *Electr. Lett.*, **23**, 109-110, 1987.
- [3.15] K.C. Gupta, R. Garg, I.J. Bahl, *Microstrip lines and slotlines*, Artech House Inc, Norwood, (1979).
- [3.16] J.K. Hunton and J.S. Takeuchi, "Recent developments in microwave slotline mixers and frequency multipliers," *Digest of Tech. Papers, G-MTT Symp.*, 196-199, 1970.
- [3.17] M. Caulton, "Lumped elements in microwave integrated circuits," in *Advances in microwaves*, (ed. by L. Young and H. Sobol), Vol. 8, Academic Press, New York, 1974.
- [3.18] R. Majidi-Ahy, B.A. Auld, and D.M. Bloom, "100 GHz on-wafer S-parameter measurements by electrooptic sampling," *IEEE MTT-S International Microwave Symposium*, 299-302, 1989.
- [3.19] R.A. Marsland, V. Valdivia, C.J. Madden, M.J.W. Rodwell, D.M. Bloom, "130 GHz GaAs monolithic integrated circuit sampling head," *Appl. Phys. Lett.*, **55**, 592-594, 1989.
- [3.20] Wiltron Company, 490 Jarvis Drive, Morgan Hill, CA.
- [3.21] C.J. Madden, R.A. Marsland, M.J.W. Rodwell, D.M. Bloom, and Y.C. Pao, "Hyperabrupt-doped GaAs nonlinear transmission line for picosecond shock-wave generation," *Appl. Phys. Lett.*, **54**, 1019-1021, 1989.

## Chapter 4

# S-parameter test-set on a chip

### 4.1 Introduction

To make S-parameter measurements, more is required than just a fast sampler; it is also necessary to separate the forward and reverse traveling waves. There are two methods which are widely used for the separation. One method takes advantage of the directionality provided by coupled transmission lines [4.1]. The second method, shown in Fig. 4.1, uses the directionality provided by the Wheatstone or directional bridge. The first method, being fully distributed, has the potential for higher frequency operation. However, it is exceedingly difficult to simultaneously achieve high directivity (greater than 20 dB) and ultra-broad bandwidth (greater than 3 decades). For example Krytar [4.2] offers a directional coupler with 20 dB directivity from 2 to 8 GHz, but the directivity degrades to 16 dB when the frequency range is extended to 1 to 20 GHz and degrades further to 10 dB when extended to cover the 1 to 40 GHz range. Wiltron Company [4.3] uses directional couplers in their 60 GHz network analyzer but, again, the directivity is only 10 dB. The bridge method could conceivably work at all frequencies, provided the resistors and interconnections could be made relatively parasitic free. The limitations of this technique are imposed by the voltage meter across the middle of the bridge. An improved version of this technique which uses a floating sampler is presented in the following sections. The floating sampler samples the voltage between two nodes

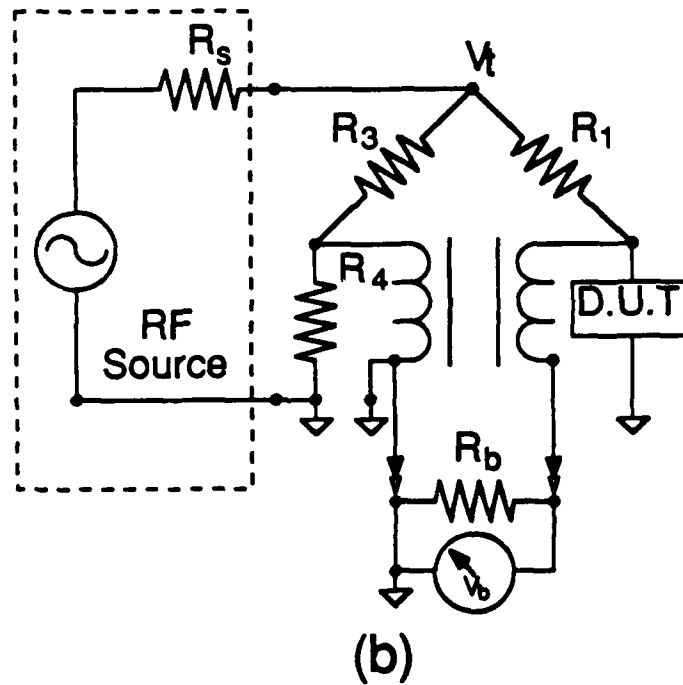
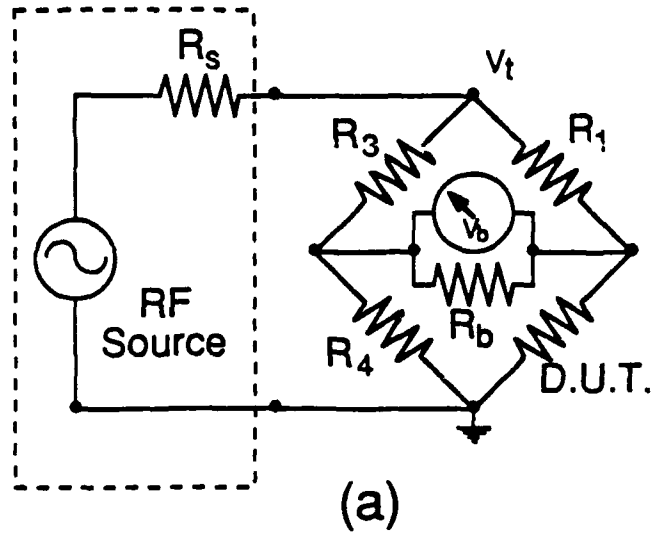


Figure 4.1: Directional bridge with (a) floating sampler and (b) single-ended sampler and balun.

where, contrary to previous practice, neither of the nodes need be grounded.

## 4.2 Directional sampler theory

The resistor bridge of 4.1a known as the Wheatstone or directional bridge, is balanced when [4.4]

$$R_4 R_1 = R_3 Z_d \quad (4.1)$$

where  $R_1$ ,  $R_3$ , and  $R_4$  can be complex impedances but in this case are chosen to be real. The impedance of the device under test or D.U.T.,  $Z_d$ , is generally complex. The bridge is designed so that Eq. (4.1) holds when  $Z_d = R_0$ , where  $R_0$  is the reference impedance, often chosen to be  $50\Omega$ . Under these conditions, the bridge output voltage  $V_b$  will be equal to zero when the impedance of the device under test equals the reference impedance. This property is useful for measuring impedance levels very close to  $R_0$ . As  $Z_d$  approaches  $R_0$ , the voltage  $V_b$  becomes proportional to the amplitude of the reflected wave from  $Z_d$ . When all the resistors are set to  $R_0$ ,

$$V_b = \frac{V_s}{8} \left( \frac{Z_d - R_0}{Z_d + R_0} \right) \quad (4.2)$$

which is directly proportional to the reflection coefficient,  $\Gamma_d$  for all  $Z_d$  [4.5].

The difficulty is measuring the magnitude and phase of the floating voltage at high-frequencies. Usually, the voltage across the bridge is measured by using a balun to convert the voltage difference to a voltage referenced to ground, as shown in Fig. 4.1b [4.6]. However, the floating sampler presented here makes the balun superfluous. The floating sampler samples the voltage between two nodes where neither of the nodes need be grounded.

The single-ended sampler operation described in Chapter 3 measures a voltage with respect to ground because nodes (e) and (c) are at zero rf potential. Now suppose that another source  $V_2$  is connected to nodes (c) and (e) as in Fig. 4.2, where  $V_1$  corresponds to the original source. Now, since the impedance looking into the normally off diodes is high, the voltage at node (a) is  $V_1$ , the voltage at node (b) is  $V_2 + V_{SP}/2 + V_{c1}$ , and the voltage at node (d) is  $V_2 - V_{SP}/2 + V_{c2}$ , where  $V_{c1,2}$  is the dc voltage on capacitors  $C_{1,2}$ . Setting the voltage difference across diode D1

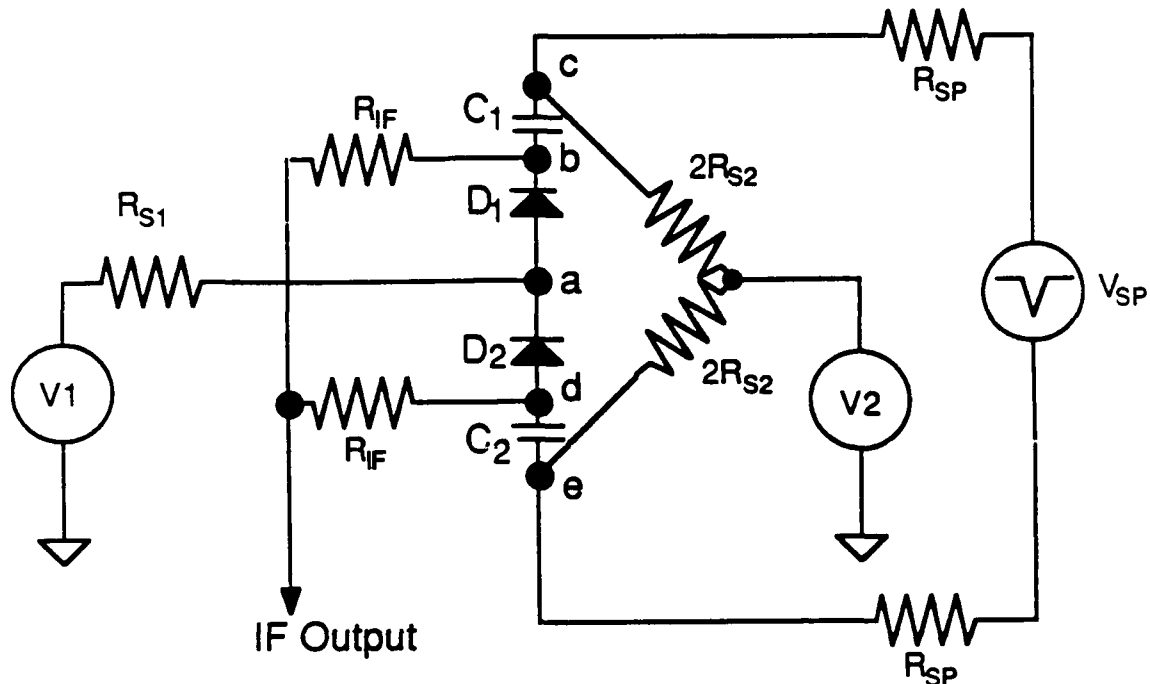


Figure 4.2: Diagram illustrating how a floating voltage can be sampled. The two sources must have constant relative phase.

equal to zero during the peak of the strobe pulse gives,  $V_{c1} = V_1 - V_2 - V_{SP}/2$  and  $V_{c2} = V_1 - V_2 + V_{SP}/2$ . So the voltage at the IF output which is halfway between these two voltages is  $V_{IF} = (V_1 - V_2)/2$ . Thus, the voltage at the IF port will follow the voltage difference  $V_1 - V_2$  at the IF frequency. This sampler is called a floating sampler because there is an RF potential on both sides of the sampling diodes whereas in conventional samplers, one side of the diode is always zero rf potential. Care must be taken in designing a floating sampler because the IF output nodes, (b) and (d) are no longer at zero rf potential. To avoid loading these nodes, a sizeable IF resistor with substantial inductance at the lowest rf frequency should be used when connecting nodes (b) and (d) to the IF output port. Resistors may be placed in series with the IF output without significant signal degradation because the output

impedance of the samplers at the IF frequency is typically on the order of  $20k\Omega$  (see Fig. 3.5).

Finally, the floating sampler is connected to a modified Wheatstone bridge in Fig. 4.3. The left side of the Wheatstone bridge has been split into parallel arms

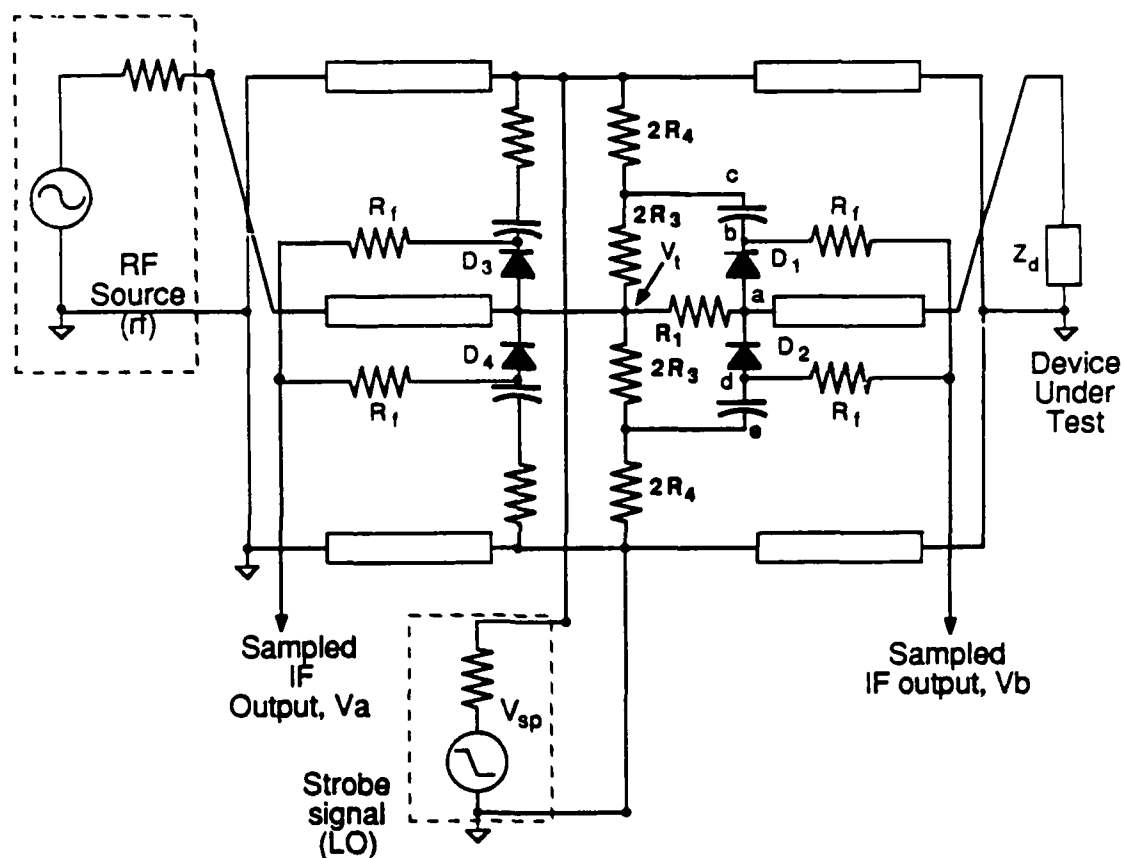


Figure 4.3: Schematic diagram of directional bridge using a floating sampler instead of a balun. The bridge is 'unfolded' to provide a means of strobing the sampling diodes

to provide a means of turning on the sampling diodes (this is the same idea as in splitting the source resistor  $R_{s2}$  in Fig. 4.2). The two arms are a mirror image across the horizontal so the rf source which excites them equally will see them in parallel and the rf potential at node (c) will be equal to that at (e). However, the strobe generator, which is applied across the split in the rf ground plane in Fig. 4.3, sees the resistors and the diodes in series. Thus, as described in the previous paragraph,

the IF output of the floating sampler will track the voltage difference from node (a) to node (c) at the IF frequency. So the circuit now performs the function of both the directional device and the sampler B of Fig. 1.2.

Above, it was mentioned that it is desirable to have all resistors in Fig. 4.1a equal to  $50\Omega$ . However, when the bridge is unfolded to as discussed above, some of the resistor values must be doubled. Since  $100\Omega$  resistors are quite large when fabricated with  $N^+$  material as discussed in Chapter 2, a compromise design is necessary. Removing  $R_b$  from the circuit and adjusting the remaining resistors to achieve test-port input-match and balance at  $Z_d = R_0$ , the reference impedance, yields a set of resistor values all under  $100\Omega$ . The voltage at the bridge output is now,

$$V_b = V_i \left( \frac{R_3}{R_4 + R_3} \right) \left( \frac{Z_d - R_0}{Z_d + R_1} \right) \quad (4.3)$$

which is not proportional to the device reflection coefficient  $\Gamma_d$  unless  $Z_d \approx R_0$ , because  $R_1 \neq R_0$ . So, to obtain  $\Gamma_d$  based on the measurement of  $V_b$  in Eq. (4.3), it is necessary to use a linear fractional transformation (LFT) [4.7] (also called the bilinear or Möbius transformation [4.8]), which has the form  $f(z) = \frac{a+bz}{c+dz}$  where  $z$  is a complex variable. This is the general form of the transformation used to remove errors in two-port vector network analyzers due to source mismatch, cross-talk between ports, directivity, and transmission loss [4.5]. So, when the test-set is measuring the  $\Gamma_d$  of the device under test, it is as if the usual systematic errors listed above are performing a LFT on the actual value of  $\Gamma_d$  and the transfer function of Eq. (4.3) is performing a LFT on this data. Since the LFT of an LFT is an LFT, and since the LFT is a one-to-one transformation, the same calibration procedure that is used to remove the usual systematic errors will simultaneously compensate for  $R_1$  not being equal to  $R_0$ . It can also be shown that having  $R_1 \neq R_0$  does not increase the sensitivity of the calibrated data to changes in the absolute value of  $R_1$ . From this point of view, the difference between the transfer functions of Eqs. (4.3) and (4.2) is quite superficial.

To provide match at the test port,

$$R_0 = R_1 + \frac{R_s(R_3 + R_4)}{R_s + R_3 + R_4} \quad (4.4)$$

must be satisfied. When Eqs. (4.4) and (4.1) are both satisfied,

$$R_4 = \frac{R_0^2(R_0 - R_1)}{R_1(R_0 + R_1)}$$

For the monolithic directional sampler, the following values were used:

$$R_1 = 25\Omega, R_3 = 16.7\Omega, R_4 = 33.3\Omega, R_s = 50\Omega$$

Even though  $R_3$  and  $R_4$  must be doubled, as in Fig. 4.3, the entire set of values is less than  $100\Omega$  and easily implemented with  $N^+$  material.

The second sampler, sampler A of Fig. 1.2, can be readily added to the circuit by simply connecting a sampler of the non-floating variety on the left side of Fig. 4.3. This sampler is driven from the same source as the floating sampler, so no additional strobe generator is needed. Since this sampler directly measures,  $V_i$ , the  $\Gamma_d$  dependence of  $V_i$  is not important as it will be divided out. The completed circuit now replaces both samplers as well as the directional device of Fig. 1.2. By using coplanar waveguide (CPW) for the transmission line sections of Fig. 4.3, the entire circuit can be fabricated in a monolithic integrated circuit.

## 4.3 Monolithic directional sampler

### 4.3.1 Design and layout

A plan view of the directional sampler is shown in Fig. 4.4. The directional sampler was fabricated on a semi-insulating GaAs substrate using the process described in Chapter 2. The strobe pulse is generated by a hyperabrupt-doped NLTL [4.9] on a separate chip. This pulse is applied across the narrow CPW grounds from the bottom port. The rf excitation is provided to the port on the left of Fig. 4.4, and the right port is connected to the device under test. The CPW grounds are shorted together by airbridges  $250\mu\text{m}$  from the center to provide a 5 ps round-trip time for the applied sampling pulse which has a transition time of approximately 5 ps. When the strobe pulse is applied,  $V_i$  and  $V_o$  are simultaneously sampled. The down converted signals are filtered by  $100\Omega$  resistors and delivered to bond pads on the left and right sides of the chip.

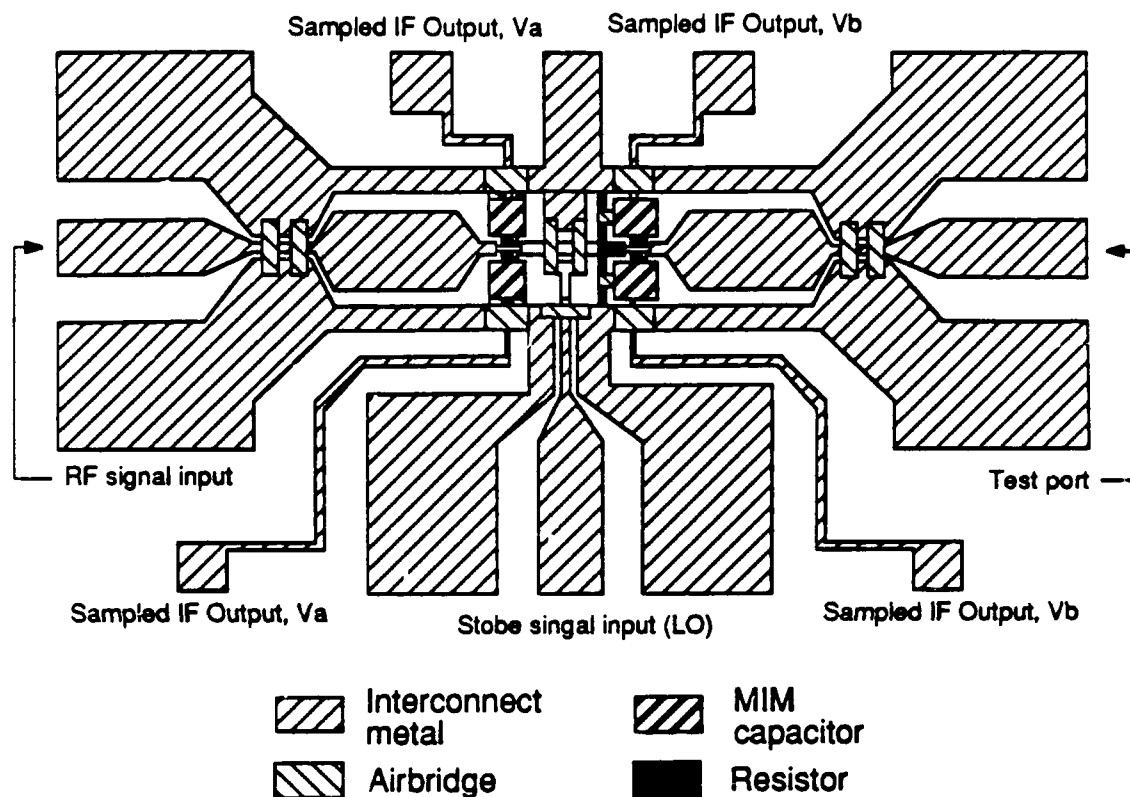


Figure 4.4: Layout of the directional sampler.

The resistors of the directional bridge were  $5 \mu\text{m}$  wide. The small size was necessary to fit all five resistors in the small space between the two rf grounds. Because of the variations in contact resistance described in Chapter 2, these resistors have a tolerance of 22%. Differentiating Eq. 4.3 gives the sensitivity of the output voltage of the bridge for  $Z_d = R_0$  normalized to the output voltage for  $Z_d \rightarrow \infty$ ,

$$\frac{\partial V_b(Z_d = R_0)}{V_b(Z_d \rightarrow \infty)} = \frac{-2}{3} \left\{ \frac{\partial R_1}{R_1} - \frac{\partial R_3}{R_3} + \frac{\partial R_4}{R_4} \right\} \quad (4.5)$$

The measured values for a typical die were  $R_1 = 20\Omega$ ,  $R_3 = 18\Omega$ ,  $R_4 = 30\Omega$ . Using

these values and the design values in Eq. (4.5) yields a predicted output voltage for a matched load normalized to the open circuit voltage of 0.24 or 12.4 dB. This number is the effective directivity of the bridge.

### 4.3.2 Results

Because the directional sampler, like any sampler, has a relatively high impedance IF output (see Fig. 3.5), it is difficult to perform on-wafer testing of the monolithic directional sampler circuits without cross-talk between the IF outputs or excessive capacitive loading. So, the circuits were diced and assembled with a NLTL strobe pulse generator in a 60 GHz package using Wiltron V-connectors<sup>1</sup> on the rf and test ports. The IF output bond pads were connected to the low-frequency output pins on the package with  $\sim 1$  cm bond wires to help filter out any rf. An rf signal between 2 and 60 GHz was applied to the rf port while the NLTL drive (LO) was maintained between 2 and 6 GHz, so that the proper harmonic mixes the rf signal and the floating bridge voltage down to the 90 MHz IF frequency (see Fig. 4.5). Two external mixers were then used to convert the IF to the 20 MHz used by the Hewlett-Packard 8510B network analyzer. The 'first' IF was chosen to be 90 MHz so that the Wiltron 90 MHz buffer amplifier could be used. The 8510B was used as the vector receiver because it was readily available and easily adapted to drive the rf and LO signal generators at the proper frequencies.

With the directional sampler configured as described above, it can be used as a one-port S-parameter test set for the 8510B. Two types of measurements were made in this mode. First, the uncalibrated reflection coefficient (simply the ratio of the two IF vector voltages) was measured for an open, load and a short. The difference in magnitude between the uncalibrated reflection coefficient of the open and that of the load is a measure of the directivity. This is an imperfect directivity measurement since imperfections in the load or losses in the open will degrade the observed difference. However, this measurement puts a lower bound on the directivity. The directional sampler required large LO power ( $\sim 30$  dBm) drive to

---

<sup>1</sup>V-connector is a trademark of Wiltron Company

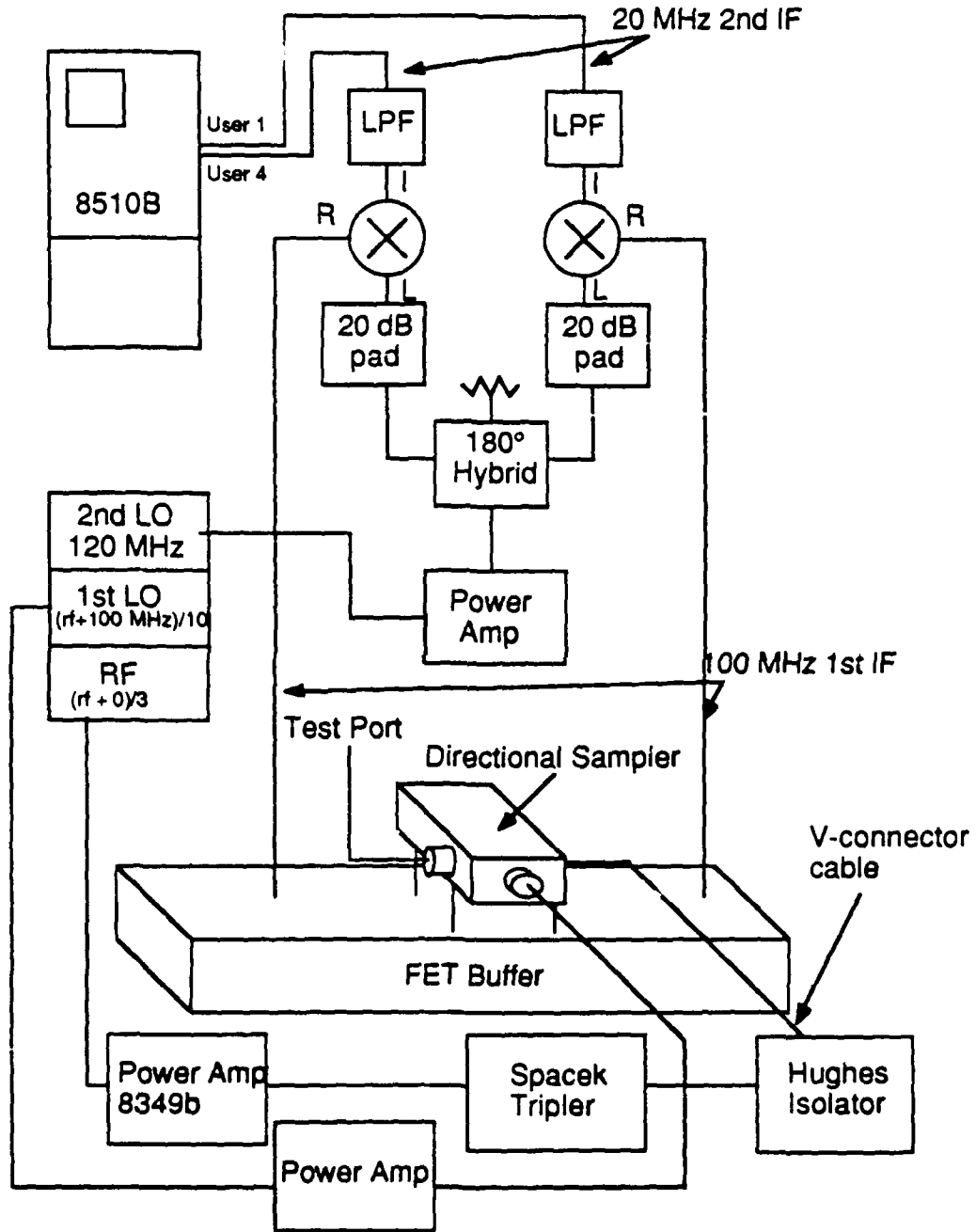


Figure 4.5: Directional sampler S-parameter test set-up. The 8510B in external mixer mode, controls the two synthesizers to produce a signal at the 90 MHz first-IF.

the NLTL for optimum performance. This power was available between 2-4 GHz so measurements were made using this LO range and an rf frequency from 2 to 4 GHz, 4 to 8 GHz, 8 to 16 GHz, 12 to 24 GHz, 20 to 40 GHz (using a frequency doubler), and 40 to 60 GHz (using a frequency tripler). The directivity over the entire 2 to 60 GHz range was better than 10 dB. A typical result is shown in Fig. 4.6. Next,

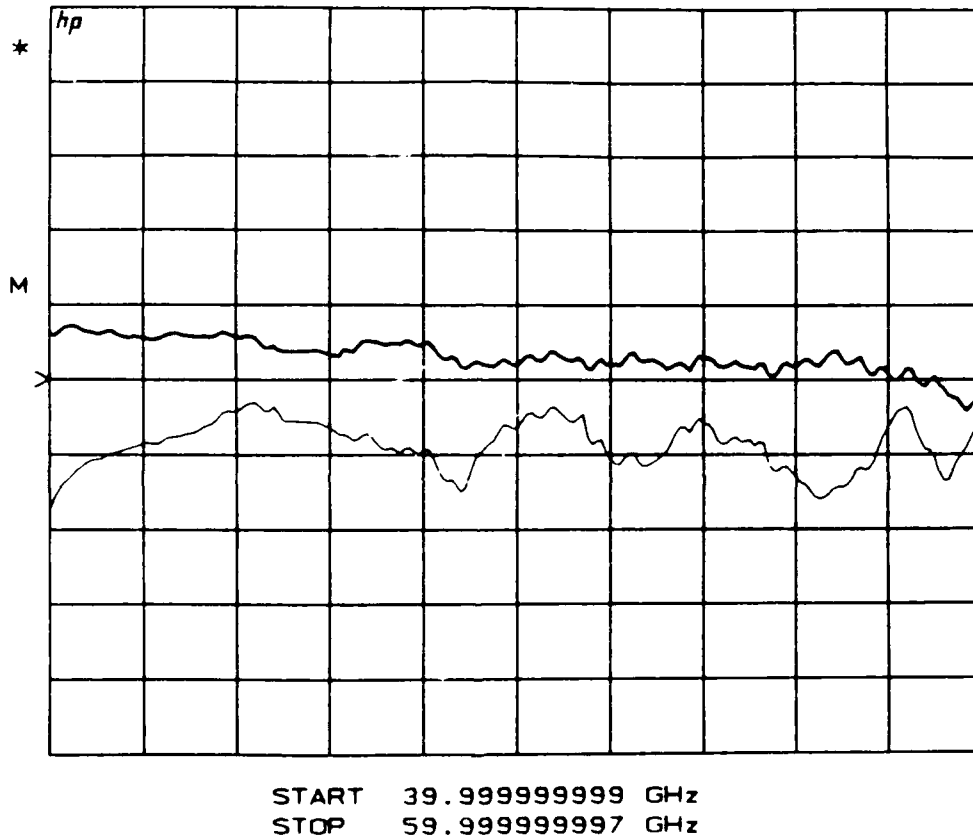


Figure 4.6: Uncalibrated S-parameter measurement with the directional sampler from 40 to 60 GHz. The heavy trace is the magnitude of the reflection from an open V-connector. The lighter trace is that of a load with a 2.4 mm connector.

a calibrated S-parameter measurement was performed. The standard “open-short-load” calibration procedure was used over a frequency range where connector losses were low and therefore the effective directivity was as high as possible. Figure 4.7 shows a typical calibration over the 8-16 GHz band. The calibration was limited to a single band at a time since the 8510B software can not skip LO harmonic numbers.

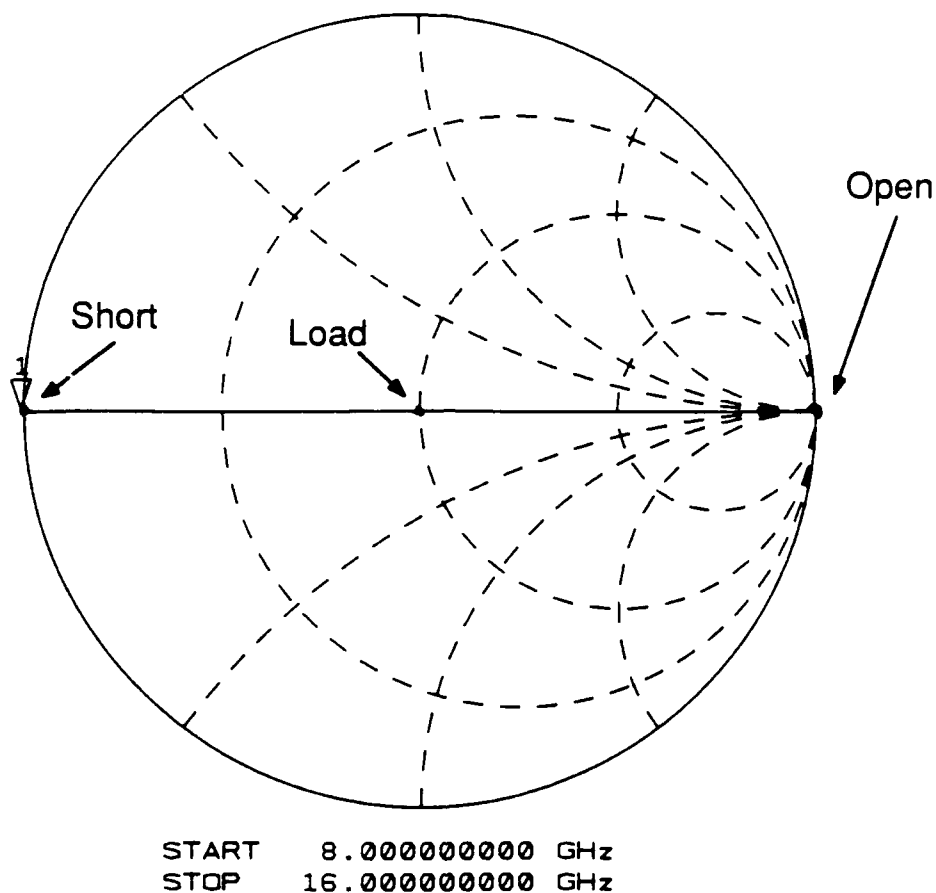


Figure 4.7: Open, short, and load measured by the directional sampler after calibration.

While 10 dB directivity to 60 GHz is no better than the best available coaxial directional coupler, the potential exists for much greater directivity and bandwidth. The measured 10 dB directivity is quite close to the predicted 12 dB directivity based solely on resistor values. If thin-film resistors trimmed within 10% of design value were added to the process, the directivity could be improved to 14 dB. If the sign of the resistor error was the same for all resistors (that is, if they were all high or all low) the directivity could be improved again to 23 dB. This directivity is independent of frequency since it is determined by the values of low-parasitic resistors. Therefore, using the techniques of Chapter 3, fabricating a 100 GHz, 20 dB directivity directional sampler should be a straightforward task, once a slightly

better resistor process is developed.

## References

- [4.1] W.H. Louisell, *Coupled mode and parametric electronics*, Wiley, New York, (1960).
- [4.2] Krytar, 1292 Anvilwood Ct. Sunnyvale, CA 94089.
- [4.3] Wiltron Company, 490 Jarvis Drive, Morgan Hill, CA 95037.
- [4.4] B.M. Oliver and J.M. Cage, *Electronic Measurements and Instrumentation*, McGraw-Hill, New York, (1971).
- [4.5] G.H. Bryant, *Principles of microwave measurement*, Peter Perengrinus, London, United Kingdom, (1988).
- [4.6] S.B. Donecker, J.K. Botka, U.S. Patent 4,588,970.
- [4.7] S.D. Fisher, *Complex variables*, Wadsworth & Brooks, Belmont, CA, (1986).
- [4.8] R.V. Churchill, J.W. Brown, and R.F. Verhey, *Complex variables and applications third edition*, McGraw-Hill, New York, (1976).
- [4.9] C.J. Madden, R.A. Marsland, M.J.W. Rodwell, D.M. Bloom, and Y.C. Pao, "Hyperabrupt-doped GaAs nonlinear transmission line for picosecond shock-wave generation," *Appl. Phys. Lett.*, **54**, 1019-1021, 1989.

## Chapter 5

# Distributed frequency multiplication

### 5.1 Introduction

Efficient frequency multipliers are important in a variety of systems. At millimeter-wave frequencies frequency multiplication is often the only practical way to achieve a phase-locked source of radiation [5.1]. Archer [5.2] has achieved 7.5 dB doubler conversion loss over a bandwidth of 90 to 124 GHz with a whisker-contacted varactor diode in a waveguide mount. While this result is impressive, a millimeter-wave doubler exploiting the distributed nonlinear interaction on a monolithic nonlinear transmission line (NLTL) [5.3] offers a much more compact, less expensive, and possibly more efficient method of harmonic generation. As a proof of this principle, Wedding and Jäger [5.4] have demonstrated 90% conversion efficiency on a macroscopic NLTL at radio-frequencies, through doubling from a forward to a *backward* wave in the upper passband of a periodic line. However, the tunability of this structure is not discussed. In this chapter, theory and experimental results of second-harmonic-generation (SHG) through doubling up from a forward wave to a *forward* wave in the upper passband of a modified NLTL is presented. This structure offers a broad electrical tuning range with reasonable impedance matching at both fundamental and second harmonic frequencies.

## 5.2 The diatomic lattice

To accomplish high efficiency SHG on a distributed network with large nonlinearity, it is necessary to prevent shock-wave formation, provide phase matching between the input and second-harmonic frequencies, and suppress higher order harmonics. One structure that accomplishes these goals is the electrical analogue of the diatomic lattice [5.5] shown in Fig. 5.1. The dispersion relation of the diatomic lattice is given

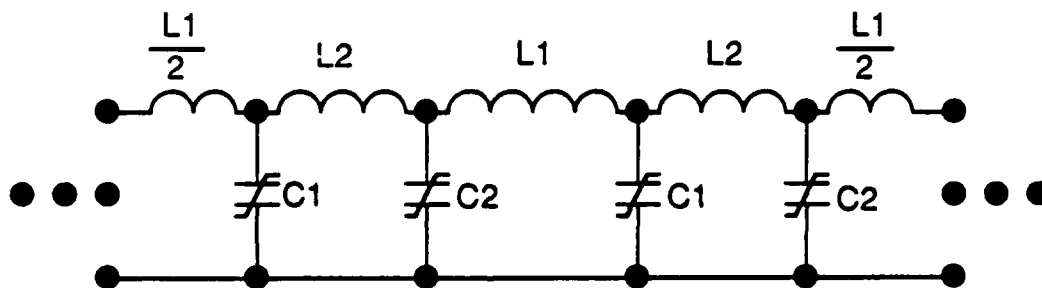


Figure 5.1: Electrical analog of the diatomic lattice. Inductance,  $L$ , replaces the atomic mass and capacitance  $C$ , replaces the spring constant.

by

$$\omega^2 = \frac{1}{2} \left( \frac{1}{L_1} + \frac{1}{L_2} \right) \left( \frac{1}{C_1} + \frac{1}{C_2} \right) \pm \sqrt{\frac{1}{4} \left( \frac{1}{L_1} + \frac{1}{L_2} \right)^2 \left( \frac{1}{C_1} + \frac{1}{C_2} \right)^2 - \frac{4 \sin^2(k/2)}{L_1 L_2 C_1 C_2}} \quad (5.1)$$

where  $L_1$  and  $L_2$  are shown in Fig. 5.1,  $C_1$  and  $C_2$  are the shunt capacitances of the varactor diodes, and  $k$  is the propagation constant in units of radians/section. The  $+$  root defines the upper branch and the  $-$  root defines the lower branch of the dispersion diagram in Fig. 5.2. From Fig. 5.2 it is evident that if the band gap is made sufficiently small, phase matched doubling from a forward wave on the lower branch to a backward wave on the upper branch is possible, as demonstrated by

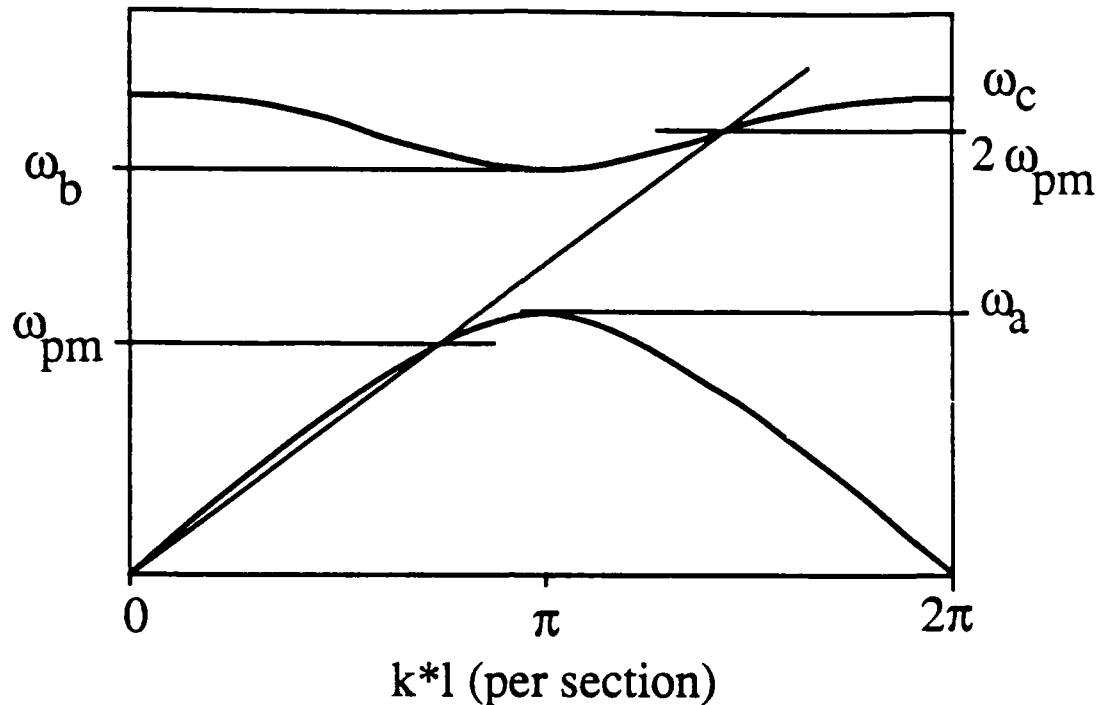


Figure 5.2: Dispersion relation of the diatomic lattice, showing the phase-matching condition and the band edges. At a fundamental frequency  $\omega_{pm}$ , the phase matching condition is satisfied. The first band edge is  $\omega_a = \sqrt{\frac{2}{L_1 C}}$ , the beginning of the second band is  $\omega_b = \sqrt{\frac{2}{L_2 C}}$ , and the high-frequency cut-off is  $\omega_c = \sqrt{\frac{2}{C}(\frac{1}{L_1} + \frac{1}{L_2})}$ .

Wedding and Jäger. However, if an attempt is made to tune the operating frequency by adjusting  $C_1$  or  $C_2$ , the band-gap will widen and possibly prevent propagation of the second harmonic. To avoid this problem, the choice  $C_1 = C_2 = C$  was made so that the shape of the dispersion relation is determined by the lithographically defined ratio  $L_1/L_2$ . Also, the doubler is designed to work with a fundamental forward wave and a second harmonic forward wave (Fig. 5.2). The phase matching condition for this case is

$$\omega_{pm} = \sqrt{\frac{2}{L_1 C}} \sqrt{1 + \frac{L_1}{L_2} - \sqrt{\frac{3L_1}{L_2}}} \quad (5.2)$$

This shows that phase matching can be accomplished over the entire tuning range of the capacitor  $C$ . Choosing the ratio  $L_1/L_2$  equal to 2.421, places the second

harmonic in the middle of its pass-band for all values of  $C$ , when the fundamental is driven at the tunable frequency  $\omega_{pm}$ .

Finally, the characteristic impedance of the structure is given by

$$Z_{B1,2} = \sqrt{\left(\frac{L_1 + L_2 - \omega_{1,2}^2 L_1 L_2 C/2}{2C}\right) \left(\frac{1 - \omega_{1,2}^2 L_1 C/2}{1 - \omega_{1,2}^2 L_2 C/2}\right)} \quad (5.3)$$

where  $Z_{B1,2}$  is the characteristic impedance at the fundamental  $\omega_1$  and the second harmonic  $\omega_2$ , respectively. It is not possible to simultaneously impedance match and phase match at both frequencies, so an impedance match is chosen only at the second harmonic. Combining the requirements of centering the second harmonic in its band, phase matching, and impedance match at the second harmonic yields

$$C = \frac{0.2489}{\omega_1}, L_1 = \frac{58.32}{\omega_1}, L_2 = \frac{37.48}{\omega_1}$$

### 5.3 Nonlinear analysis

If  $C$  is allowed to be nonlinear, and curve-fit a second order polynomial to the measured C-V relation in the region of interest,

$$C(V - V_0) = C^{(0)} + C^{(1)}(V - V_0) + C^{(2)}(V - V_0)^2$$

$C(V - V_0)$  can be substituted into the circuit equations of the structure to obtain the coupled mode equations [5.6]

$$\frac{da_{1+}}{dz} = -(\alpha_1 + jk(\omega))a_{1+} - jK_1 a_{2+} a_{1+}^* \quad (5.4)$$

$$\frac{da_{2+}}{dz} = -(\alpha_2 + jk(2\omega))a_{2+} - jK_2 a_{1+}^2 \quad (5.5)$$

$$K_1 = \sqrt{2Z_{B2}Z_{B1}}\omega_1 C^{(1)}$$

$$K_2 = \sqrt{2Z_{B1}Z_{B2}}\omega_1 C^{(1)}$$

Here,  $a_{1,2+}$  are the forward traveling waves at the fundamental and second harmonic, respectively. They are related to the instantaneous voltage by the equation

$$V = \sqrt{2Z_{B1}}(a_{1+}e^{j\omega t} + a_{1+}^*e^{-j\omega t}) + \sqrt{2Z_{B2}}(a_{2+}e^{j2\omega t} + a_{2+}^*e^{-j2\omega t})$$

Here,  $\alpha_{1,2}$  are the attenuation constants in Np/section at the fundamental and second harmonic respectively.

The coupled mode Eqs. (5.4), (5.5) are derived by first assuming a uniformly distributed transmission line with nonlinear capacitance, and then replacing  $\omega_1 Z_{B1} C^{(0)}$  with  $k(\omega_1)$  and  $2\omega Z_{B2} C^{(0)}$  with  $k(\omega_2)$ . This allows the correct dispersion relation to be used, while separating the problem of determining the dispersion from the nonlinear problem. Terms involving  $C^{(1)}$  yield the usual equations for SHG, while terms with  $C^{(2)}$  add the effect of the power dependant phase-velocity, which can adversely effect phase-matching.

In the present case, losses turned out to be more important than pump depletion due to conversion or  $C^{(2)}$  effects, so an analysis similar to the analysis of Champlin et. al. [5.7] can be used. This yields the solution

$$a_{2+} = \left( \frac{K_2 a_{10}^2}{\alpha_2 - 2\alpha_1} \right) (e^{-2\alpha_1 z} - e^{-\alpha_2 z}) \quad (5.6)$$

which has a maximum at

$$z = \frac{1}{2\alpha_1 + \alpha_2} \ln \left( \frac{2\alpha_1}{\alpha_2} \right) \quad (5.7)$$

where the conversion efficiency will be

$$\eta_{max} = \left[ \frac{K_2 a_{10}}{\alpha_2} \left( \frac{\alpha_2}{2\alpha_1} \right)^{\frac{1}{1 - \frac{\alpha_2}{2\alpha_1}}} \right]^2 \quad (5.8)$$

## 5.4 Losses on the distributed doubler

Equation (5.8) shows that the conversion efficiency is critically dependent on the attenuation at the fundamental and second harmonic. Resistance of the interconnecting transmission lines, diode series resistance, and radiation all contribute to the attenuation of the doubler line. The attenuation coefficients due to conductor and dielectric loss on a TEM transmission line are

$$\alpha_c = \frac{R}{2Z}, \quad \alpha_d = \frac{G_d Z}{2} \quad (5.9)$$

where  $R$  is the effective resistance per unit length of the transmission line,  $Z$  is the characteristic impedance of the line, and  $G_d$  is the dielectric conductance per unit

length. The inductors  $L_1$  and  $L_2$  will be implemented with short, high-impedance sections of coplanar waveguide (CPW) and the capacitors with reverse biased Schottky diodes, as with the NLTL. Conductor loss on CPW is given by [5.8]

$$\alpha_c^{CPW} = 5.62 \times 10^{-5} R_s \epsilon_{re} Z_{0cp} \frac{P'}{\pi W} \left(1 + \frac{S}{W}\right) \times \left\{ \frac{\frac{1.25}{\pi} \ln \frac{4\pi S}{t} + 1 + \frac{1.25t}{\pi S}}{\left[2 + \frac{S}{W} - \frac{1.25t}{\pi W} (1 + \ln \frac{4\pi S}{t})\right]^2} \right\} \quad (5.10)$$

$$\epsilon_{re} \approx \frac{\epsilon_d + 1}{2} \quad (5.11)$$

$$R_s = \sqrt{\frac{\omega \mu \rho}{2}} = 9.81 \times 10^{-3} \sqrt{\frac{f}{1 \text{ GHz}}} \quad (5.12)$$

$$P' \approx \frac{\pi^2}{2k \ln^2 \frac{4}{k}} \text{ for } k < 0.1 \quad (5.13)$$

$$k = \frac{S}{S + 2W} \quad (5.14)$$

where  $\alpha_c$  is the loss in Np/unit length on a coplanar waveguide with center conductor width  $S$ , center conductor to ground spacing  $W$ , characteristic impedance  $Z_{0cp}$ , surface resistance  $R_s$ , and metal thickness  $t$  patterned on a substrate with a relative dielectric constant of  $\epsilon_d$ . Equating Eq. (5.10) with the conductor loss expression in Eq. (5.9) yields an effective series resistance for the unloaded transmission line,  $R_{CPW} = 2Z_{0cp}\alpha_c^{CPW}$ . When the capacitances of the shunt connected Schottky diodes are connected to the CPW, the characteristic impedance will be changed to that given by Eq. (5.3) but the physical resistance  $R_{CPW}$  will not change. The attenuation coefficient due to conductor losses of the diode loaded line is therefore

$$\alpha_c = \frac{Z_{0cp}}{Z_B} \alpha_c^{CPW} \quad (5.15)$$

Losses due to shunt conductance are dominated by the Schottky diode losses. The diode model is simply a series resistance  $R_d$  and a large signal junction capacitance  $C_{i_s}$ . The series  $R_d, C_{i_s}$  network can be converted into a parallel  $G_d, C_{i_s}$  network where the shunt conductance  $G_d$  is given by

$$G_d = \omega^2 C_{i_s}^2 R_d \quad (5.16)$$

Combining Eq. (5.16) with the expression for  $\alpha_d$  in Eq. (5.9) yields the attenuation in  $N_p$ /diode due to diode series resistance. Since there are two diodes per doubler section, the attenuation per section is

$$\alpha_d = \omega^2 C_{i_s}^2 R_d Z_B \quad (5.17)$$

Radiation losses are much more difficult to quantify. However, a qualitative analysis can reveal at least the order of magnitude. Figure 5.3 shows how the currents of the doubler line can be represented by an array of dipoles. The dipole

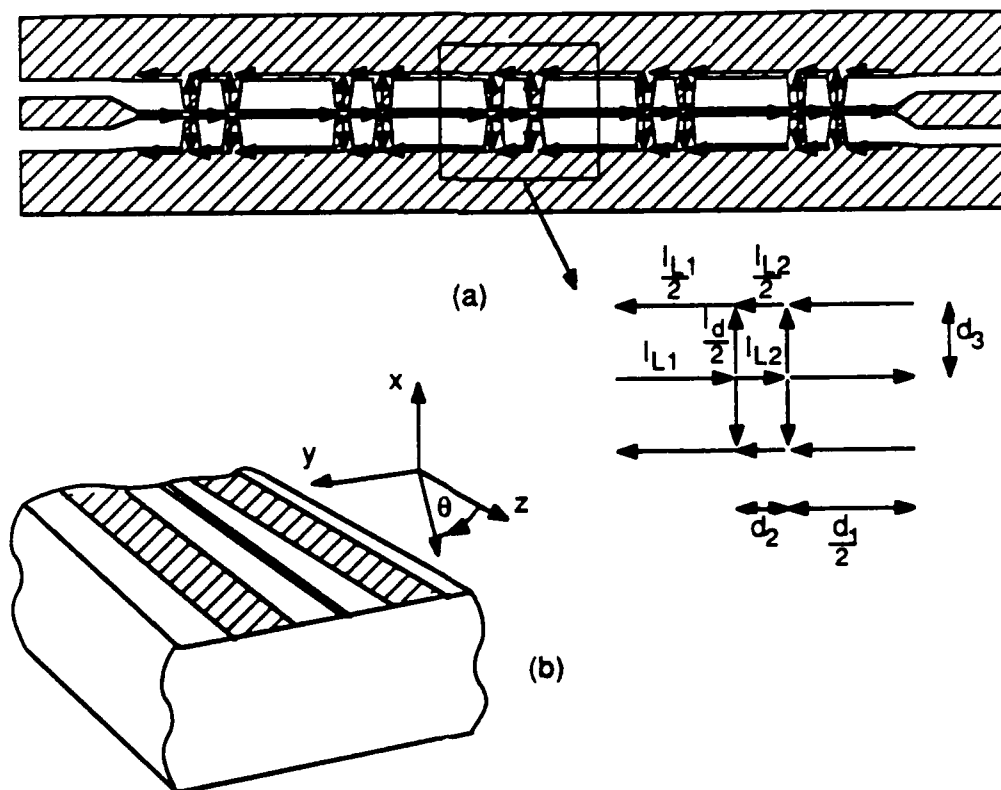


Figure 5.3: Radiation sources on the distributed doubler. The dipole representation of a section is shown in the inset. The CPW geometry and coordinate system is also shown (b).

representation of a section shown in the inset is repeated with a spacing  $d_1 + d_2$ . If

the far field, or Fraunhofer diffraction pattern of the section is  $f(\theta, \phi)$ , then, using the principle of pattern multiplication, the total radiation pattern of the doubler line is

$$f_T = f(\theta, \phi) \frac{\sinh \frac{M\gamma}{2}}{\sinh \frac{\gamma}{2}} \quad (5.18)$$

where  $M$  is the total number of sections and

$$\gamma = j \left\{ \frac{2\pi(d_1 + d_2)}{\lambda} \cos \theta - k(\omega) \right\} - \alpha \quad (5.19)$$

where  $\lambda$  is the wavelength in the substrate material,  $k(\omega)$  is the phase shift per section given by Eq. (5.1), and  $\alpha$  is the total loss per section. The radiated field is maximized when

$$\frac{2\pi(d_1 + d_2)}{\lambda} \cos \theta - k(\omega) = 2n\pi; \quad n = 0, \pm 1, \pm 2, \pm \dots \quad (5.20)$$

This is satisfied when

$$\cos \theta = \frac{(2n\pi + k(\omega))\lambda}{2\pi(d_1 + d_2)} \quad (5.21)$$

When  $n = 0$ , Eq. (5.21) reduces to the usual condition for Cherenkov radiation. However, because this is a periodic and not a uniform transmission line, the additional solutions with  $n \neq 0$  exist. These extra solutions have no effect on the lower branch of the dispersion relation, but allow significant portions of the upper branch to radiate. Therefore, to minimize loss due to radiation in the upper branch, the section pattern amplitude  $f(\theta, \phi)$  must be minimized by making  $d_3$  as small as possible.

## 5.5 Results

A monolithic frequency doubler using  $L_1 = 186\text{pH}$ ,  $L_2 = 77\text{pH}$ , and  $C = 79\text{fF}$  was designed. The layout and dimensions are shown in Fig. 5.4. The inductances of the CPW sections are  $L_{1,2} = d_{1,2}Z_{0\text{cpw}}/v$  where  $v$  is the phase velocity on the unloaded CPW. The impedance of the CPW is  $90\Omega$  so the  $L_1$  section is  $219\ \mu\text{m}$  long and the  $L_2$  section is  $83\ \mu\text{m}$  long. The capacitance of the  $L_1$  line section is  $22\ \text{fF}$  and is  $8.2\ \text{fF}$  for the  $L_2$  section. Consistent with previous NLTL designs

using  $90\Omega$  line sections, the center conductor width was chosen to be  $10\ \mu\text{m}$ , with a  $60\ \mu\text{m}$  spacing to ground. The stray capacitance in parallel with the Schottky diode is estimated to be  $4.4\ \text{fF}$ , using a CPW model. The total line capacitance per diode is  $11 + 4.1 + 4.4 = 19.5\ \text{fF}$ . The balance of the  $79\ \text{fF}$  is provided by the Schottky diode with  $1.5\ \text{V}$  reverse bias, so the zero bias junction capacitance is  $C_{j0} = 100\ \text{fF}$ . The doublers were placed on the same mask as the generation III samplers so the  $N^-$  layer was  $0.3\ \mu\text{m}$  thick and uniformly doped at  $1.2 \times 10^{17}$ . The diode area for the  $100\ \text{fF}$   $C_{j0}$  on this material is  $4 \times 20\ \mu\text{m}$ . The Schottky diodes and interconnecting CPW were formed according to the process described in Chapter 2.

Based on Eqs. (5.15) and (5.17) the total attenuation excluding radiation loss is expected to be  $\alpha_c + \alpha_d = 0.056 + 0.022 = 0.078\ \text{Np/section}$  at  $50\ \text{GHz}$  and  $0.079 + 0.088 = 0.17$  at  $100\ \text{GHz}$ . A curve fit to the measured C-V relation of the doubler line gives  $C^{(1)} = 13.6\ \text{fF/V}$ . For a  $20\ \text{dBm}$  input,  $K_2 a_{10} = 0.45\ \text{radians/section}$ . The predicted conversion based on these values is greater than  $100\%$ , invalidating the assumption that the fundamental is not depleted by conversion. However, the actual losses were significantly greater and  $K_2$  was smaller than expected.

The doublers were tested using direct-electrooptic sampling (described in Chapter 1). Preliminary measurements used the  $0\ \text{dBm}$  output of a frequency tripler at  $48.8\ \text{GHz}$ . A more detailed study was performed using the multiplier to injection-lock a  $\sim 20\ \text{dBm}$ ,  $50$  or  $55\ \text{GHz}$  oscillator to a harmonic of the probe laser pulse repetition rate plus  $600\ \text{kHz}$ . The  $50$  or  $55\ \text{GHz}$  signal was down-converted to  $600\ \text{kHz}$  by electrooptic mixing while the second harmonic was found at  $1.2\ \text{MHz}$ . The amplitude response of the electrooptic sampler was calibrated using a lower frequency signal at the same offset. The experimental set-up is shown in Fig. 5.5.

Two doubler designs were evaluated. The first design, having  $5$  sections, was a straight CPW transmission line with  $10$  diodes. The second design, having  $17$  sections, was a  $34$ -diode CPW structure which included four  $90$  degree bends in order to reduce the circuit size. Preliminary measurements on the  $17$ -section doubler with  $0\ \text{dBm}$  of input power at  $48.8\ \text{GHz}$  and  $1\ \text{V}$  reverse bias on the line gave results in reasonable agreement theory up to the first bend. The loss at the fundamental was

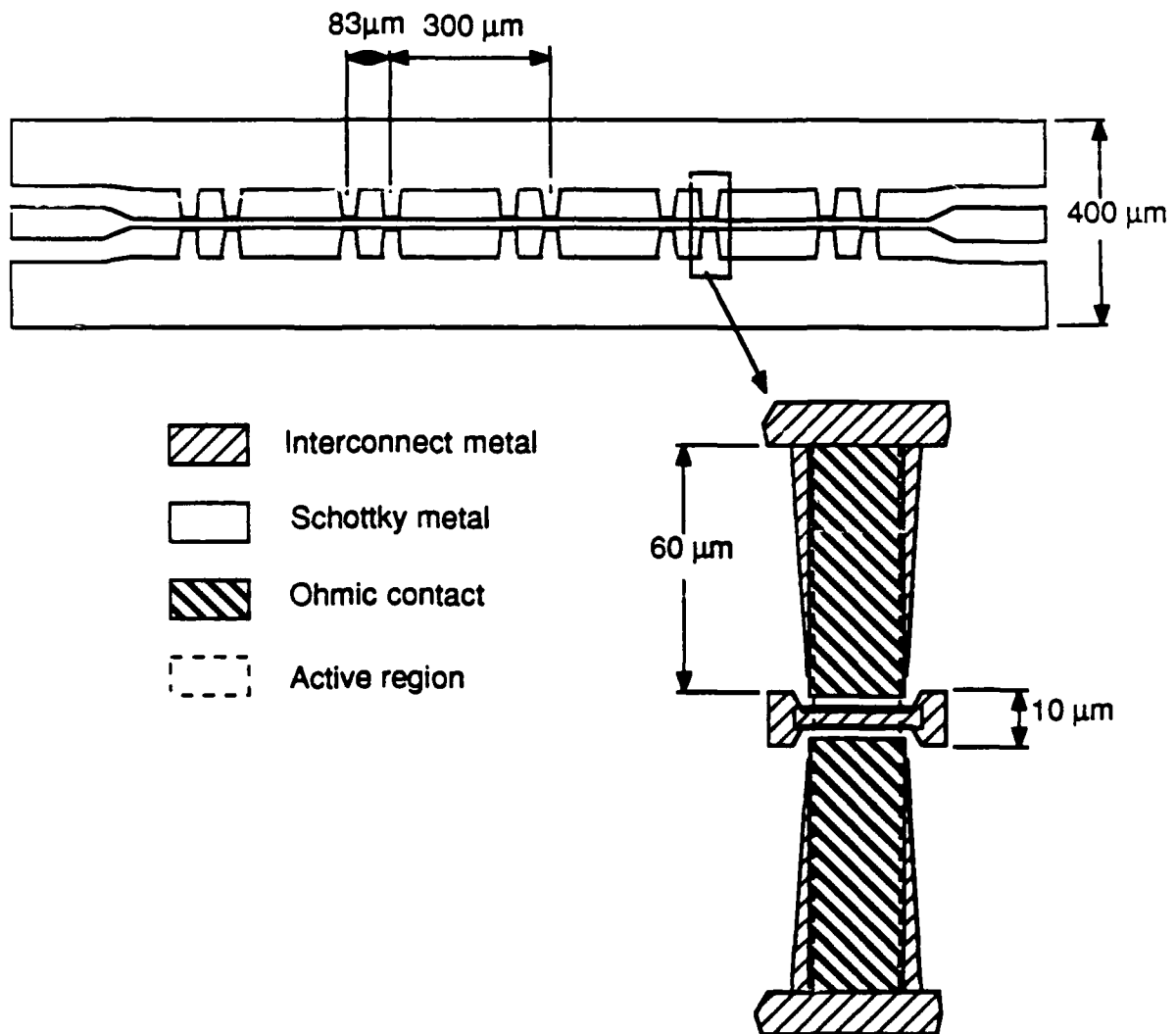


Figure 5.4: Layout of the distributed frequency doubler.

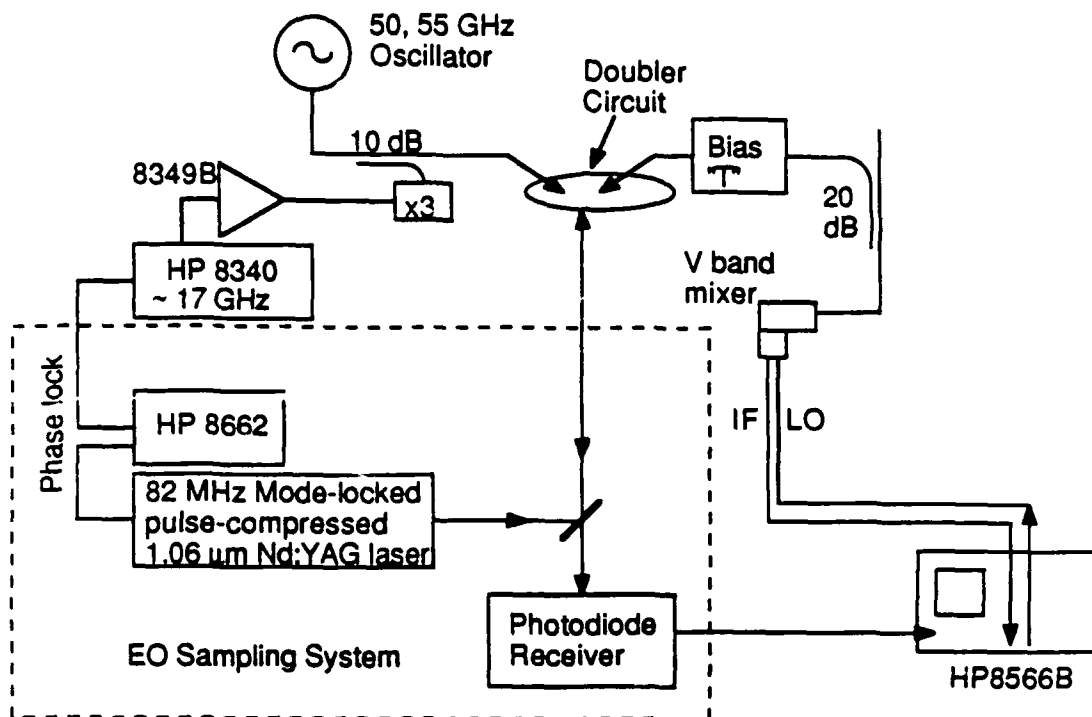


Figure 5.5: Experimental set-up for testing the monolithic doublers.

$\approx 0.08$  Np/section and the minimum conversion loss was 22 dB compared with the theoretical value of 20 dB from Eq. (5.8). The second harmonic amplitude peaked near the end of the first 5 sections, whereas Eq. (5.7) predicts a peak at the sixth section using the theoretical losses.

Although the preliminary measurements showed that the doubler was working in accordance with theory, 1% conversion efficiency does not compare well with other available frequency multipliers. Jim Crowley of Varian III-V device center provided two high-power oscillators for the investigation of higher conversion efficiency. Figures 5.6 and 5.7 show a comparison of the theoretical and experimentally obtained values for both designs. In the 5-section doubler, maximum powers of 2 and 5 dBm were measured with input powers of 14 and 21 dBm at 50 and 55 GHz respectively. The discrepancy between theory and measurement is mainly due to the standing wave generated by the bad match of the 50 GHz wafer probe at the output of the doubler. The 17-section doubler showed better agreement between theory and mea-

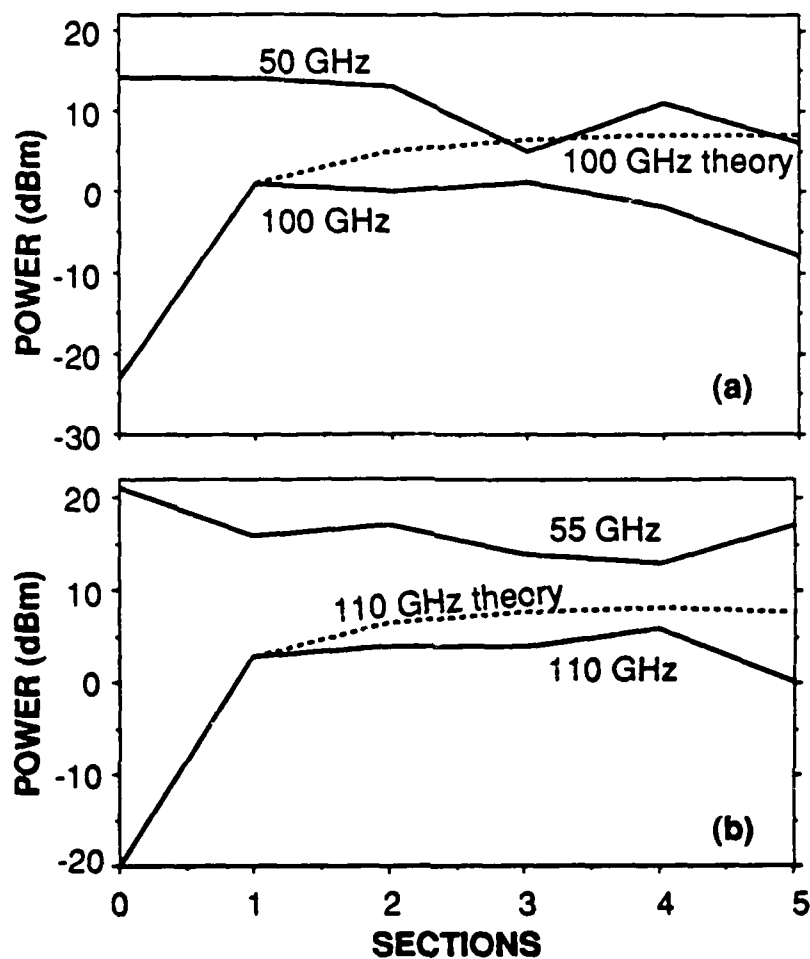


Figure 5.6: Comparison of the theoretical and experimental second harmonic generation for the 5-section doubler. Experimental data for the 50 GHz fundamental and the 100 GHz second harmonic are plotted as a function of position (solid lines) in (a). The theoretical prediction is shown by the dashed curve. The experiment was repeated with a 55 GHz fundamental and 110 GHz second harmonic (b).

measurement because the high losses of the circuit minimized the standing wave effect. A maximum power of 10 dBm was measured at 100 GHz at stage 5, but it was reduced by 8 dB at stage 6, after the 90 degree CPW bends. The 110 GHz data was comparable to the 100 GHz measurement. The theoretical data assumes 50, 55, 100 and 110 GHz line losses of 0.11, 0.13, 0.24 and 0.266 Np/section respectively and  $K_2 a_{10}$  of 0.14 and 0.08 at 50 and 55 GHz respectively. Although the theory predicts the shape of the curve well enough, the values necessary to achieve this fit are not

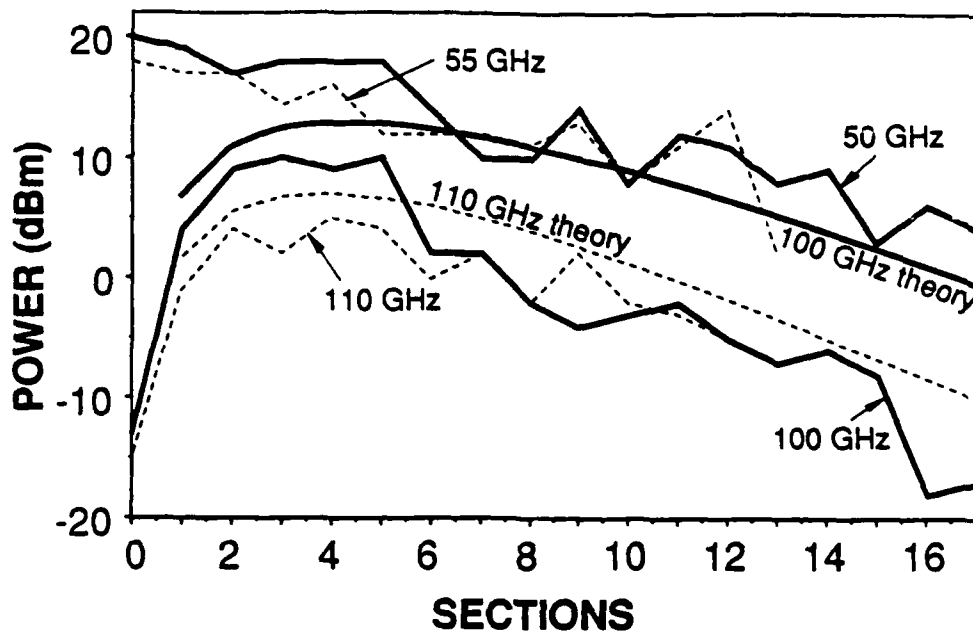


Figure 5.7: Comparison of the theoretical and experimental second harmonic generation at 100 and 110 GHz for the 17-section doubler. Experimental data for the 50 GHz fundamental, the 100 GHz second harmonic, and the predicted 100 GHz values are plotted as a function of position (solid lines). The experiment was repeated with a 55 GHz fundamental and 110 GHz second harmonic (dashed lines).

at all in agreement with those predicted.

## 5.6 Conclusion

The results of the previous section indicate that phase-matched second harmonic generation has been accomplished to some degree. However, the anomalously low value of  $K_2$  indicates that the doubler was not functioning in accordance with theory in the high-power experiment. One contributor to this problem is the fact the line was designed to operate at a reverse bias of 1.5 V but was driven with a 3V sinusoid. Therefore, when the diodes were properly biased for phase-matching, they were driven into forward conduction by the fundamental. Such power was necessary to achieve significant conversion on the short line that was available. Another factor

could be the power-dependant phase velocity briefly mentioned previously. Further analysis is necessary to investigate the magnitude of this effect. If this is a limiting factor, it can be reduced by designing the doping of the epitaxial layer such that a linear capacitance change with voltage is achieved, thus making  $C^{(2)} = 0$ .

The loss at 100 GHz could be partially circumvented if spatial power combining is used instead of phase matching guided waves. This technique has been used for second harmonic generation of optical radiation in lithium niobate [5.9]. The fundamental propagates in the waveguiding structure while the second harmonic radiates into the substrate in a semicone with angle  $\theta$  given in Eq. (5.21). In section 5.4 it was pointed out that, while the structure does radiate, the radiation can be minimized by keeping the transverse dimension small. On the other hand, if the transverse dimension is increased, the structure can radiate with high efficiency. There are several benefits of this approach. First, since the second harmonic is being radiated, the transmission line parameters can be optimized for the fundamental frequency. Second, large, low impedance, low loss CPW sections may be used to connect the Schottky diodes. The characteristic impedance can be raised to  $50\Omega$  using inductive slots in the CPW ground which double as antennas for the second harmonic. Third, the fundamental will not radiate significantly, thereby providing a suppression of the fundamental that is not available from the previous design. Finally, angle tuning of the receiver may be used in addition to voltage tuning to find the optimum conversion efficiency. The proposed structure is shown in Fig. 5.8.

The work of this chapter has shown that the basic principle of phase-matching for second-harmonic-generation on a nonlinear transmission line, as demonstrated by Wedding and Jäger at low frequency is also applicable to generation of mm-wave radiation. The primary contribution of this work was a modification of the structure proposed earlier to allow phase-matched SHG over a broad electrical tuning range. It was also shown that microwave losses on the structure place an upper limit to the conversion efficiency that can be obtained. Spatial power combining should provide a significant improvement in conversion efficiency.

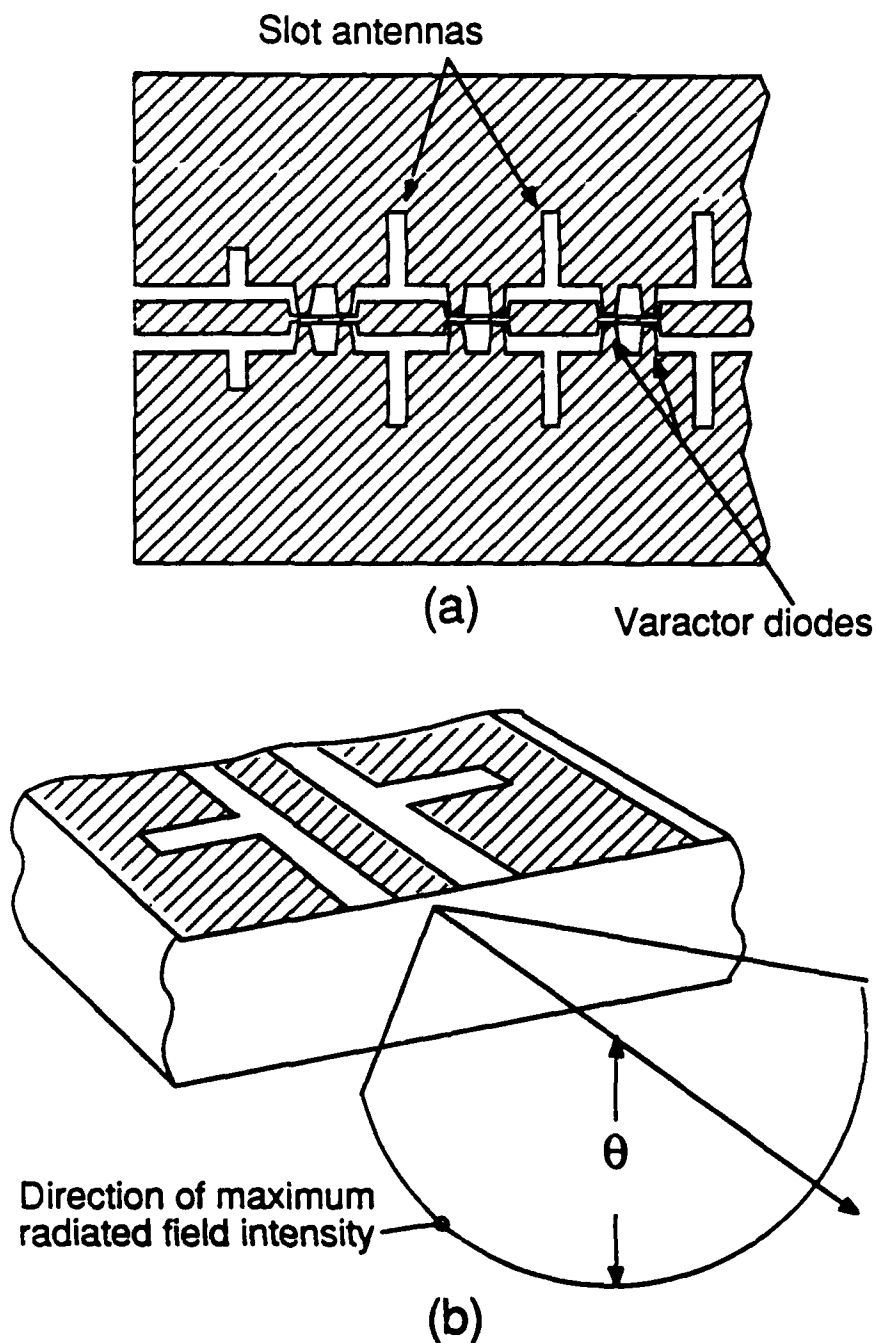


Figure 5.8: Proposed doubler using spatial power combining. The inductive slots in the CPW ground serve as inductors to the fundamental and antennas to the second harmonic (a). Radiation pattern is also shown (b).

## References

- [5.1] R.W. McMillan, "Near-millimeter-wave sources of radiation," *Proceedings of the IEEE*, **73**, 86-108, 1986.
- [5.2] J.W. Archer, "A high performance frequency doubler for 80 to 120 GHz," *IEEE Trans. on Microwave Theory Tech.*, **MTT-30**, 824-825, 1982.
- [5.3] C.J. Madden, R.A. Marsland, M.J.W. Rodwell, D.M. Bloom, and Y.C. Pao, "Hyperabrupt-doped GaAs nonlinear transmission line for picosecond shock-wave generation," *Appl. Phys. Lett.*, **54**, 1019-1021, 1989.
- [5.4] B. Wedding and D. Jäger, "Phase-matched second harmonic generation and parametric mixing on nonlinear transmission lines," *Electr. Lett.*, **17**, 76-77, 1980.
- [5.5] L. Brillouin, *Wave propagation in periodic structures: electric filters and crystal lattices*, Dover, New York, (1953).
- [5.6] W.H. Louisell, *Coupled mode and parametric electronics*, Wiley, New York, (1960).
- [5.7] K.S. Champlin and D.R. Singh, "Small-signal second-harmonic generation by a nonlinear transmission line," *IEEE Trans. on Microwave Theory Tech.*, **MTT-34**, 351-353, 1986.
- [5.8] K.C. Gupta, R. Garg, and I.J. Bahl, *Microstrip Lines and Slotlines*, Artech House Inc, Norwood, (1979).
- [5.9] G.T. Tohmon, K. Yamamoto, and T. Taniuchi, "Blue light source using guided-wave frequency doubler with a laser diode," in *Miniature optics and lasers*, edited by L.E. Cramer, G.T. Forrest, and C. Roychoudhuri, SPIE, Bellingham, 1988.

# Chapter 6

## Future directions

This thesis work has advanced the state of the art in sampler technology from 20 GHz to almost 300 GHz, while reducing the size and enhancing manufacturability. The sampler was then integrated with a resistive directional bridge to form the first S-parameter test-set on a chip. This chip exhibited approximately 10 dB of directivity to 60 GHz. Directivity can be improved with more precise resistor values. Finally, a monolithic distributed frequency multiplier was demonstrated with a 10 % conversion efficiency. With incremental improvements in performance, the directional sampler and distributed doubler technologies could reduce the price and enhance the performance of current mm-wave network analyzers. To exploit this technological advance over the bandwidths now available, it will be necessary to develop new approaches to probe fabrication and circuit interconnects, and to fully exploit the use of optical-IC hybrid systems.

### 6.1 Directional sampler rf probe

One of the advantages of the integrated circuits described here is that they are small enough to be mounted on probe tips. Bringing the measurement instrument into contact with circuit to be tested almost entirely circumvents the difficulty of interconnect losses. A proposed probe design for the directional sampler is shown in Fig. 6.1. With a ceramic probe tip, this approach should perform well to 100 GHz.

Ceramic probes with no active circuitry are commercially available with 65 GHz bandwidth [6.1]. A resistive multiplier assembled on a 5 mil Alumina probe tip has reached 130 GHz [6.2]. Above 100 GHz, the parasitics of the connection between the MMIC and the probe tip become intolerable and the tip must be eliminated. In this case, plated metal pads on the GaAs IC will be brought into direct contact with the circuit under test. Of course, the GaAs can not be allowed to flex, so the contact pressure must be applied by adding a specific weight to a balanced probe.

This work is currently being pursued by Dan Van Der Weide and Mohammad Shakouri. The directional sampler discussed in chapter 4 and the associated IF circuitry are being placed on a microwave probe which will be useful to 65 GHz. Future modifications, coupled with improvements to the directional sampler design should allow operation to 300 GHz. Other circuits that will be probe mounted include the sampler for on-wafer time-domain reflectometry, the NLTL for a fast test signal generator, and the distributed doubler (also as a test signal generator). These on-wafer capabilities are most important for device designers because maximum frequencies of operation are already reaching 300 GHz [6.3]. Getting a detailed look at device operation above 60 GHz should provide new insight into device operation and limitations.

## 6.2 Circuit interconnects for operation to 300 GHz

The sampler and frequency multiplier designs presented here show that extension of broad-band measurement instruments to 300 GHz is feasible. However, one major barrier to the development of such instruments is the limited bandwidth of the interconnections. It is possible to design connectors and coaxial cables that operate single-mode to 100 and possibly 300 GHz by simply scaling down the existing components. However, such a scheme has two major problems. First, the small size required for single-mode operation makes the parts difficult to manufacture. For example, a coaxial connector that is single-mode to 300 GHz would have an

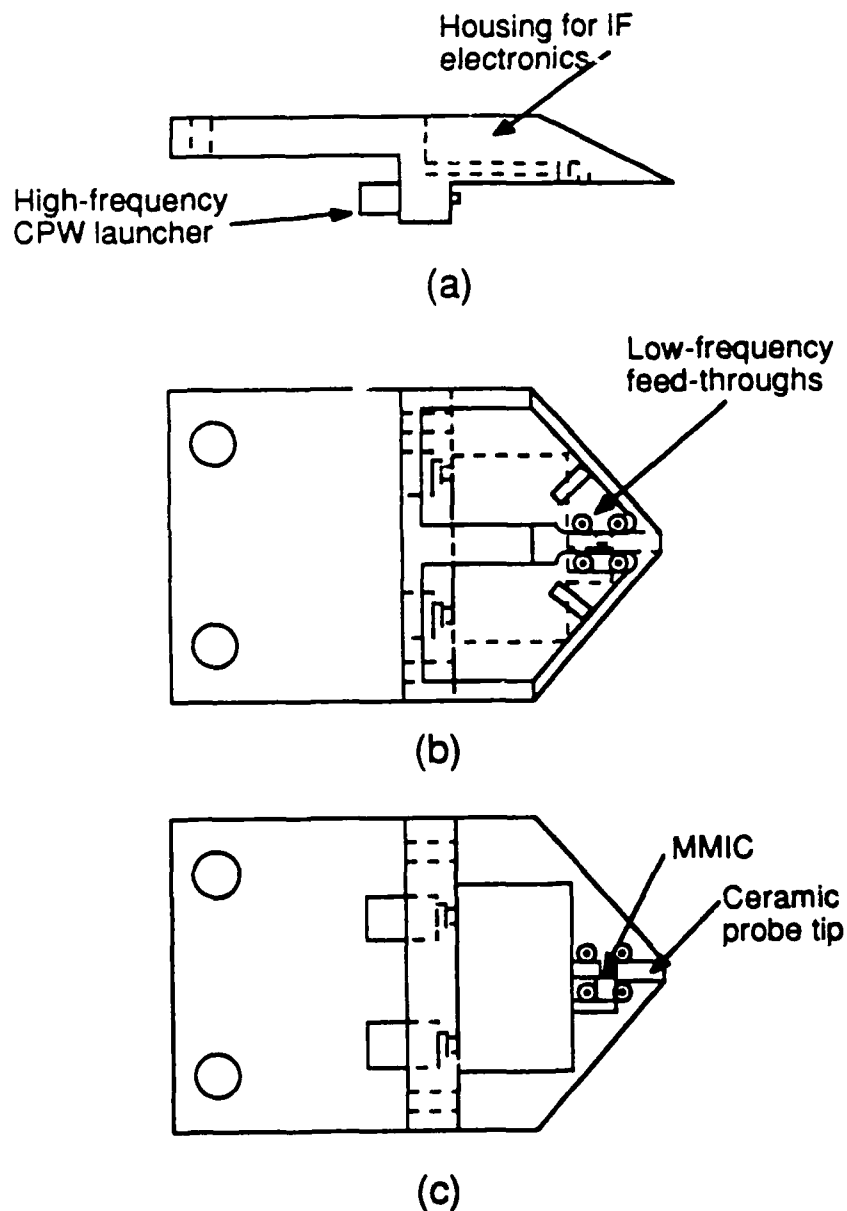


Figure 6.1: On-wafer probing with GaAs MMICs. A prototype active-probe directional sampler is shown in side view (a), top view (b), and bottom view (c). A ceramic probe tip can be used to 100 GHz, but may be abandoned to reach 300 GHz.

outer conductor diameter of  $800 \mu\text{m}$  and an inner conductor diameter of  $348 \mu\text{m}$ . Secondly, conductor losses increase with the square root of frequency and inversely with cable diameter, so a cable which is six times smaller and operating at six times the frequency will have 14.7 times more loss. This means a cable which has a loss of 1.5 dB/foot at 50 GHz and is single-mode to 60 GHz, will have a loss of 22 dB/foot at 300 GHz if scaled down to be single-mode to 360 GHz. In addition to conductor losses, dielectric losses tend to increase linearly with frequency at mm-wave frequencies because of the broad sub-millimeter absorption band in many dielectric materials [6.4]. It is interesting to note, however, that dielectric loss in GaAs is relatively constant to 250 GHz, before it begins to increase due to multi-phonon absorption near 600 GHz.

In the face of dramatically increasing conductor losses with increasing frequency in coaxial cable, engineers have traditionally turned to rectangular waveguide. For example, WR-3 guide has a theoretical attenuation ranging from 5.1 dB/ft to 3.5 dB/ft from 220 to 325 GHz [6.5]. However, it is extremely difficult to make a reproducible interface between a device such as a transistor or solid-state amplifier and the rectangular waveguide mode. The typical 40% waveguide bandwidth is often not large enough and waveguide dispersion makes it unsuitable for propagation of narrow pulses. Clearly there is a need for a low-loss, broad-band waveguiding structure that interfaces conveniently with solid-state devices.

One approach which is now widely used is to place a printed circuit transmission line inside of a hollow waveguide [6.6]. The printed circuit increases the bandwidth of the hollow guide and the hollow guide, by preventing radiation, allows larger conductors to be used on the printed circuit, thereby reducing the printed circuit conductor loss. An example of this type of line is the fin-line invented by Meier [6.7]. Fin-line is often used to provide a transition between the waveguide mode and a quasi-TEM planar transmission line such as microstrip which is used for microwave circuits. Fin-line, however, is not useful for connecting to circuits with many inputs and outputs.

Another approach is to accept high losses and simply reduce the length of the interconnect. This can be accomplished by combining the various components which

require broad-band connection on the same monolithic integrated circuit. This was the key to the success of the sampler presented in Chapter 3. Various integrated circuits can be connected together without lengthy interconnections by designing the ICs so that they may be brought into direct contact. This technique was employed for the Generation III sampler, with bond wires bridging the gap between the circuits. Alternatively, metal bumps could be plated on circuit input and output connections so the chips can simply be pressed together. However, higher levels of integration only postpone the eventual necessity of connection to the outside world. An interesting alternative to this final connection is the monolithic antenna. Patterning an antenna or array of antennas on the integrated circuit allows communication via free space propagation. Obviously, it may be difficult to use antennas for circuits with multiple inputs and outputs, but this approach has proven useful in several applications including high-power microwave generation [6.8] and radar transmit-receive modules [6.9].

Losses in existing waveguiding structures constructed of high-purity metals can be reduced by operating at a lower temperature. Resistivity due to phonon scattering decreases linearly with absolute temperature down to the Debye temperature  $\Theta_D$ , where it begins to fall off even more rapidly, approaching  $(T/\Theta_D)^5$  for  $T \ll \Theta_D$  [6.10]. Thus, a metal film such as copper ( $\Theta_D = 333K$ ) of sufficient purity at 85K would have a resistivity ten times lower than at room temperature. This means that if one is willing to suffer the expense of a liquid nitrogen cooling system and higher purity metals, drastically reduced losses can be achieved without significantly altering the circuit design or using a different metalization.

Finally, high- $T_c$  superconductors offer the hope of even lower losses at mm-wave frequencies. According to the BCS theory [6.11], superconducting materials can have significant loss at mm-wave frequencies due to Cooper-pair breaking by the high-frequency fields. At frequencies above the frequency corresponding to the energy required for pair breaking

$$f_{gap} = \frac{3.54k_B T_c}{2\pi\hbar} \quad (6.1)$$

where  $k_B$  is the Boltzmann constant and  $T_c$  is the temperature of the superconducting transition, the material reverts to normal conduction. Eq. (6.1) shows why

high- $T_c$  superconductors are anticipated to be useful in mm-wave circuits. For example, a  $90^\circ T_c$  superconductor would have an  $f_{gap} = 6.65$  THz. There is still considerable controversy over the applicability of BCS theory to the new high- $T_c$  superconductors, nevertheless, theoreticians have already used the BCS theory to compare the possible performance of the new superconductors with conventional conductors such as copper [6.12]. If these predictions prove valid, a  $90^\circ T_c$  superconductor such as YBCO could offer lower loss than copper at 85K up to 500 GHz. The advantage of YBCO at 100 GHz would be perhaps a factor of ten. However, recent experimental measurements of surface resistance on 2000Å thick YBCO have shown no advantage of this material over gold for frequencies above 100 GHz [6.13]. It remains to be seen whether thicker, higher quality YBCO films will achieve the advantage predicted by the BCS theory.

### 6.3 Optical synthesis

Another method of circumventing lossy interconnections is to place the mm-wave signal on an optical carrier. A photodiode receiver could then be integrated with the circuitry on-chip. The bandwidth available on an optical carrier is tremendous. This perspective brings a new challenge to measurement technology: how to achieve bandwidths that are significant in comparison to the optical frequency of today's communication systems, 194 THz. The possibility of such broadband detection is illustrated by the metal-insulator-metal (MIM) diode. This device has been used for signal rectification up to 197 THz for optical frequency synthesis and measurement [6.14]. If this detector was combined with a sampling receiver, a frequency synthesizer could be constructed that is tunable over a sizable optical bandwidth.

The nonlinearity of the MIM diode is due to the quantum-mechanical tunneling of electrons through the barrier created by the thin insulator. In the common W-Ni diode, the insulator is nickel's native oxide. The device is usually assembled much like a crystal radio detector where the tungsten is a  $2 \mu\text{m}$  whisker that is electrochemically etched to form a  $1000\text{Å}$  tip which is then brought into contact with the nickel sample using a micro-positioner. Attempts have been made to pattern

them monolithically [6.15]. However, the technology now exists for micro-machining tungsten tips on silicon wafers. These tips can have 500 to  $100\text{\AA}$  radii of curvature [6.16]. The smaller tip area may permit the MIM diode to be used well above 197 THz, while the micro-machined structure may permit the integration of an array of MIM diodes with a sampling receiver. Thus the frequency difference between two optical sources could be detected without the use of a small band-gap material for electron-hole pair production. An example of such a system is shown in Fig. 6.2. The synthesized output can be used as a local oscillator for a high resolution spectrum analyzer, or the combined synthesized and reference outputs can be used as a source of mm-wave radiation.

The MIM diode provides the possibility of huge bandwidths. However, the conventional photodiode has also made significant progress in recent years. In the popular 1.3 and 1.55  $\mu\text{m}$  communications bands, the preferred detector material is InGaAs on InP. Detectors in this material system have reached 67 GHz [6.17]. For visible radiation, the more mature GaAs technology detectors have reached 100 GHz [6.18] with a quantum efficiency of 25%. Since quantum efficiency can be traded directly for bandwidth in a conventional vertical photodiode [6.19], the bandwidth can be increased significantly in applications where sensitivity is not of primary importance.

When the signal is delivered to the chip on an optical carrier, the bandwidth is only limited by the on-chip circuitry. For example, suppose a sampler is integrated with one or more diode detectors (MIM or photodiode). Utilizing the techniques developed here, a sampler having a 1 THz GHz 3-dB bandwidth should be feasible. If the transmission lines connecting the detectors and the sampler are less than 100  $\mu\text{m}$  long, the detector - sampling receiver combination could also approach a 3-dB bandwidth of 1 THz. Using this sampling receiver in an optical synthesizer would provide an  $80\text{\AA}$  tuning range at 1.55  $\mu\text{m}$  wavelength.

Another application for this sampling photoreceiver is electrooptic sampling. This technique, discussed in Chapter 1, uses an ultra-fast pulsed laser to achieve picosecond time resolution. However, the techniques used to produce the ultrafast pulses, such as mode-locking and pulse compression, also contribute to intensity

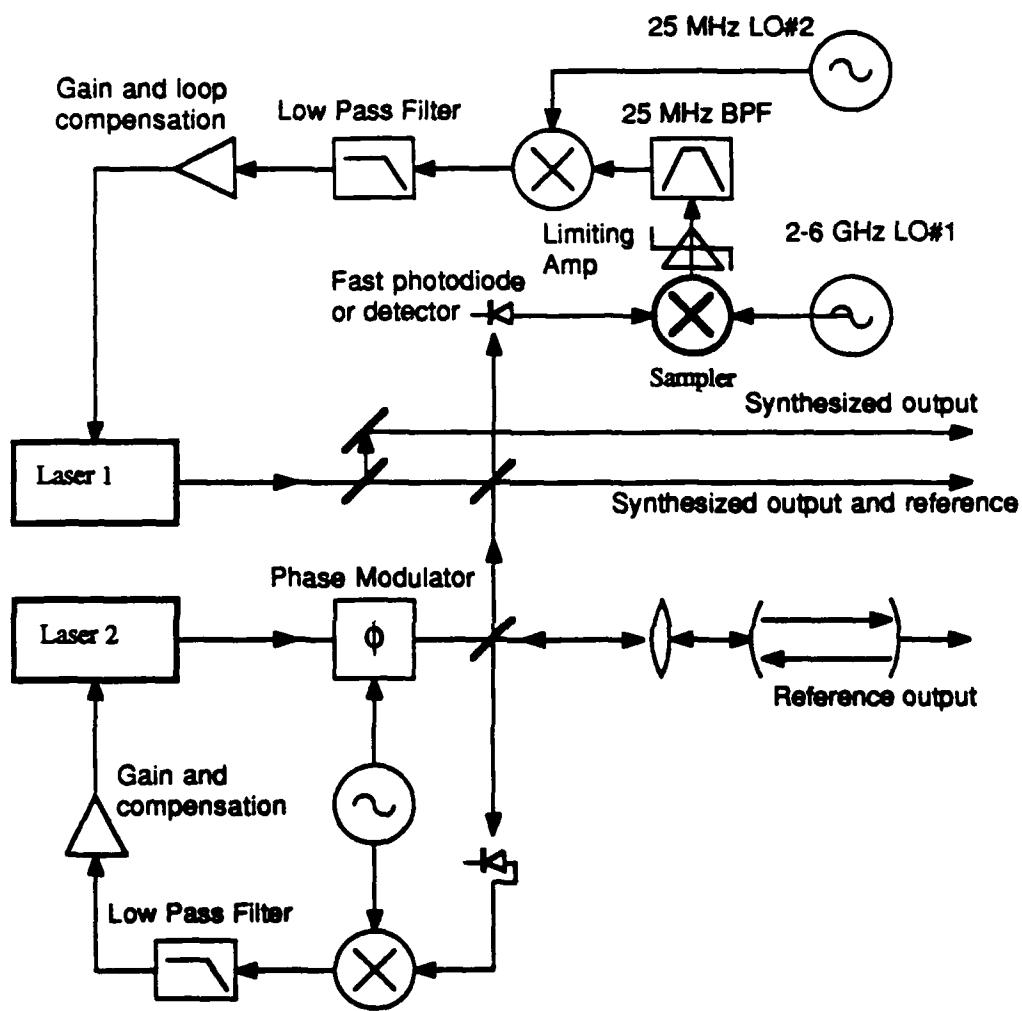


Figure 6.2: Optical frequency synthesizer block diagram.

noise on the laser beam. In addition, it is very difficult to stabilize the pulse repetition rate to the degree necessary for low phase-noise measurements at mm-wave frequencies. If the pulsed laser were replaced by a continuous-wave laser that was amplitude and frequency stabilized, the received electrooptic signal would be nearly shot-noise limited. The 1 THz photoreceiver and its microwave local oscillator would then set the time resolution of the system. It is interesting that the high-speed sampler technology that was motivated in part by the picosecond time resolution made possible by the ultra-fast laser could render it obsolete.

## References

- [6.1] Cascade Microtech Inc., P.O. Box 2015, Beaverton, OR 97075.
- [6.2] R. Majidi-Ahy, B.A. Auld, and D.M. Bloom, "100 GHz on-wafer S-parameter measurements by electrooptic sampling," *IEEE MTT-S International Microwave Symposium*, 299-302, 1989.
- [6.3] U.K. Mishra, A.S. Brown, M.J. Delaney, P.T. Greiling, and C.F. Krumm, "The AlInAs-GaInAs HEMT for microwave and millimeter-wave applications," *IEEE Trans. on Microwave Theory Tech.*, MTT-37, 1279-1285, 1989.
- [6.4] M.N. Afsar, K.J. Button, "Millimeter-wave dielectric measurement of materials," *Proceedings of the IEEE*, 73, 131-147, 1985.
- [6.5] E.C. Jordan, ed., *Reference data for radio engineers, electronics, computer, and communications, 7th ed.*, Howard W. Sams & Co., Indianapolis, (1988).
- [6.6] T. Itoh, "Overview of quasi-planar transmission lines," *IEEE Trans. on Microwave Theory Tech.*, MTT-37, 275-280, 1989.
- [6.7] P.J. Meier, "Integrated fin-line millimeter components," *IEEE Trans. on Microwave Theory Tech.*, MTT-22, 1209-1216, 1974.
- [6.8] Z.B. Popović, R.M. Weikle II, M. Kim, K.A. Potter, and D.B. Rutledge, "Bar-grid oscillators," *IEEE Trans. on Microwave Theory Tech.*, MTT-38, 225-231, 1990.
- [6.9] J. Birkeland and T. Itoh, "Quasi-optical planar FET transceiver modules," *IEEE MTT-S International Microwave Symposium*, pp. 119-122, 1989.
- [6.10] R.H. Bube, *Electronic properties of crystalline solids*, Academic Press, Orlando, (1974).
- [6.11] N.W. Ashcroft and N.D. Mermin, *Solid state physics*, Saunders college, Philadelphia, (1976).

- [6.12] E.B. Ekholm and S.W. McKnight, "Attenuation and dispersion for high- $T_c$  superconducting microstrip lines," *IEEE Trans. on Microwave Theory Tech.*, **MTT-38**, 387-395, 1990.
- [6.13] M.C. Nuss, K.W. Goossen, P.M. Mankiewich, R.E. Howard, B.L. Straughn, G.W. Berkstresser, and C.D. Brandle, "YBa<sub>2</sub>Cu<sub>3</sub>O<sub>7</sub> Superconductors for high-speed interconnects," *IEEE Electron Device Lett.*, **11**, 200-202, 1990.
- [6.14] D.A. Jennings, K.M. Evenson, and D.J.E. Knight, "Optical frequency measurements," *Proceedings of the IEEE*, **74**, 168-179, 1986.
- [6.15] J.G. Small, G.M. Elchinger, and A. Javan, "ac electron tunneling at infrared frequencies: Thin-film MOM diode structure with broad-band characteristics," *Appl. Phys. Lett.*, **24**, 275-279, 1974.
- [6.16] H.H. Busta, R.R. Shaddock, and W.J. Orvis, "Field emission from tungsten-clad silicon pyramids," *IEEE Trans. Electr. Dev.*, **36**, 2679-2685, 1989.
- [6.17] R.S. Tucker, A.J. Taylor, C.A. Burrus, G. Eisenstein, J.M. Wiesenfeld, "Coaxially mounted 67 GHz bandwidth InGaAs PIN photodiode," *Electr. Lett.*, **22**, 917-918, 1986.
- [6.18] S.Y. Wang and D.M. Bloom, "100 GHz bandwidth planar GaAs Schottky photodiode," *Electr. Lett.*, **19**, 554-555, 1983.
- [6.19] S.M. Sze, *Physics of semiconductor devices*, Wiley & Sons, New York, (1981).